# Nearly-Hyperuniform Network Models of Amorphous Silicon

Miroslav Hejna

A Dissertation

Presented to the Faculty

of Princeton University

in Candidacy for the Degree

of Doctor of Philosophy

Recommended for Acceptance

by the Department of

Physics

Advisers: Paul J. Steinhardt and Salvatore Torquato

September 2013

# Abstract

In this thesis, we introduce the concept of *nearly hyperuniform network* (NHN) structures as alternatives to the conventional continuous random network (CRN) models for amorphous tetrahedrally-coordinated solids, such as amorphous silicon (a-Si). A hyperuniform solid has a structure factor $S(k)$ that approaches zero as the wavenumber $k \to 0$. We define a NHN as an amorphous network whose structure factor $S(k \to 0)$ is smaller than its liquid value at the melting temperature. Using a novel implementation of the Stillinger-Weber potential for the interatomic interactions, we show that the energy landscape for a spectrum of NHNs includes a sequence of local minima with an increasing degree of hyperuniformity, i.e. smaller $S(k \to 0)$ that is significantly below the frozen liquid value and that correlates with the width of the electronic band gap and with other measurable features in $S(k)$ at intermediate and large $k$.

We compare the structural properties predicted by these NHN models to the results of highly sensitive transmission X-ray scattering measurements performed at the Advanced Photon Source at Argonne National Laboratory, on high-purity a-Si samples with density close to that of crystalline silicon (c-Si). The best theoretical NHN model produced so far possesses $S(k \to 0) = 0.010 \pm 0.002$, which is consistent with the experimentally observed value $S(k \to 0) = 0.0075 \pm 0.0005$. Our theoretical studies predict an increase in the degree of hyperuniformity with annealing, which is also observed in these experiments. Both theoretical models and experimental measurements show that increasing the degree of hyperuniformity is correlated with increasing the height and narrowing the width of the first diffraction peak, and with extending the range of oscillations in the pair correlation function. This work suggests that there is a greater diversity of theoretical network structures and experimental realizations of amorphous silicon than was previously recognized.

# Acknowledgements

To my mother

# Contents

# List of Tables

# List of Figures

# List of Abbreviations

a-Si        amorphous silicon

c-Si        crystalline silicon

CRN        continuous random network

$G(r)$        reduced radial distribution function

$g(r)$        pair correlation function

$k$        wavenumber

K1-5        models relaxed with the Keating potential

NHN        nearly hyperuniform network

p-Si        polycrystalline silicon

RDF        reduced radial distribution function

$S(k)$        structure factor

SW1-5        models relaxed with the Stillinger-Weber potential

TA        transverse acoustic phonon peak

TO        transverse optic phonon peak

WWW        Wooten, Winer, and Weaire

# Thesis Outline

In Chapter 1, we explain the importance of amorphous silicon (a-Si) in the micro-electronics applications and as a prototype for a wider range of disordered tetrahedral materials. We also give a definition of hyperuniformity and discuss its significance in understanding the long-range structure of the disordered materials. In Chapter 2, we present some background information on various techniques that have been employed to study the structure of a-Si. Chapters 3, 4, and 5 are based on an article [1]. Chapter 3 introduces the concept of nearly hyperuniform network models (NHN) and discusses their implications for the structure of a-Si and the electronic band-gap in a-Si. In Chapter 4, we give details of the techniques used to produce NHN models. Chapter 5 presents the geometric and topological characteristics of the structure of NHN models, and their electronic and vibrational density of states. In Chapter 6, we compare the predictions of NHN models to recent measurements performed by Xie et al. [2] and Laaziri et al. [3, 4]. Finally, we summarize our findings and discuss future research in Chapter 7.

# Chapter 1

# Introduction and Motivation

## 1.1 Practical Significance of Amorphous Silicon

A MORPHOUS silicon (a-Si) has found diverse applications in microelectronics since the 1980's. These include thin-film transistors, active-matrix liquid-crystal displays, photodiodes, image sensor arrays, scanners, medical imagers, light sensors, multilayer color detectors, position sensitive detectors, large scale power generation, and solar cells [5, 6]. The use of a-Si in microelectronics is not surprising, given that a-Si exhibits semiconducting properties such as an electronic and optic band-gap, the ability to be doped, and photoconductivity; these properties are similar to those found in the crystalline (c-Si) and polycrystalline (pc-Si) silicon. While a-Si has a significantly lower free carrier mobility (by a factor of about 30) than that of c-Si, its characteristics are more favorable for many applications. Owing to its disordered structure and lack of domain walls, a-Si is isotropic and more homogeneous compared to c-Si and pc-Si. a-Si has a direct electronic band-gap in contrast to the indirect band-gap of c-Si and pc-Si. Though a-Si has a disadvantage over c-Si

due to the presence of dangling bond defects in its structure, this disadvantage can be mitigated by passivating of the dangling bonds via hydrogenation.

Arguably, the most important application of a-Si is in thin-film transistors (TFT) [7]. TFTs are now widely used in active-matrix liquid-crystal displays and digital radiography. In these applications , the primary advantage a-Si has over c-Si is its amorphous structure, which allows hetero-interfaces to be easily formed, and its higher resistivity which matches the resistivity of the liquid crystals.

Another major application of a-Si is in solar photovoltaic cells [8]. An appeal of a-Si for solar cells is that for a given layer thickness, a-Si absorbs about 2.5 times more energy than c-Si due to a larger, direct band-gap resulting from the isotropy of a-Si and the fact that the momentum selection rule for optical absorptions does not apply for a-Si resulting from the lack of a translational symmetry in the disordered structure of a-Si. A thickness of less than $1\,\mu$m of a-Si is sufficient to absorb a large fraction of sunlight, compared to about $5\,\mu$m needed for c-Si, requiring less material for a-Si films of solar cells, making them lighter and less expensive. Although the applications of a-Si in solar cells has not yet proved economically competitive with power generation based on fossil fuels, it seems only a matter of time before solar cell-based power generation will become profitable without the need for governments subsidies.

The ability to control the properties of a-Si, and to expand the range options and devices makes the future of a-Si in microelectronics very promising. With possible future applications such as phase-change and analogue memory [9], and multi-junction thin-film full spectrum solar cells [10], there is no doubt that a-Si will play an increasing role in electronics applications in the foreseeable future. Understanding the relationship between the structure of a-Si and the corresponding physical properties is crucial to the design of many technological devices, and practical applications of a-Si continue to motivate the need for a better description of the structure of a-Si.

## 1.2 Manufacturing of Amorphous Silicon

Contrary to glasses and most amorphous materials, a-Si cannot be prepared by a rapid quenching of liquid silicon. The expected cooling rate needed to achieve an amorphous state by rapid cooling of a liquid state is $10^{11}\,\mathrm{Ks^{-1}}$ [11, 12]. Such a cooling rate is many orders of magnitude higher than what can be currently achieved in laboratories (about $10^6\,\mathrm{Ks^{-1}}$) [12, 13]. Methods of preparation of a-Si include pressure induced amorphization, laser quenching, vapor deposition, and sputtering. The purest form of a-Si is produced by self-ion implantation (silicon ion bombardment) [3, 4].

The ion implantation method produces a-Si by bombarding a liquid nitrogen cooled c-Si (001) wafer with silicon atoms at different energies and fluencies [14]. The silicon ion energies vary from $1.5\,\mathrm{MeV}$ to $27\,\mathrm{MeV}$ and the fluencies vary from $5\times10^{15}\,\mathrm{ions\,cm^{-2}}$ to $9\times10^{15}\,\mathrm{ions\,cm^{-2}}$, giving a c-Si sample a cumulative dose of $8.3\times10^{16}\,\mathrm{ions\,cm^{-2}}$, while producing a $12\,\mu\mathrm{m}$ thick a-Si membrane. Any traces of c-Si in the sample can be removed by a wet chemical etch with 20% solution of KOH, as c-Si is more susceptible to KOH etching. The impurity level in a sample produced by ion implantation method is below 0.1% [14]. Thermal annealing of an as-implanted sample in vacuum at $600\,^{\circ}\mathrm{C}$ produces an annealed sample of a-Si.

Pressure induced amorphization uses a diamond anvil cell to compress porous c-Si. The sample is transformed to a-Si at pressures in excess of $10\,\mathrm{GPa}$ [15] and remains amorphous upon decompression. Pressure induced amorphization can also be achieved using nano-indentation [16]. Other methods of fabricating a-Si include laser quenching [17], where silicon is amorphized by melting c-Si with picosecond laser pulses, chemical vapor deposition [18], where a-Si is formed by condensation of vaporized silicon onto a substrate, and magnetron sputtering [19], where silicon atoms ejected from a target by energetic ion bombardment are deposited onto a substrate.

Amorphous silicon networks structures and their properties in general depend on the preparation method [20]. It has been conjectured [21] that the relaxed form of

a-Si approaches a universal structure. We will show in Chapter 3 that the possible structures of a-Si span a much larger class of structures than previously recognized.

## 1.3   Experimental Probes of Amorphous Silicon

Experimentally, the most direct probe of the structure of a-Si is provided by diffraction scattering experiments (X-ray or neutron). Since the positions of silicon atoms in a-Si lack periodicity and a preferred direction, the entire X-ray signal is due to the diffuse scattering and depends only on the magnitude of the scattering vector $k = |\mathbf{k}|$. Scattering experiments provide the values of the structure factor $S(k)$ as a function of the magnitude of the scattering vector $k = \frac{4\pi}{\lambda} \sin(\theta/2)$, where $\theta$ is the scattering angle and $\lambda$ is the wavelength of the electromagnetic wave, or the de Broglie wavelength of the neutrons. The structure factor is defined as

$$S(k) = \frac{1}{N} |n_{\mathbf{k}}|^2, \tag{1.1}$$

where $n_{\mathbf{k}} = \sum_j e^{-i\mathbf{k}\cdot\mathbf{r}_j}$ is the scattering amplitude of a point pattern, $N$ is the number of atoms, $\mathbf{r}_j$ are the positions of atoms, and $\mathbf{k}$ is the scattering vector. Note that for isotropic point patterns $n_{\mathbf{k}}$ depends only on the magnitude of the wavevector $k = |\mathbf{k}|$ allowing us to write to $S(k)$ as a function of $k$. In the following, we omit the delta-function forward scattering at $k = 0$ and define $S(0)$ by $S(0) = S(k \to 0)$. Using the Fourier transform, the structure factor $S(k)$ can be inverted to obtain the pair correlation function $g(r)$ using the formula (valid for three dimensional isotropic point patterns)

$$g(r) = 1 + \frac{1}{2\pi^2\rho} \int_0^\infty k\left(S(k) - 1\right) \frac{\sin(kr)}{r} dk, \tag{1.2}$$

where $\rho$ is the sample density.

To date, the most precise scattering measurement on a-Si was obtained by Xie et al. [2] at the Advance Photon Source in the Aragon National Laboratory. Xie et al. used a highly sensitive small angle transmission spectroscopy with a $250\,\mu\text{m} \times 250\,\mu\text{m}$ beam of $17\,\text{keV}$ X-rays in vacuum with a sample to detector distance $293\,\text{mm}$ to measure the scattering intensity in the transmission geometry from an edge-supported membrane of a-Si [14]. The measurements were immediately repeated with $9\,\text{keV}$ X-rays. Xie et al. verified that the amorphous scattering volume is free from nucleation of nanocrystalline silicon, by demonstrating the absence of a very tiny but sharp c-Si(111) scattering feature on the principal peak. The structure factor at large $k$ (up to $55\,\text{Å}^{-1}$), needed to obtain the pair correlations function, was measured by Laaziri et al. [3, 4].

A major limitation of the scattering experiments is that they only provide information about the angular average of pair statistics. The structure factor $S(k)$ depends only on the magnitude of the scattering vector and consequently only the angularly averaged pair correlation function is obtained. There is a large degeneracy of amorphous structures with the same radial pair statistics ($g(r)$ or $S(k)$). That is, there is a large number of amorphous structures with identical $g(k)$ and $S(k)$, but different higher-order correlations $g_3, g_4 \cdots$ [22]. Microscopic structural models have been devised to understand the full three-dimensional structure of a-Si. Predictive models must be constructed as local minima of physically realistic inter-atomic interactions in order to reduce the aforementioned structural degeneracy. The development of accurate models for a-Si that can explain the measured structure factor and pair correlation function as well as all other properties of a-Si is a subject of this thesis.

Another probe of a-Si, independent of the scattering experiments is provided by the measurement of the phonon spectra (vibrational density of states). The phonon spectra are measured either by the neutron scattering [23, 24] or by the Raman

scattering [20, 25]. The size of the electronic band gap is also an important probe imposing constraints on the number of coordination defects in a-Si. The size of the electronic band gap, $\Delta E_g$, is observed to increase with annealing. The self-ion implanted a-Si sample has a band gap of $\Delta E_g = 0.85\,\mathrm{eV}$ and annealed samples (3 h at 500 °C) has a band gap of $\Delta E_g = 1.30\,\mathrm{eV}$ [26, 27]. These values should be compared to the size of the band gap of c-Si, which is $\Delta E_g = 1.1\,\mathrm{eV}$.

## 1.4 Theoretical Significance of Amorphous Silicon

Theoretically, a-Si is one of the simplest disordered network materials, serving as a model for study of a wide range of glassy and amorphous systems [13]. a-Si is a prototypical example of a covalently bonded, tetrahedrally coordinated amorphous solids, examples of which include Silicon, Germanium, Silicon dioxide, Germanium dioxide, Silicon-germanium, Zinc chloride and water. Since a-Si contains only one type of atom, its structure is easier to understand than the compounds and alloys.

On a short range, atomic positions are completely described in terms of bond-length $d$, bond-angle $\theta$ and dihedral angle $\alpha$, see Fig. 1.1 for illustration. On a medium range, partial information about the structure is provided by ring statistics. On a long range, no simple metric can fully describe the structure as the number of degrees of freedom grows without bound with increasing scale. Choosing the correct metric to characterize the large scale properties of a disordered material is the hardest and arguably the most important part of a structural description. Hyperuniformity was proposed as a suitable order metric to characterize a disordered material according to its local density fluctuations [28]. Hyperuniformity is discussed in detail in the following section.

Despite being disordered and isotropic, at a short range (0-6 Å) a-Si retains the same local chemical bonding as that of c-Si. Silicon atoms are almost perfectly tetra-

(a)     Bond-length          (b)     Bond-angle          (c)     Dihedral-angle
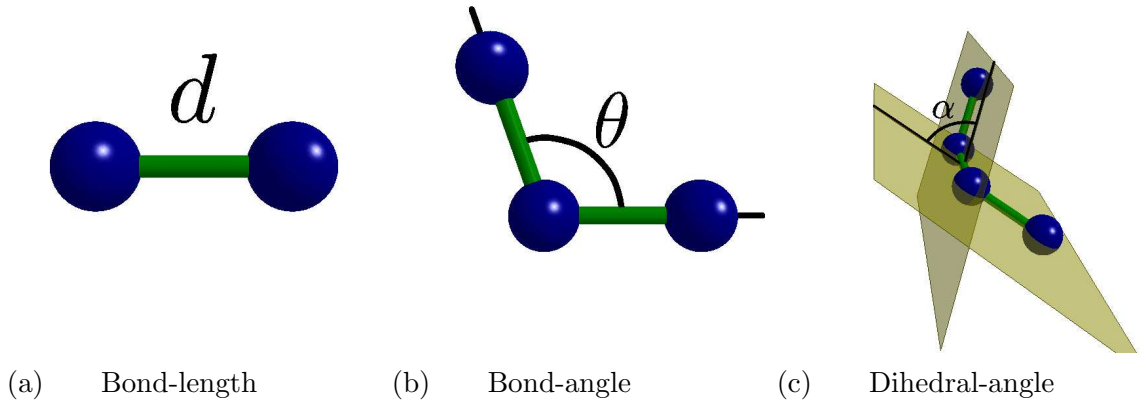
Figure 1.1: Characteristics of the short-range atomic ordering

hedrally coordinated with less than 0.1% coordination defects [29]. The bond-length and bond-angle are close to the crystalline values, with only a few percent deviation [3, 4, 30]. The dihedral angle on the other hand has a very broad distribution, close to the uniform distribution proposed by Zachariasen for an ideal glass in 1932 [31]. On a medium scale, (6-20 Å) a-Si can be partially described by the relative representation of the shortest-path irreducible rings formed by silicon atoms [32]. Since c-Si has a diamond cubic lattice, it contains only six-atom rings. The a-Si ring structure on the other hand, while having a large proportion of six-atom rings, also contains a significant number of five- and seven-atom rings, and a small number of rings with less than five or more then seven atoms. On a large scale (20 Å and larger) a-Si looks homogeneous and isotropic. The amount of the density fluctuation on a large scale is partially described by the hyperuniformity order metric.

a-Si is an example of a highly over-constrained material. The number of constraints is seven, far exceeding the three translational degrees of freedom per atom. See Appendix A for details of the constraint counting. The highly over-constrained configuration of a-Si is in contrast to $SiO_2$, which is isostatic. The high strain results in a-Si is far from equilibrium [21], making it ideal for the study of non-equilibrium statistical systems.

9

The existence of a large band-gap in the electronic density of states of a-Si is not only technologically important, but is also of great theoretical interest. The band-gap of a-Si $\Delta E_g = 1.5\,\text{eV}$ lies between the indirect band-gap $\Delta E_{g,\text{ind}} = 1.1\,\text{eV}$ (difference between the minimum energy in the conduction band and the maximum energy in the valence band) and the direct $\Gamma$ band-gap $\Delta E_{g,\Gamma} = 3.4\,\text{eV}$ (difference between the energy of the conduction band and the valence band at the $\Gamma$ point, which lies at the center of the Brillouin zone) of c-Si [33]. Historically, the existence of a large band-gap in a-Si was surprising, given the disordered structure of a-Si. Weaire and Thorpe were the first to use a theoretical argument to show a possibility of a band-gap in disordered, covalently bonded tetrahedral materials such as a-Si [34, 35]. Their argument explains the existence of a band-gap as a consequence of a high local bonding order (perfect four-coordination and small deviations of bond-length and bond-angles) [13].

## 1.5   Hyperuniformity

A point pattern is *hyperuniform* if the number variance $\sigma_R^2 \equiv \langle N_R^2 \rangle - \langle N_R \rangle^2$ within a (hyper-)spherical sampling window of radius $R$ grows more slowly than the window volume for large $R$, i.e. more slowly than $\mathbb{R}^d$ in $d$ dimensions, see Fig. 1.2 for illustration [28]. In reciprocal space, hyperuniformity corresponds to a pattern having a structure factor $S(k)$ that tends to zero as the scattering vector $k = |\mathbf{k}|$ tends to zero, i.e. the infinite wavelength density fluctuations vanish [28]. For any system, the structure factor $S(k \to 0)$ can be expressed in terms of the fluctuation of $N(R)$, the number of atoms in a sphere with radius $R$, as $S(k \to 0) = \lim_{R \to \infty} [\langle N(R)^2 \rangle - \langle N(R) \rangle^2] / \langle N(R) \rangle$. For a system in thermal equilibrium, one can show that $S(k \to 0) = \rho k_B T \chi_T$, where $\rho$ is the number density, $T$ is the temperature, $\chi_T$ is the isothermal compressibility and $k_B$ is the Boltzmann constant.
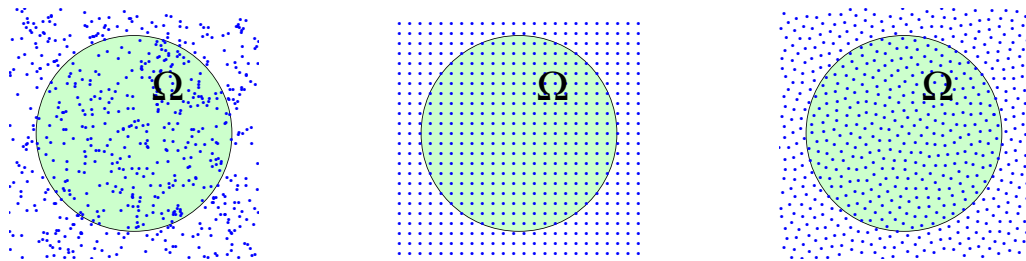
(a) Poisson pattern      (b) Crystalline pattern      (c) Hyperuniform pattern

Figure 1.2: Hyperuniform and non-hyperuniform point patterns. Spherical window $\Omega$ is shown in light green.

The concept of hyperuniformity was introduced by Torquato and Stillinger as an order metric for ranking point patterns according to their local density fluctuations [28]. Trivial examples of hyperuniform systems are crystals and quasi-crystals. In this thesis, we are mainly interested in isotropic, translationally disordered structures.

Since its introduction, hyperuniformity has been observed in many systems of practical and theoretical interest. Many of these are systems with hard, short-range interactions, most notably in maximally random jammed packings [36–38]. Random jammed packings were introduced by Torquato and Stillinger as a rigorous replacement to the historically prominent but ambiguous idea of "random close packing" [39]. Hyperuniform maximally random jammed packings include packings of spheres [36–38, 40], a class of smoothly shaped non-spherical particles [37, 38, 40], Platonic solids, ellipsoids, superballs and superellipsoids [41] and polydisperse hard disks [37]. In fact, long before the aforementioned maximally random jammed packings were shown to be hyperuniform, Torquato and Stillinger suggested that "all strictly jammed saturated infinite packings of identical spheres are hyperuniform" [28]. *Saturated packing* of hard spheres is defined as a packing in which there is no space available to add another sphere, e.g. in the case of saturated packings of identical hard spheres of unit

11

diameter, no point in space has distance greater than unity from the center of some sphere [28].

Other interesting examples of disordered hyperuniform systems include a one component plasma [42], strongly interacting systems of bosons such as liquid helium [43], spin-polarized fermionic ground states arising from determinantal point processes [44, 45], and the ground states of the so-called *stealthy* potentials [46], that enforce $S(k) = 0$ for a $k$ in a range $[0, k_C]$, by a collective coordinates approach [47]. An example of applications of hyperuniformity in cosmology is the Harrison-Zeldovich form of the primordial power spectrum [48, 49], that describes the matter fluctuations on the large-scale structure of the Universe. Hyperuniformity may play a role in determining the structural coloring of bird feathers and other biological tissues [50]. Beyond particle systems, the concept of hyperuniformity has been generalized to include random heterogeneous media [51].

Disordered hyperuniform systems are excellent candidates for materials with exotic properties [52, 53] and have been used to design novel photonic materials with tunable band-gaps [54–57]. Florescu, Torquato and Steinhardt conjectured that the band-gap properties of real amorphous materials are related to their degree of hyperuniformity [55]: "Although bounded variation [of density] may be sufficient to obtain a nonzero electronic band-gap, we conjecture that hyperuniform, tetrahedrally coordinated, continuous random networks have substantially larger electronic band-gaps than those that do not."de Graff and Thorpe on the other hand suggested that all amorphous tetrahedral networks have $S(k \to 0) \approx 0.035$ [21], and hence that hyperuniformity or even near hyperuniformity in continuous random networks is impossible. The reasoning of de Graff and Thorpe is based on an analysis of a $100,000$-atom sample of continuous random network and on the idea that the structure of amorphous silicon looks like a "frozen liquid" and hence the density fluctuations "freeze" at the freezing temperature. The frozen-liquid picture led them to conclude that $S(k \to 0)$

for a-Si is given by $S(k \to 0) = (\langle N^2 \rangle - \langle N \rangle^2)/\langle N \rangle = \rho k_B T \xi_T$, where $\rho$ is the number density, $T = T_g \approx 1100\,\mathrm{K}$ is the freezing temperature and $\chi_T$ is the isothermal compressibility of a-Si.

## 1.6 Pair Correlation Function

Any statistical system of $N$ identical particles confined to a volume $V$ is completely described in terms of the *configurational probability density function* $P(\mathbf{r}_1, \mathbf{r}_2, \cdots, \mathbf{r}_N)$, which is defined as a probability density of finding the system in configuration $\mathbf{r}_1, \mathbf{r}_2, \cdots, \mathbf{r}_N$. $P(\mathbf{r}_1, \mathbf{r}_2, \cdots, \mathbf{r}_N)$, contains all the information about the system, and thus it is too complex to be studied in practical samples with $N \gtrsim 10^3$, let alone in the thermodynamic limit in which $N \to \infty$. Instead, we define the *reduced configurational probability density function of rank n*, $P_n(\mathbf{r}_1, \mathbf{r}_2, \cdots, \mathbf{r}_n)$, which is defined as a probability density for any $n$-subset of the $N$ particles to occupy positions $\mathbf{r}_1, \mathbf{r}_2, \cdots, \mathbf{r}_n$. $P_n(\mathbf{r}_1, \mathbf{r}_2, \cdots, \mathbf{r}_n)$ is evaluated by counting the number of $n$-subsets of $N$ particles and integrating out the $\mathbf{r}_{n+1}, \cdots, \mathbf{r}_N$ variables, which leads to the following expression,

$$P_n(\mathbf{r}_1, \mathbf{r}_2, \cdots, \mathbf{r}_n) = n! \binom{N}{n} \int_V \cdots \int_V P(\mathbf{r}_1, \mathbf{r}_2, \cdots, \mathbf{r}_N) d\mathbf{r}_{n+1} \cdots d\mathbf{r}_N, \qquad (1.3)$$

where $V$ denotes the volume available to a single particle.

Aside from the trivial $P_0 = 1$ and $P_1 = \rho \equiv N/V$, the simplest reduced configuration density is of rank 2, $P_2(\mathbf{r}_1, \mathbf{r}_2)$. In a statistically homogeneous system, it is convenient to express the configurational variables in terms of the relative coordinate $\mathbf{r}_{21} = \mathbf{r}_2 - \mathbf{r}_1$ and the center of mass coordinate $\mathbf{r}_{CM} = [\mathbf{r}_1 + \mathbf{r}_2]/2$. We have $P_2(\mathbf{r}_1, \mathbf{r}_2) = P_2(\mathbf{r}_2 - \mathbf{r}_1, [\mathbf{r}_1 + \mathbf{r}_2]/2) = P_2(\mathbf{r}_{21}, \mathbf{r}_{CM})$, where we use the fact that $d\mathbf{r}_1 d\mathbf{r}_2 = d\mathbf{r}_{21} d\mathbf{r}_{CM}$. By integrating out the two-particle center of mass variable $\mathbf{r}_{CM}$ on which $P_2(\mathbf{r}_1, \mathbf{r}_2)$ does not depend, given the assumption of homogeneity, we

have $P_2(\mathbf{r}_1, \mathbf{r}_2) = P_2(\mathbf{r}_{21})$. In a statistically isotropic system, we may further write $P_2(\mathbf{r}_{21}) = P_2(|\mathbf{r}_{21}|) = P_2(r_{21})$ as the probability density depends only on the magnitude of the relative coordinate $r_{21} = \mathbf{r}_{21}$.

Physical quantities can be derived from *statistical operators* that are defined as functions of particle configuration $\mathbf{r}_1, \mathbf{r}_2, \cdots, \mathbf{r}_N$, i.e. $o = o(\mathbf{r}_1, \mathbf{r}_2, \cdots, \mathbf{r}_N)$. Every statistical operator can be expressed in terms an $n$-body operator expansion as

$$o(\mathbf{r}_1, \mathbf{r}_2, \cdots, \mathbf{r}_N) = o_0 + \sum_{i_1} o_1(\mathbf{r}_{i_1}) + \sum_{i_1, i_2} o_2(\mathbf{r}_{i_1}, \mathbf{r}_{i_1}) + \cdots + \sum_{i_1, i_2, \ldots, i_N} o_N(\mathbf{r}_{i_1}, \mathbf{r}_{i_2}, \cdots, \mathbf{r}_{i_N}),$$

(1.4)

where $o_n$ are $n$-body operators.

The ensemble average of an operator $o(\mathbf{r}_1, \mathbf{r}_2, \cdots, \mathbf{r}_N)$ is defined as

$$\langle o \rangle = \int_V \cdots \int_V o(\mathbf{r}_1, \mathbf{r}_2, \cdots, \mathbf{r}_N) P(\mathbf{r}_1, \mathbf{r}_2, \cdots, \mathbf{r}_N) d\mathbf{r}_1 \cdots d\mathbf{r}_N.$$

(1.5)

The ensemble average of an $n$-body operator depends only on the reduced configurational probability density function of rank $n$. Arguably the most important statistical operator is the *density operator* defined as

$$n_{\mathbf{r}}(\mathbf{r}_1, \mathbf{r}_2, \cdots, \mathbf{r}_N) = \sum_{i=1}^{N} \delta(\mathbf{r} - \mathbf{r}_i).$$

(1.6)

The ensemble average of the density operator is the density of the sample $\langle n_{\mathbf{r}} \rangle = \rho$. Comparison with the $n$-body operator expansion (1.4) reveals that the density operator is a one body statistical operator.

The *pair correlation function* is defined in terms of a density-density correlation function $\langle n_{\mathbf{r}_1} n_{\mathbf{r}_2} \rangle$ as

$$g(\mathbf{r}_1, \mathbf{r}_2) = \frac{\langle n_{\mathbf{r}_1} n_{\mathbf{r}_2} \rangle}{\rho^2} - \frac{\delta(\mathbf{r}_2 - \mathbf{r}_1)}{\rho}.$$

(1.7)

14

The second term subtracts the $\delta$-function self-correlation at $\mathbf{r}_1 = \mathbf{r}_2$. It follows from equation (1.7) that $g(\mathbf{r}_1, \mathbf{r}_2) \to 1$ as $|\mathbf{r}_2 - \mathbf{r}_1| \to \infty$. Since in statistically homogeneous isotropic systems the ensemble average depends only on the value of $P_2(r_{21})$, we have $g(\mathbf{r}_1, \mathbf{r}_2) = g(\mathbf{r}_2 - \mathbf{r}_1) = g(|\mathbf{r}_2 - \mathbf{r}_1|) = g(r_{21})$. Intuitively, the pair correlation function $g(r)$ represents a probability density of finding a particle at a distance $r$ from any other particle in the system.

## 1.7   Structure Factor

The structure factor can be defined as a Fourier transform of the density-density correlation function

$$
\begin{aligned}
S(\mathbf{k}) &= \frac{1}{NV} \int_V \int_V [\langle n_{\mathbf{r}_1} n_{\mathbf{r}_2} \rangle - \langle n_{\mathbf{r}_1} \rangle \langle n_{\mathbf{r}_2} \rangle] \exp[-i\mathbf{k} \cdot (\mathbf{r}_2 - \mathbf{r}_1)] d\mathbf{r}_1 d\mathbf{r}_2 \\
&= \frac{1}{N} \left[ \langle n_{\mathbf{k}} n_{-\mathbf{k}} \rangle - (2\pi)^3 \rho^2 \delta(\mathbf{k}) \right],
\end{aligned}
\tag{1.8}
$$

where $n_{\mathbf{k}}$ is the Fourier transform of the density operator, i.e.

$$
n_{\mathbf{k}} = \int_V n_{\mathbf{r}} \exp(-i\mathbf{k} \cdot \mathbf{r}) d\mathbf{r} = \sum_{j=1}^{N} \exp(-i\mathbf{k} \cdot \mathbf{r}_j).
\tag{1.9}
$$

Note that we have chosen to define the structure factor with the central peak subtracted.

In a homogeneous and isotropic sample, the structure factor $S(\mathbf{k})$ depends only on the magnitude of the wavenumber $k = |\mathbf{k}|$, so we have

$$
S(k) = 1 + \rho \int_0^\infty \int_0^\pi [g(r) - 1] \exp(-ikr \cos \theta) 2\pi r^2 \sin \theta \, d\theta \, dr,
\tag{1.10}
$$

which can be restated as

$$S(k) = 1 + 4\pi\rho \int_0^\infty r\left[g(r) - 1\right] \frac{\sin(kr)}{k} dr, \qquad (1.11)$$

which expresses an intimate relationship between the pair correlation function $g(r)$ and the structure factor $S(k)$ in a homogeneous isotropic media.

# Chapter 2

# Models of Amorphous Silicon

A s discussed in section 1.3, experimental probes do not directly provide all the information necessary to reconstruct the structure of a-Si, so microscopic structural models have been devised in order to understand its full three-dimensional structure. The most successful of these models are based on continuous random network (CRN) models [13, 58], first proposed by Zachariasen in 1932 [31]. In the following, we will present a survey of some of the most well known modeling methods that have gained a widespread use. These include CRN methods, molecular dynamics methods, empirical potentials methods, reverse Monte Carlo methods, and ab-initio density functional methods. There is still an enormous room for development of new algorithms and approaches to modeling a-Si and amorphous semiconductors in general.

## 2.1   Continuous Random Network Models

The idea of a continuous random network (CRN) was introduced in Zachariasen's seminal paper [31] more than 80 years ago. The key idea behind CRN models is that, on small scales, the local order of a-Si is close to that of c-Si, while a wide

spread in the dihedral angle distribution ensures that the atomic correlation decays sufficiently quickly (within the distance of several bond-lengths) to make the sample homogeneous and isotropic on large scales. The ideal continuous random network of a-Si is characterized by the following properties:

- each atom is four-fold coordinated (no dangling bonds or floating bonds)

- small spread in bond length and bond angle distributions

- wide spread in dihedral angle distribution

- no long-range order

- no crystalline regions

- no voids

Fig. 2.1 shows typical distributions of bond lengths, bond angles and dihedral angles in a CRN model. The distributions of bond lengths and bond angles are approximately Gaussian with $\sigma = 3.6\%$ for bond lengths and $\sigma = 8.61°$ for bond angles. The distribution of the dihedral bond angles is broad, with enhancements at $-60°$, $60°$, $180°$, arising from the staggered configurations of silicon atoms.

The early versions of the CRN models were made of sticks and balls, see Fig. 2.2. Polk demonstrated that there are no obstacles to constructing an arbitrarily large CRN by building a 440 atom CRN with about a 5% bond length and a 10% bond angle deviation, with no observable difference in the CRN structure between the central and outer regions [59, 60]. Using a computer program, the models were later relaxed [61] with the Keating potential and analyzed for their structural characteristics, including pair correlation functions, the dihedral angle distribution, the bond length and bond angle distributions, ring statistics [62], and the one-band electronic structure [63]. The CRN models were shown to be in a good agreement with experimental data in terms of the structure factor, the phonon density of states and the electronic structure;
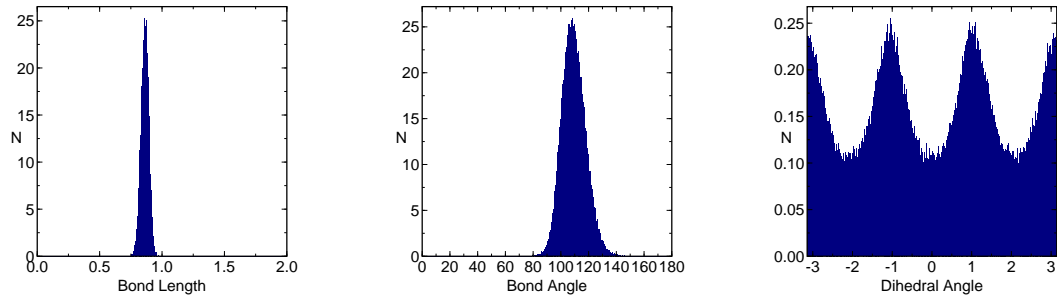
(a) Bond length histogram    (b) Bond angle histogram    (c) Dihedral angle histogram

Figure 2.1: Distribution of bond lengths, bond angles and dihedral angles in a typical continuous random network model. Bond lengths are normalized so that the unstretched value of Si-Si bond length is $\sqrt{3}/2$. Units on the vertical axis are arbitrary; dihedral angle is measured in radians.

however they failed to predict the behavior of the structure factor for small values of the wavevector.

Today, continuous random networks of sizes up to $100,000$ atoms are generated by an accelerated massively parallelized implementation of the Wooten, Winer, and Weaire (WWW) method, which uses a sequence of topological reconfigurations (bond switches) in order to achieve an amorphous, topologically disordered state. The WWW method bond switches are defined purely topologically. The Keating potential is used to evaluate the energy of a topological configuration.
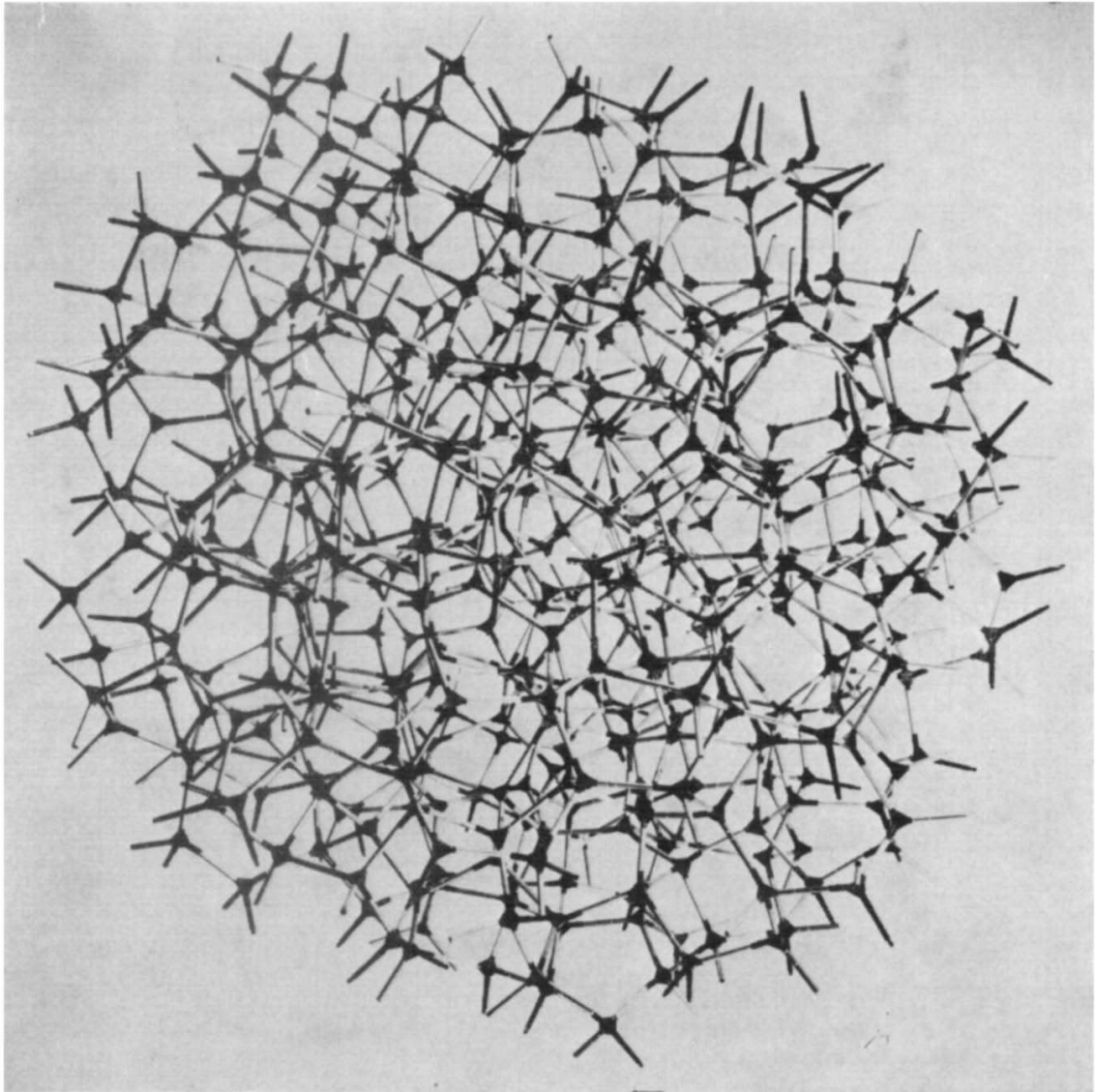
Figure 2.2: Polk sticks and balls model[1]

## 2.2 Keating Potential

The Keating potential [64–67] was originally proposed as an alternative to the strain potential of the Born-Huang approach of modeling elastic properties of tetrahedrally bonded crystals with diamond cubic lattice. The Keating potential contains two-body

[1]Courtesy of Polk, reproduced with permission of Elsevier

and three-body interactions, described by the formula

$$E = \frac{3}{16}\frac{\alpha}{d^2}\sum_{i,j}\left(\mathbf{r}_{ij}\cdot\mathbf{r}_{ij} - d^2\right)^2 + \frac{3}{16}\frac{\beta}{d^2}\sum_{i,j,k}\left(\mathbf{r}_{ij}\cdot\mathbf{r}_{ik} + \frac{1}{3}d^2\right)^2, \qquad (2.1)$$

where $\mathbf{r}_{ij} = \mathbf{r}_i - \mathbf{r}_j$, and $\mathbf{r}_i, \mathbf{r}_j$ denote the position vectors of a pair of bonded atoms, $d = 2.35\,\text{Å}$ is the mean length of the Si-Si bond, $\alpha = 2.965\,\text{eV}/\text{Å}^2$ is the overall energy scale, and $\beta = 0.285\alpha$ is determined from the crystalline phonon density of states of silicon. The first term of the Keating potential (bond stretching term) penalizes bonds for their deviation from their ideal unstrained value, while the second term (bond bending term) pushes bond angles towards the ideal tetrahedral angle $\theta_0 = \arccos(-1/3) \approx 109.47°$ of $sp^3$ hybridization. The Keating potential provides a good fit with experimental data on c-Si, including elastic coefficients, bulk modulus, and strain-energies [65, 66]. Models of a-Si based on the Keating potential are generally in good agreement with the pair correlation function $g(r)$ and the structure factor $S(k)$, except for a significant deviation at large distances $r$ and small wavevectors $k$ [21].

Evaluation of the Keating potential requires the knowledge of a bonding table i.e. a list of atomic pairs that are considered to be bonded. Since non-bonded atoms interacting with the Keating potential incur no penalty for being close, the Keating potential does not preclude the possibility that a pair of non-bonded atoms comes unphysically close together. This deficiency of the Keating potential can be remedied by altering the bonding table to make sure that all pairs of close atoms are always bonded.

## 2.3 Wooten, Winer, and Weaire Method of Generating Continuous Random Networks

The Wooten, Winer, and Weaire (WWW) method [68] was proposed as an efficient algorithm for constructing high quality CRNs. The method uses a sequence of bond transpositions, particular bond reconfigurations that alter the topology of the network while preserving the perfect four-fold coordination of each atom. The topology reconfiguration due to a bond transposition is illustrated in Fig. 2.3. The bonds between $A, A1$ and $B, B2$ are broken and replaced by bonds between $A, B2$ and $B, A1$ respectively, while the bond between $A, B$ is rotated by about $90°$. After each bond transposition, the configuration is relaxed with the Keating potential.

The starting point of the WWW technique is a perfectly four-coordinated network of atoms in a periodic box. This network is evolved through a sequence of bond switches, that are accepted with Hastings-Metropolis acceptance probability

$$p = \min \left[ 1, \exp \left( \frac{E_{\text{after}} - E_{\text{before}}}{k_B T} \right) \right], \tag{2.2}$$

where $E_{\text{before}}, E_{\text{after}}$ are the Keating energies before and after bond transposition respectively, $k_B$ is the Boltzmann constant and $T$ is the temperature. A sufficiently long evolution produces a thermal ensemble of configurations at temperature $T$.

Wooten et al. [68] demonstrated the practicality of their technique by generating a 216-atom sample with bond angle distribution of $11°$. Djordjević et al. [69] later used the WWW method to generate a 4096-atom model with the bond angle distribution of $10.5°$. Significant progress was achieved by Barkema and Mousseau [70], who proposed improvements to the WWW method that allowed them to generate a $100,000$-atom models with the bond angle distribution of $10°$. The improvements proposed by Barkema et al. include using local and non-local relaxation to reject unfavorable
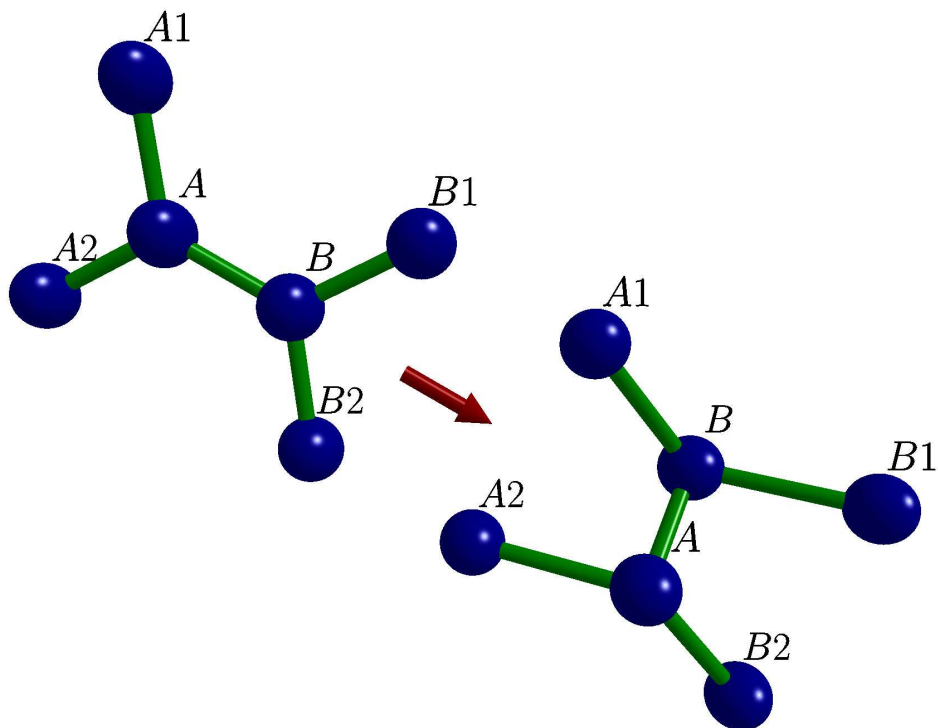
Figure 2.3: Bond transposition of the bond between atom $A$ and $B$. Bond transpositions represent a basic Monte-Carlo evolution step of the WWW method.

transpositions [70] and bulk synchronous parallelization scheme [71]. Barkema and Mousseau also proposed to start from a highly disordered liquid-like configuration to avoid any memory of an initial crystalline state. Connectivity of any liquid-like configuration can be assigned by an expanding loop method described in [70]. Fig. 2.4 illustrates the CRN network produced by the WWW method.

Evolution steps of the WWW method take the system from one local minimum of the Keating potential to another through the energy landscape of the system. This presents a notable advantage over molecular dynamics models, where many steps
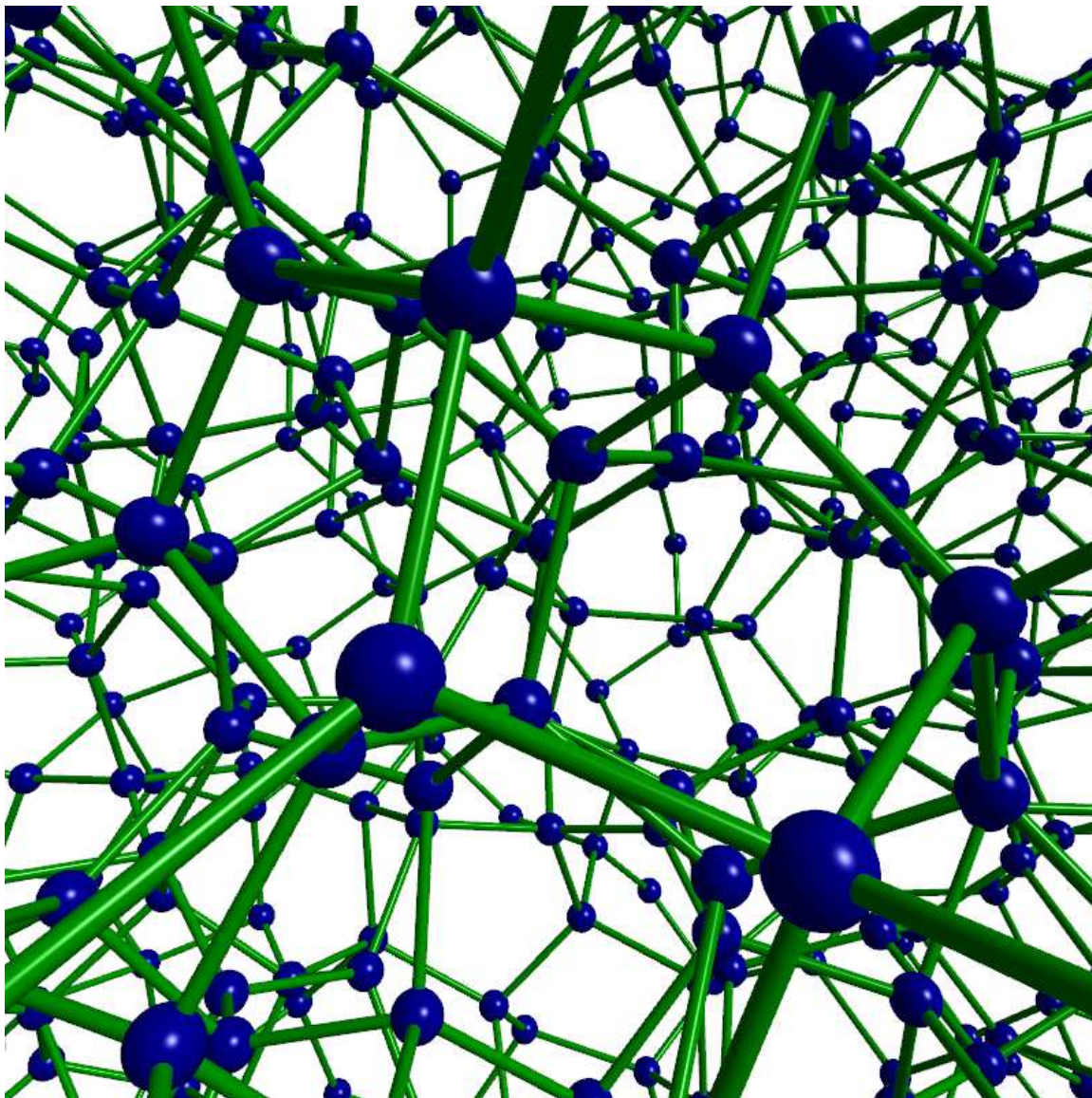
Figure 2.4: Small portion of a continuous random network model of a-Si generated by a WWW method

are taken before the system makes a transition between the states corresponding to different inherent structures [72, 73].

## 2.4  Empirical Classical Potentials

An accurate description of physical properties of solids, especially of the disordered ones requires a study of samples with sizes at least $3 - 10 \, \text{nm}$, or about $1000 - 100,000$ atoms. Ab-initio methods based on the density functional theory (DFT) can provide an accurate description of inter-atomic interactions which are necessary in these studies, but the computational complexity of ab-initio methods remains prohibitive given the size of the samples needed. An alternative to the quantum treatment of the DFT is to use empirical inter-atomic potentials, which are computationally much less expensive. Developing reliable empirical potentials that are much simpler than the full quantum treatment, yet capture the essential physics, is of crucial importance for the study of the structure and properties of materials.

Any classical potential for a statistical system of $N$ particles can be expressed as a sum of one-body, two-body, three-body, etc. terms (cluster expansion)

$$E = \sum_i v_1(\mathbf{r}_i) + \sum_{i,j} v_2(\mathbf{r}_i, \mathbf{r}_j) + \sum_{i,j,k} v_3(\mathbf{r}_i, \mathbf{r}_j, \mathbf{r}_k) + \cdots + v_N(\mathbf{r}_1, \mathbf{r}_2, \cdots, \mathbf{r}_N). \quad (2.3)$$

Although a purely two-body potential that stabilizes and self-assembles a diamond lattice has recently been proposed [74], because of the directional nature of $sp^3$ bonding orbitals a three-body potential is likely to be needed in order to model all properties of silicon that include the melting temperature, phonon spectra, and mechanical properties.

The Stillinger-Weber potential [75] involves two- and three- body interactions described by the following set of equations:

$$E_{SW} = \sum_{i,j} v_2(\mathbf{r}_i, \mathbf{r}_j) + \sum_{i,j,k} v_3(\mathbf{r}_i, \mathbf{r}_j, \mathbf{r}_k), \quad (2.4)$$

$$v_2(r_{ij}) = \varepsilon f_2\left(r_{ij}/\sigma\right), \tag{2.5}$$

$$v_3(r_{ij}, r_{ik}, \cos\theta) = \varepsilon f_3\left(r_{ij}/\sigma, r_{ik}/\sigma, \cos\theta_{ijk}\right), \tag{2.6}$$

where $r_{ij} = |\mathbf{r}_j - \mathbf{r}_i|$, $r_{ik} = |\mathbf{r}_k - \mathbf{r}_i|$, $\theta_{ijk}$ is the angle between the vectors $\mathbf{r}_j - \mathbf{r}_i$ and $\mathbf{r}_k - \mathbf{r}_i$, and

$$f_2(r) = \begin{cases} A(Br^{-p} - r^{-q})\exp\left[(r-a)^{-1}\right] & r < a \\ 0 & r \geq a \end{cases} \tag{2.7}$$

$$f_3(r_{ij}, r_{ik}, \theta_{ijk}) = \begin{cases} \lambda\exp\left[\gamma(r_{ij}-a)^{-1} + \gamma(r_{ik}-a)^{-1}\right]\left(\cos\theta_{ijk} + \tfrac{1}{3}\right)^2 & r_{ij} < a \text{ and } r_{ik} < a \\ 0 & r_{ij} \geq a \text{ or } r_{ik} \geq a. \end{cases} \tag{2.8}$$

Table 2.1 shows the original crystalline parameters of the Stillinger-Weber potential in the first column and the modified parameters that were determined by fitting to the phonon spectra of a-Si [76] in the second column. Crystalline parameters were obtained by fitting the c-Si model to the experimentally obtained cohesive energy and melting temperature. The amorphous parameters were obtained by fitting the positions of the transverse acoustic (TA) and transverse optic (TO) peaks of the a-Si phonon spectra [76].

| | Stillinger-Weber crystalline | Stillinger-Weber amorphous |
|---|---|---|
| $\sigma$ | 0.20951 nm | 0.20951 nm |
| $\varepsilon$ | 2.16826 eV | 1.64833 eV |
| $A$ | 7.049556277 | 7.049556277 |
| $B$ | 0.6022245584 | 0.6022245584 |
| $p$ | 4 | 4 |
| $q$ | 0 | 0 |
| $a$ | 1.80 | 1.80 |
| $\lambda$ | 21.0 | 31.5 |
| $\gamma$ | 1.20 | 1.20 |

Table 2.1: Stillinger-Weber potential parameters

Fig. 2.5 shows the two-body and three-body functions of the Stillinger-Weber potential. $V_2(r)$ is the two-body potential term and $V_3(r)$ is the radial part of the three body potential term.

The Tersoff potentials [77–79] are a family of *bond order potentials*, a class of potentials whose bond-strength depends on the local environment. The dependence of bond-strength on the local environment allows the Tersoff potentials to accurately describe the non-tetrahedrally bonded atoms (bonding defects) in a-Si. The Tersoff potentials are described by the following set of formulas.

$$E_T = \sum_{ij} v_2(\mathbf{r}_i, \mathbf{r}_j), \tag{2.9}$$

where $v_2$ has the form of a Morse pair potential

$$v_2(\mathbf{r}_i, \mathbf{r}_j) = f_c(r_{ij}) \left[ A \exp(-\lambda_1 r_{ij}) - B(\mathbf{r}_i, \mathbf{r}_j) \exp(-\lambda_2 r_{ij}) \right]. \tag{2.10}$$
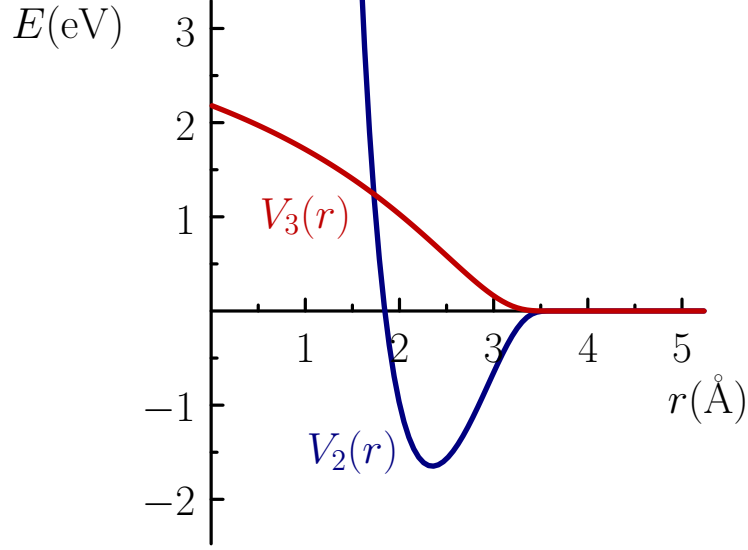
Figure 2.5: Illustration of the Stillinger-Weber potential. The two-body potential term, $V_2(r)$ is shown in dark blue; the radial part of the three-body potential term, $V_3(r)$ is shown in red.

Deviations of the Tersoff potential from a pair potential are derived from the dependence of $B(\mathbf{r}_i, \mathbf{r}_j)$ on the local environment. $B(\mathbf{r}_i, \mathbf{r}_j)$ is given by

$$B(\mathbf{r}_i, \mathbf{r}_j) = B_0 \exp\left(-z_{ij}/b\right), \tag{2.11}$$

$$z_{ij} = \sum_{k \neq i,j} \left[\frac{w(r_{ik})}{w(r_{ij})}\right]^n \left[c + \exp(-d \cos\theta_{ijk})\right]^{-1}, \tag{2.12}$$

where $r_{ij} = |\mathbf{r}_j - \mathbf{r}_i|$, $\theta_{ijk}$ is the angle between the vectors $\mathbf{r}_j - \mathbf{r}_i$ and $\mathbf{r}_k - \mathbf{r}_i$, and $w(r)$ is given by

$$w(r) = f_c(r) \exp(-\lambda_2 r), \tag{2.13}$$

where $f_c(r)$ is a cutoff function that restricts the range of the potential

$$f_c(r) = \begin{cases} 1 & r \leq R - D, \\ \frac{1}{2} - \frac{1}{2} \sin\left[\frac{\pi(r-R)}{D}\right] & R - D < r < R + D, \\ 0 & r \geq R + D. \end{cases} \tag{2.14}$$

$z_{ij}$ is a weighted measure of the number of bonds competing with the bond $ij$, and $b$ determines how rapidly the bond strength falls off with increasing effective coordination [77]. $A, B_0, \lambda_1, \lambda_2, b, c, d, n, R, D$ are parameters of the Tersoff potential determined by fitting to the properties of c-Si.

| parameter | $A$ | $B_0$ | $\lambda_1$ | $\lambda_2$ | $b$ | $c$ | $d$ | $n$ | $R$ | $D$ |
|-----------|-----|-------|-------------|-------------|-----|-----|-----|-----|-----|-----|
| value | $2280\,\mathrm{eV}$ | $171\,\mathrm{eV}$ | $2\lambda_2$ | $1.465\,\mathrm{\AA}^{-1}$ | $1.324$ | $6.5$ | $6.02$ | $4$ | $3.0\,\mathrm{\AA}$ | $0.2\,\mathrm{\AA}$ |

Table 2.2: Tersoff potential parameters

Another class of empirical potentials are the *environment-dependent interatomic potentials (EDIP)* [80–83]. The EDIP potential was constructed using an analysis of elastic properties for the diamond crystalline structure and inversions of ab-initio cohesive energy curves. The EDIP potential includes two- and three-body terms which depend on the local atomic environment through an effective coordination number. The EDIP potential takes the following form

$$E_{EDIP} = \sum_{ij} v_2(r_{ij}, Z_i) + \sum_{ijk} v_3(r_{ij}, r_{ik}, Z_i), \tag{2.15}$$

$$Z_i = \sum_{j \neq i} f(r_{ij}) \tag{2.16}$$

where $f(r_{ij})$ is a weight function that measures the contribution of neighbor $j$ to the coordination of atom $i$ in terms of interatomic separation $r_{ij}$. The neighbor function is 1 for $r \leq c$ and 0 for large inter-atomic separations $r$.

$$f(r) = \begin{cases} 1 & r \leq a, \\ \exp\left(\frac{\alpha}{1-x^{-3}}\right) & c < r < a, \\ 0 & r \geq b, \end{cases} \tag{2.17}$$

$$x = \frac{r-c}{b-c}. \tag{2.18}$$

The two-body potential takes the following form

$$
v_2(r_{ij}, Z_i) =
\begin{cases}
A \left[ \left( \frac{B}{r_{ij}} \right) - \exp\left( -\beta Z_i^2 \right) \right] \exp\left( \frac{\sigma}{r_{ij} - a} \right) & r < a, \\
0 & r \geq a.
\end{cases}
\tag{2.19}
$$

The three-body potential contains the radial cutoff function and angular factor

$$
v_3(r_{ij}, r_{ik}, Z_i) = g(r_{ij})g(r_{ik})h(\cos\theta_{ijk}, Z_i),
\tag{2.20}
$$

where

$$
g(r) =
\begin{cases}
\exp\left( \frac{\gamma}{r - b} \right) & r < b, \\
0 & r \geq b.
\end{cases}
\tag{2.21}
$$

$$
h(\cos\theta_{ijk}, Z_i) = \lambda \left\{ 1 - \exp\left[ -Q(Z_i) \left( \cos\theta_{ijk} + \tau(Z_i) \right)^2 \right] \right\},
\tag{2.22}
$$

$$
Q(Z_i) = Q_0 \exp\left( -\mu Z_i \right),
\tag{2.23}
$$

$$
\tau(Z_i) = u_1 + u_2 \left[ u_3 \exp(u_4 Z_i) - \exp(-2 u_4 Z_i) \right],
\tag{2.24}
$$

and where $A, B, \rho, \beta, \sigma, a, b, c, \lambda, \gamma, Q_0, \mu, \alpha, u_1, u_2, u_3, u_4$ are parameters. See [82] for the values that were obtained by fitting to ab-initio DFT results including lattice sums, elastic constants, and energies of point defects.

## 2.5    Molecular Dynamics Models

Molecular dynamics models simulate the motion of atoms interacting with a classical potential and evolving under Newtonian dynamics. For a system of $N$ particles with

positions $\mathbf{r}_i(t)$ and velocities $\mathbf{v}_i(t)$, the Newtonian dynamics is given by

$$\frac{d\mathbf{r})_i}{dt} = \mathbf{v}_i, \tag{2.25}$$

$$\frac{d\mathbf{v}_i}{dt} = \mathbf{a}_i(t), \tag{2.26}$$

$$\mathbf{a}_i = -\frac{1}{m}\nabla_i V(\mathbf{r}_1, \cdots, \mathbf{r}_N). \tag{2.27}$$

A suitable integration scheme has to be chosen to numerically solve the system of ordinary differential equations (2.27). The simplest integration scheme is the Euler scheme, which integrates the equations by

$$\mathbf{r}_i(t + \Delta t) = \mathbf{r}_i(t) + \mathbf{v}_i(t)\Delta t, \tag{2.28}$$

$$\mathbf{v}_i(t + \Delta t) = \mathbf{v}_i(t) + \mathbf{a}_i(t)\Delta t, \tag{2.29}$$

$$\mathbf{a}_i(t) = -\frac{1}{m}\nabla_i V(\mathbf{r}_1(t), \cdots, \mathbf{r}_N(t)). \tag{2.30}$$

An example of a commonly used scheme is the two step Verlet algorithm [84, 85] that consists of the following steps:

$$\mathbf{r}_i(t + \Delta t) = \mathbf{r}_i(t) + \mathbf{v}_i(t)\Delta t + \frac{1}{2}\mathbf{a}_i(t)(\Delta t)^2, \tag{2.31}$$

$$\mathbf{v}_i(t + \Delta t) = \mathbf{v}_i(t) + \frac{1}{2}[\mathbf{a}_i(t) + \mathbf{a}_i(t + \Delta t)]\Delta t, \tag{2.32}$$

$$\mathbf{a}_i(t) = -\frac{1}{m}\nabla_i V(\mathbf{r}_1(t), \cdots, \mathbf{r}_N(t)). \tag{2.33}$$

The popularity of the Verlet algorithm stems from ease of implementation and good convergence properties (the Verlet algorithm has $O(\Delta t^4)$ convergence).

Models of amorphous silicon obtained by molecular dynamics simulation of rapid quenching starting from a sufficiently high temperature thermal state provide a good fit for the radial distribution function, but suffer from a significant number of overcoordinated atoms (atoms with more than 4 neighbors in their first coordination shell,

i.e. floating bonds) and undercoordinated atoms (atoms with less than 4 neighbors in their first coordination shell, i.e. dangling bonds) [86–88]. Depending on the speed of the quenching and the potential used, molecular dynamics models predict the concentration of coordination defects to be 5% to 10%. Experimentally, the number of coordination defects can be reliably measured by electron paramagnetic resonance experiments (EPR), which are very sensitive to defects in a-Si by detecting unpaired spins of electrons. The EPR experiments point to a negligible number of coordination defects - less than 0.1% [29, 89, 90], which means that molecular dynamics models are ruled out as viable models of amorphous silicon.

## 2.6 Simulated Annealing

Simulated annealing is a stochastic Monte Carlo simulation procedure, which consists of randomly selected transitions between two states of a model according to the Metropolis transition probability [91]

$$p_{ij} = \min\left[1, \exp\left(\frac{E_j - E_i}{k_B T}\right)\right], \tag{2.34}$$

Here $E_i, E_j$ are energies of the $i-$th and $j-$th states respectively and $T$ is the temperature.

The model evolved under the Metropolis transition probabilities represents a discrete time Markov chain, which satisfies the detailed balance condition and is assumed to be transitive, i.e. every state in the configuration is reachable as required by ergodicity. By the Markov ergodic convergence theorem, the probability distribution converges to an equilibrium state in which the probability of a configuration is given by the Boltzmann distribution, i.e. the probability of the $n-$th state is

$$P_n = \frac{\exp\left(-\frac{E_n}{k_B T}\right)}{Z}, \tag{2.35}$$

where

$$Z = \sum_n \exp\left(-\frac{E_n}{k_B T}\right).$$ (2.36)

A deep local minimum in the energy landscape of the model can be found by quasi-statically lowering temperature from a high temperature $T = T_{\max}$ to $T = 0$ according to a predetermined annealing schedule. This choice of an annealing schedule is critical to the efficiency of the algorithm. Popular choices of annealing schedule include the logarithmic annealing schedule defined by $T(n_{\text{step}}) = c/\log(1 + n_{\text{step}})$ and the inverse linear annealing schedule defined by $T(n_{\text{step}}) = c/(1 + n_{\text{step}})$, where $n_{\text{step}}$ denotes the number of steps taken in the current state of the simulation and $c$ is a constant. Using the theory of Markov chains, it can be shown that simulated annealing using logarithmic temperature schedule $T(n_{\text{step}}) = c/\log(1 + n_{\text{step}})$ will eventually reach the global minimum provided that the constant $c$ is larger than the depth of the deepest local minimum which is not a global minimum [92]. While the logarithmic annealing schedule always succeeds in finding a global minimum, the logarithmic convergence is not practical. Faster annealing schedules may not converge to the global minimum but rather to a deep local minimum, representing an amorphous state.

Simulated annealing is at the core of the Wooten, Winer, and Weaire method for generating CRN models of a-Si. Apart from modeling a-Si, it was successfully employed to model many other amorphous materials, including a-Si, a-Ge, a-SiO$_2$, a-Se, a-H$_2$O and polymers. Simulated annealing is commonly used as an efficient optimization method [93, 94].

## 2.7 Tight Binding Models

Tight binding models represent the simplest quantum mechanical models of solids. The quantum mechanical treatment is restricted to the valence electrons (the electrons responsible for bonding), which are treated as independent and uncorrelated.

In the tight binding approximation, electronic eigenstates are represented as a linear combination of atomic orbitals (LCAO), which leads to the wavefunction of the following form

$$|\psi\rangle = \sum_{i,\alpha} c_{i\alpha} |\phi_{i\alpha}\rangle, \tag{2.37}$$

where $|\phi_{i\alpha}\rangle$ represent atomic orbitals with $i$ indexing silicon atoms and $\alpha$ indexing valence orbitals of a particular silicon atom, i.e. $3s, 3p_x, 3p_y, 3p_z$ orbitals of the $1s^2 2s^2 2p^6 3s^2 3p^2$ electronic configuration of silicon atoms. The tight binding method approximates the full many-body Hamiltonian by an effective one body Hamiltonian matrix, whose eigenstates correspond to the electronic states of independent valence electrons. In the *two center approximation*, overlaps between three or more orbitals are neglected, so the Hamiltonian is completely determined by the following transfer (hopping) matrix elements between two overlapping orbitals

$$H_{i\alpha j\beta} = \langle i\alpha|H|j\beta\rangle = \int \phi_{i\alpha}^* H \phi_{j\beta} d\mathbf{r}. \tag{2.38}$$

Similarly, inner products of wavefunctions are completely determined by the following matrix of overlap matrix integrals.

$$S_{i\alpha j\beta} = \langle i\alpha|j\beta\rangle = \int \phi_{i\alpha}^* \phi_{j\beta} d\mathbf{r}. \tag{2.39}$$

An orthonormal basis of $|\phi_{i\alpha}\rangle$ is often used, as it leads to a simple form of overlap matrix integrals $S_{i\alpha j\beta} = \delta_{ij}\delta_{\alpha\beta}$.

The interatomic portion of the transfer and overlap matrices can be expressed in the Slater-Koster basis [95] in terms of the rotationally invariant elements

$a_{ss\sigma}, a_{sp\sigma}, a_{pp\sigma}, a_{pp\pi}$ as

$$A = \begin{pmatrix} a_{ss\sigma} & n_x a_{sp\sigma} & n_y a_{sp\sigma} & n_z a_{sp\sigma} \\ -n_x a_{ss\sigma} & a_{pp\pi} + n_x n_x (a_{pp\sigma} - a_{pp\pi}) & n_x n_y (a_{pp\sigma} - a_{pp\pi}) & n_x n_z (a_{pp\sigma} - a_{pp\pi}) \\ -n_y a_{ss\sigma} & n_y n_x (a_{pp\sigma} - a_{pp\pi}) & a_{pp\pi} + n_y n_y (a_{pp\sigma} - a_{pp\pi}) & n_y n_z (a_{pp\sigma} - a_{pp\pi}) \\ -n_z a_{ss\sigma} & n_z n_x (a_{pp\sigma} - a_{pp\pi}) & n_z n_y (a_{pp\sigma} - a_{pp\pi}) & a_{pp\pi} + n_z n_z (a_{pp\sigma} - a_{pp\pi}) \end{pmatrix}.$$

(2.40)

Here $A$ stands for the transfer matrix $H$ or the overlap matrix $S$ and $a_{ss\sigma}, a_{sp\sigma}, a_{pp\sigma}, a_{pp\pi}$ stand for the two-center Slater-Koster transfer elements $h_{ss\sigma}, h_{sp\sigma}, h_{pp\sigma}, h_{pp\pi}$ or the two-center Slater-Koster overlap elements $s_{ss\sigma}, s_{sp\sigma}, s_{pp\sigma}, s_{pp\pi}$ respectively, and $n_x, n_y, n_z$ are components of the unit vector in direction $\mathbf{r}_2 - \mathbf{r}_1$, stretching between the two bonded atoms. The elements $a_{ss\sigma}, a_{sp\sigma}, a_{pp\sigma}, a_{pp\pi}$ are rotationally invariant and have the symmetry of $\sigma$ or $\pi$ bonds (see Fig. 2.6 (a)-(d), for illustration). The intra-atomic portion of the transfer and overlap matrix is taken to be diagonal and by symmetry can be parametrized as

$$B = \begin{pmatrix} b_{ss} & 0 & 0 & 0 \\ 0 & b_{pp} & 0 & 0 \\ 0 & 0 & b_{pp} & 0 \\ 0 & 0 & 0 & b_{pp} \end{pmatrix}, \qquad (2.41)$$

where $b_{ss} = b_{pp} = 1$ for the overlap matrix elements and $b_{ss} = E_s$, $b_p = E_p$ for transfer matrix elements. $E_s$ and $E_p$ denote the energy levels of the $s$ and $p$ orbitals respectively.

The eigenstates of the Hamiltonian are the critical points of the following variational functional

$$\mathcal{E}[\psi] = \int \psi^* H \psi d\mathbf{r} - \epsilon \int \psi^* \psi d\mathbf{r}. \qquad (2.42)$$

(a) $a_{ss\sigma}$

(b) $a_{sp\sigma}$

(c) $a_{pp\sigma}$

(d) $a_{pp\pi}$
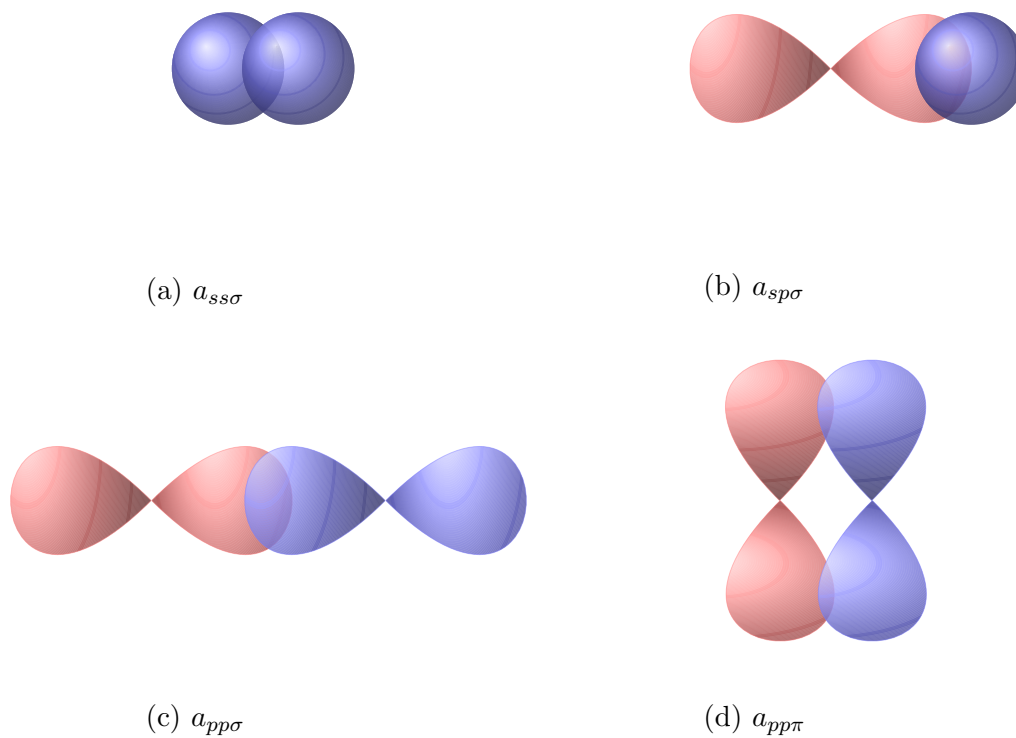
Figure 2.6: Orbital overlaps

In the subspace of one-electron orbitals of the form $|\psi\rangle = \sum_{i,\alpha} c_{i\alpha} |\phi_{i\alpha}\rangle$, the critical points satisfy

$$H_{i\alpha j\beta}\, c_{j\beta} = \epsilon S_{i\alpha j\beta}\, c_{j\beta}. \tag{2.43}$$

The coefficients $c_{i\alpha}$ are obtained by the Löwdin transformation method, which requires an eigendecomposition of $S$ and solving for eigenvalues of matrix $H$ with inner product specified by $S$. Once the eigenvalues of (2.43) are known, the electronic part of the configurational energy (band energy) is obtained by summing the eigenenergies of the Hamiltonian from the lowest energy state up to the Fermi level,

$$E_{\text{electrons}} = 2 \sum_{\substack{\text{occupied} \\ \text{states}}} \epsilon_s, \tag{2.44}$$

where $\epsilon_s$ denotes the energy of an electronic state, the factor of 2 takes into account the spin degeneracy of the states and the sum is performed of the filled states (e.g. lower half of the spectrum).

The total energy of the atomic configuration consists of the band energy and the energy of the ionic repulsion between the atoms. The energy of the ion repulsive interaction can be modeled by a two-body empirical potential

$$E_{\text{ions}} = \sum_{i,j} v_2(r_{ij}), \tag{2.45}$$

or by a many body potential such as

$$E_{\text{ions}} = \sum_i f\left(\sum_j \phi_2(r_{ij})\right). \tag{2.46}$$

The total energy of the configuration is then expressed as

$$E = E_{\text{electrons}} + E_{\text{ions}} + N_{\text{atoms}} E_0, \tag{2.47}$$

where $N_{\text{atoms}}$ is the number of atoms and $E_0$ is an intrinsic energy associated with a silicon atom.

Energy of the configuration can be used to evaluate forces on atoms using a formula

$$F = -\frac{d}{dR}E_{\text{electrons}} - \frac{d}{dR}E_{\text{ions}} = -\sum_{i\alpha j\beta}\left(\frac{dH_{i\alpha j\beta}}{dR} - E_{\text{electrons}}\frac{dS_{i\alpha j\beta}}{dR}\right) - \frac{d}{dR}E_{\text{ions}}, \tag{2.48}$$

which in turn can be used as an input of molecular dynamics model or a relaxation.

The eigenenergies can be used to determine the size of an electronic band gap. The major limitation of the tight binding method is the need for an eigendecomposition of an $n \times n$ matrix, with $n = N_{\text{atoms}} N_{\text{orbitals}}$, where $N_{\text{atoms}}$ is the number of silicon atoms and $N_{\text{orbitals}}$ is the number of atomic orbitals per atom. Since the

computational complexity of the matrix diagonalization is $O(n^3)$, the use of the tight binding approximation is impractical for systems with more than about 1000 atoms.

A physically motivated parametrization of the transfer and overlap elements that successfully predicts the size of the band gap in c-Si was given by Kwon [96, 97]. The Kwon method uses an orthonormal set of orbitals, so that $S_{i\alpha j\beta} = 1$ for orbitals of the same type on the same site and $S_{i\alpha,j\beta} = 0$ otherwise. In this model, inter-atomic transfer matrix elements are parametrized as

$$h_\alpha(r) = h_\alpha(r_0) \left(\frac{r_0}{r}\right)^n \exp\left(n\left[-\left(\frac{r}{r_{c\alpha}}\right)^{n_{c\alpha}} + \left(\frac{r_0}{r_{c\alpha}}\right)^{n_{c\alpha}}\right]\right), \tag{2.49}$$

where the subscript $\alpha$ denotes the four possible types of interatomic hopping, i.e. $ss\sigma$, $sp\sigma$, $sp\pi$, $pp\pi$. The intra-atomic transfer matrix elements are parametrized as $h_{ss} = E_s$, $h_{pp} = E_p$.

The ionic repulsion is modeled according to equation (2.46) with

$$f(x) = C_1 x + C_2 x^2 + C_3 x^3 + C_4 x^4, \tag{2.50}$$

and $\phi_2(r)$ given by

$$\phi_2(r) = \left(\frac{r_0}{r}\right)^m \exp\left(m\left[-\left(\frac{r}{r_{c\alpha}}\right)^{m_c} + \left(\frac{r_0}{r_c}\right)^{m_c}\right]\right). \tag{2.51}$$

The $h_\alpha(r_0), r_{c\alpha}, r_c, r_0, n, n_{c\alpha}, m, m_c, E_s, E_p, E_0, C_i$ are parameters of the model that were fitted to experimental data shown in the following table:

| off-diagonal transfer elements parameters | | | | |
|---|---|---|---|---|
| $\alpha$ | $ss\sigma$ | $sp\sigma$ | $pp\sigma$ | $sp\pi$ |
| $h_\alpha(r_0)/$eV | $-2.038$ | $1.745$ | $2.75$ | $-1.075$ |
| $n_{c\alpha}$ | $9.5$ | $8.5$ | $7.5$ | $7.5$ |
| $r_{c\alpha}$ | $3.4$ | $3.55$ | $3.7$ | $3.7$ |
| diagonal transfer elements parameters | | | | |
| $E_s/$eV | $E_p/$eV | $E_0/$eV | | |
| $-5.25$ | $1.20$ | $8.7393204$ | | |
| other electronic parameters | | | | |
| $r_0/$nm | | $n$ | | |
| $0.235$ | | $2$ | | |
| ion repulsion function parameters | | | | |
| $C_1/$eV | $C_2/$eV | $C_3/$eV | $C_4/$eV | |
| $2.1604385$ | $-0.1384393$ | $5.8398423 \times 10^{-3}$ | $-8.0263577 \times 10^{-5}$ | |
| ion repulsion potential parameters | | | | |
| $m$ | $m_c$ | $r_c/$Å | | |
| $6.8755$ | $13.017$ | $3.66995$ | | |

Table 2.3: Parameters of the Kwon model [96]

An example of a parametrization that uses a non-orthogonal set of orbitals includes a model proposed by Bernstein et al. [98]. For more details on the tight binding method, see [99].

## 2.8 Reverse Monte Carlo Models

Reverse Monte Carlo models result from an attempt to create a structural model that optimizes fit to experimental data with no assumption of the underlying physics. In the Reverse Monte Carlo models, physically motivated configuration energy is replaced by an artificial energy function that measures the distance of the configuration dependent quantities from the corresponding experimentally measured data points [100, 101]

$$E_{RMC} = \sum_i \left[ x_i(\mathbf{r}_1, \mathbf{r}_2 \cdots \mathbf{r}_N) - x_{i,\text{obs}} \right]^2. \tag{2.52}$$

Here $x_{i,\text{obs}}$ denotes an experimentally measured quantity, $x_i(\mathbf{r}_1, \mathbf{r}_2 \cdots \mathbf{r}_N)$ the same quantity calculated from the configuration of the model, and $i$ indexes the different measured quantities. The Metropolis-Hasting algorithm can be used to find a configuration that represents a local minimum of $E_{RMC}$.

In the case of a-Si, the experimentally measured quantities are typically either the structure factor $S(k)$ obtained from the diffraction experiments or the pair correlation function $g(r)$ obtained from $S(k)$. In these cases it is desirable to add a physical, short range inter-atomic interaction to $E_{RCM}$ to break a high degeneracy of $E_{RMC}$ that is a result of many different atomic configurations giving rise to the same values of $g(r)$ or $S(k)$.

The reverse Monte Carlo methods are successful in reproducing the data contained in the energy function, but often fail to fit other experimental data. An impressive fit of the experimental data is not necessarily a virtue of the reverse Monte Carlo methods, since the data are often fitted to a higher precision than that of the data itself, which is a sign of too many parameters in the model.

The major problem of the reverse Monte Carlo methods is that often very different configurations can fit the same experimental data. Stillinger proved that the number of inherent structures grows exponentially with the system size [102]. Con-

sequently, the reverse Monte Carlo methods have a low predictive power, due to the large number of possible configurations that fit the experimental data well, resulting from the structural degeneracy. Lack of a physical realistic mechanism that selects the correct inherent structure presents a serious shortcoming of the reverse Monte Carlo methods.

## 2.9   Density Functional Theory Models

Density functional theory (DFT) models represent the electronic energy of a configuration as a functional depending only on the electron charge density, i.e. $E_{el.} = E_{el.}[\rho]$, where the density $\rho$ is given by

$$\rho(\mathbf{r}_1) = N_{el.} \int d\mathbf{r}_2 \cdots d\mathbf{r}_N \, \||\Psi(\mathbf{r}_1, \cdots, \mathbf{r}_N)\rangle\|^2 . \qquad (2.53)$$

Here $N_{el.} = \int d^3\mathbf{r}\rho(\mathbf{r})$ is the number of electrons in the system. The ground state of the electrons minimizes the energy functional. The DFT electronic energy functional is approximated as

$$E_{el.}[\rho] = q \int d^3\mathbf{r}\phi(\mathbf{r})\rho(\mathbf{r}) + q^2/2 \int d^3\mathbf{r}d^3\mathbf{r}'\frac{\rho(\mathbf{r})\rho(\mathbf{r}')}{|\mathbf{r} - \mathbf{r}'|} + T_{el.}(\rho) + E_{el.}^{exch.}, \qquad (2.54)$$

where $q$ is the charge of electron, $\phi(\mathbf{r})$ is an external potential, $T_{el}(\rho)$ is the kinetic energy of the electrons, and $E_{el.}^{exch.}$ is the exchange-correlation term, which models the quantum effects of interacting electrons.

The simplest method of approximating the exchange-correlation term is the local density approximation (LDA). In the LDA approximation, $E_{el.}$ depends only on the local density $\rho(\mathbf{r})$ (not on the derivatives of $\rho(\mathbf{r})$), so that $E_{el.}$ can be expressed as $E_{el.}^{exch.LDA} = \int d^3\mathbf{r}\rho(\mathbf{r})\epsilon_{el.}^{exch.}$. The exchange-correlation energy density $\epsilon_{el.}^{exch.}$ can be obtained as $\epsilon_{el.}^{exch.} \approx hc \left(-\frac{0.458}{r_s}R_\infty^2 - \frac{0.44}{r_s+7.8R_\infty}R_\infty^2\right)$ by approximating the electrons as

homogeneous electron gas (jellium) [103, 104]. Here $r_s$ is the Wigner-Seits radius defined by $r_s = \left(\frac{3}{4\pi\rho}\right)^{1/3}$ and $R_\infty = \frac{m_e e^4}{8\varepsilon_0^2 h^3 c}$ is the Rydberg constant.

The kinetic energy can be evaluated using the Kohn-Sham orbitals $|\psi_i\rangle$ as

$$T_{el}(\rho) = \sum_i \langle\psi_i| - \hbar/2m\nabla^2|\psi_i\rangle, \tag{2.55}$$

where the Kohn-Sham orbitals $|\psi_i\rangle$ corresponding to energy $\varepsilon_i$ labeled by index $i$ are found by solving the Kohn-Sham equation [105]

$$-\hbar^2\nabla^2|\psi_i\rangle + V_{\text{eff}}(\mathbf{r})|\psi_i\rangle = \varepsilon_i|\psi_i\rangle, \tag{2.56}$$

where $V_{eff}$ is defined as

$$V_{\text{eff}}(\mathbf{r}) = V(\mathbf{r}) + q^2 \int d^3\mathbf{r}' \frac{\rho(\mathbf{r}')}{|\mathbf{r} - \mathbf{r}'|} + \frac{\delta\epsilon_{el.}^{exch.}}{\delta\rho}, \tag{2.57}$$

and the electronic density is

$$\rho(\mathbf{r}) = \sum_{\substack{\text{occupied} \\ \text{states}}} \||\psi_i\rangle\|^2. \tag{2.58}$$

Besides the electronic energy, a configuration also carries an ionic energy

$$E_{ion.} = \frac{1}{2}\sum_{i\neq j} \frac{q_i q_j}{r_{ij}}, \tag{2.59}$$

where $q_i$ denotes the electric charge of $i$-th ion, $\mathbf{r}_i$ denotes the position of $i$-th ion, and $r_{ij} = |\mathbf{r}_j - \mathbf{r}_j|$.

The DFT equations form a set of nonlinear integro-differential equations that can be solved iteratively, where each step of the iteration requires the diagonalization of a Hermitian $N \times N$ matrix. Here $N$ is the number of Kohn-Sham orbitals consid-

ered. While the DFT models can provide most accurate ways to calculate energies of configurations, the computational complexity of these models limits their use to only small sample sizes.

# Chapter 3

# Nearly-Hyperuniform Network Models of Amorphous Silicon

T HIS Chapter and Chapters 4 and 5 are based on M. Hejna, P. J. Steinhardt, S. Torquato, *Nearly hyperuniform network models of amorphous silicon*, Phys. Rev. B **87**, 245204 (2013). In this chapter we introduce the concept of the nearly-hyperuniform network models of amorphous silicon and discuss their implications for the structure of a-Si and the electronic band-gap in a-Si.

## 3.1 Introduction

The development of accurate structural models of amorphous silicon (a-Si) and other tetrahedrally-coordinated solids has been an active area of research for the last eight decades [13, 31, 58], but many challenges remain. The structure of a-Si is approximated well by continuous random network (CRN) models [13, 58], the first of which was introduced by Zachariasen in 1932 [31]. Conventional CRNs for a-Si are fully four-coordinated, isotropic disordered networks that contain primarily five, six, and seven atom rings, while maintaining nearly perfect local tetrahedral order (narrow bond-

angle and bond-length distributions). Predictions derived from CRN models assuming a Keating potential describes the interatomic interactions are in good agreement with many structural properties of a-Si that are accessible via experiments, including the radial distribution function (RDF) and the phonon and electron density of states [58, 70, 76], nearest- and next-nearest-neighbor distances, bond statistics, ring statistics, etc. These successes are related to the form of the structure factor $S(k)$ at intermediate wavenumbers $k$.

In this chapter, we introduce the concept of *nearly hyperuniform network* (NHN) structures and, on the basis of computer simulations, propose that NHN models may provide a better description of a-Si, especially after annealing. A perfectly *hyperuniform solid has a structure factor $S(k)$ that approaches zero as the wavenumber $k \to 0$,* implying that infinite-wavelength density fluctuations vanish [28]. The CRN models based on the Keating model that have been considered in the past (e.g., Ref. [70]) have values of $S(k \to 0)$ comparable to those found in the liquid phase at the equilibrium melting temperature, $S(k \to 0) \approx 0.03$. We define a *nearly hyperuniform network as a disordered tetrahedral structure whose $S(k \to 0)$ is less than the liquid value at melting.* As a practical matter, we shall be interested in cases where $S(k \to 0)$ is substantially less, by 50% or more, which implies a substantial reduction in the large-scale density fluctuations and runs counter to the limitations imposed by the frozen-liquid paradigm.

Employing a novel simulation protocol that is based on the Stillinger-Weber (SW) potential to model the interatomic interactions, we generate a spectrum of NHN models and show that the energy landscape includes a sequence of progressively more hyperuniform minima with values $S(k \to 0)$ that are substantially less than the melting value – by a factor of 2 or more. The simulations suggest that this sequence of states can be reached through extensive annealing, and more efficiently when combined with pressure. We further show that the degree of hyperuniformity correlates with other

measurable signatures in $S(k)$ at intermediate and large $k$ and with the width of the electronic band gap. Experimental measurements by Xie et al. [2] that lend support to this picture are discussed in Chapter 6.

While the SW potential has been shown to give a more realistic description of crystalline silicon [75], the energy penalty for dangling bonds is not sufficiently large, and hence quenches from the melt, via molecular dynamics, result in an unrealistic number of coordination defects. These defects are avoided in conventional CRN models by using the less realistic Keating potential that enforces perfect fourfold coordination.

## 3.2  Methods

In our study, we have devised a novel two-step numerical protocol to produce a spectrum of NHN models that combines the advantages of the Keating and SW potentials. Step one is a standard bond-switching annealing procedure using a Keating potential [69] applied to $20,000$ atoms within a cubic box (under periodic boundary conditions) that is augmented with procedural modifications introduced by Barkema and Mousseau (BM) [70, 71]. However, unlike the BM CRN model, we anneal our systems significantly longer (between 2 to 250 times as long as measured by the number of accepted transpositions) to achieve a sequence of inherent structures (local potential-energy minima) that have lower energies than those of the K (BM) model. In the second step of our procedure, we use our end-state inherent-structure configurations obtained via a Keating potential (K1, K2, etc.) as *initial conditions* for atomic-position rearrangement under a modified SW potential [76] at zero pressure via a conjugate gradient method. We use the same parameters of the SW potential that were determined by fitting the phonon spectra of a-Si to neutron scattering data [76]. We label the corresponding inherent structures of this SW potential respec-

tively SW1, SW2, etc. With this two-step procedure, the resulting structures possess a negligible number of dangling bonds. See Chapter 4 for additional simulation details and Chapter 5 for the geometric and topological properties including structural and energy statistics for the resulting network configurations.

The structure factors $S(k)$ of the generated samples were evaluated by the *sampling volume* method. This method is based on the scaling behavior of density fluctuations presented by Torquato and Stillinger [28] and described in detail in Chapter 4. It can be viewed as a Fourier transform of the pair correlation function $g(r)$ with an appropriately chosen convergence factor that reduces artifacts due to the finite size of the model [21].

## 3.3 Results

In Fig. 3.1, we show $S(k \to 0)$ as a function of the inverse of the height $H$ of the first scattering peak in $S(k)$ for K (BM), the Barkema-Mousseau CRN model [21], as well as for K3, K5, SW3, and SW5. Importantly, it can be observed that the K (BM) model is not an endpoint of annealing under the Keating potential, since further annealing produces a sequence K1 through K5 along a trajectory where $S(k \to 0)$ gets smaller and the first peak height in $S(k)$ gets larger. Moreover, the models obtained by then quenching under the SW potential are nearly hyperuniform: they have values of $S(k \to 0)$ that extend to more than 50% lower than their K progenitors and substantially below the value at the melting temperature. They also have substantially higher radial distribution function (RDF) first-peak heights (see discussion of Tables 5.1 and 5.2 in Chapter 5). The most nearly hyperuniform structure obtained in our anneal run, SW5, yields $S(k \to 0) = 0.010 \pm 0.002$, which represents a 70% reduction in the large-scale density fluctuations relative to the K (BM) model [$S(k \to 0) = 0.035 \pm 0.001$] [21] or over three times more hyperuniform, which is a

remarkably large reduction in the large-scale density fluctuations of the system. We note that we stopped with K5 because the annealing runs began to use unreasonable computational time; we believe that more refined hyperuniform amorphous networks are achievable with yet longer annealing times.
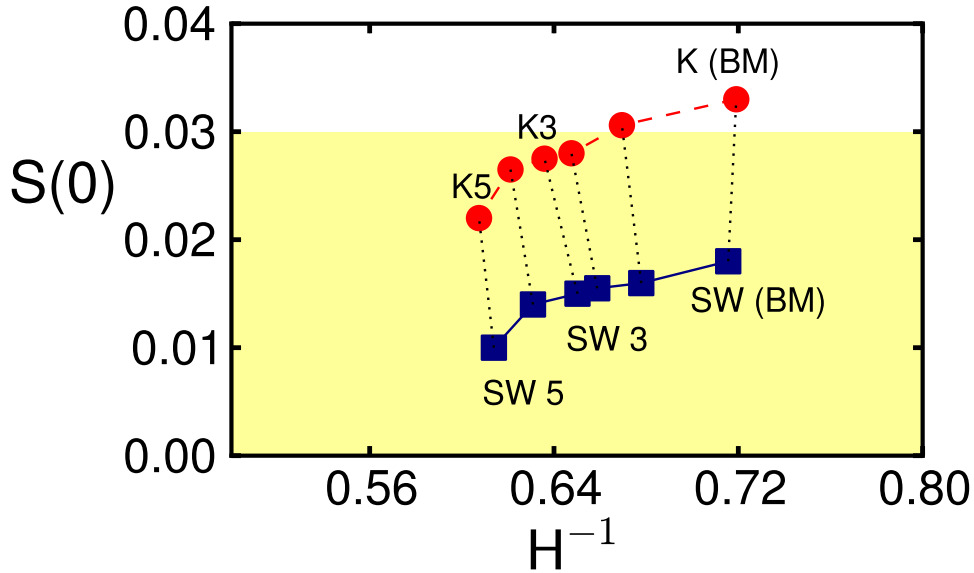


Figure 3.1: $S(k \to 0)$ versus the inverse height $H$ of the first scattering peak for the K (BM) Keating annealed continuous random network model [21] and our Keating annealed models (circles) and the corresponding Stillinger-Weber quenched models (squares). The shaded region indicates the nearly hyperuniform range in which $S(k \to 0)$ is below the equilibrium melting value for a-Si; note that the SW models are substantially below this threshold.

The SW5 model exhibits other signature features that correlate with increased hyperuniformity and can be measured experimentally:

(1) The SW5 structure possesses a bond-angle standard deviation that is more than a degree lower than that of the K (BM) model and is in better agreement with recent bond-angle analysis of monatomic amorphous semiconductors [30].

(2) The height of the first peak of $S(k)$ for the SW5 model is higher than for the K (BM) model, as shown in Fig. 3.2(a). The SW5 model exhibits a small scattering enhancement near $k = 1.0\,\text{Å}^{-1}$ seen in the experiments of Ref. [2].

(3) The K (BM) model has a significantly broader first peak of the pair correlation function $g(r)$ (due to a larger bond-length variation) than the SW5, as shown in Fig. 3.2(b).

(4) For larger wavenumbers, the K (BM) model predicts a significantly faster decay of the large-$k$ oscillations in $S(k)$ than does that of the SW5 model, as shown in Fig. 3.3.

(5) Based on simulations of smaller 1000-atom models and using a tight-binding model for silicon by Kwon [96], the electronic band gap increases with increasing hyperuniformity, as shown in Fig. 3.4. The widths of the isotropic band gaps are calculated as the difference between the lowest energy state of the conduction band and the highest energy state of the valence band. The figure shows that the fractional band gap width $\Delta E/E$ increases as the SW energy per atom decreases, which correlates with increasing relaxation and thus the hyperuniformity. $\Delta E$ is the band gap width and $E$ is the energy of the midpoint of the band gap compared to the lowest energy valence state. The same absolute gap width, $\Delta E$, also increases with hyperuniformity.

To ensure that our NHN configurations are truly amorphous, we analyzed them for the presence of ten-atom cages composed of four adjacent six-rings that constitute a basic building block of the diamond crystalline structure. Our results show that the most annealed CRN sample, K5, has 0.02 ten-atom cages per atom, a tiny fraction compared to the perfect crystal that has one ten-atom cage per atom. Since the Stillinger-Weber relaxation produces only negligible amount of topological defects,
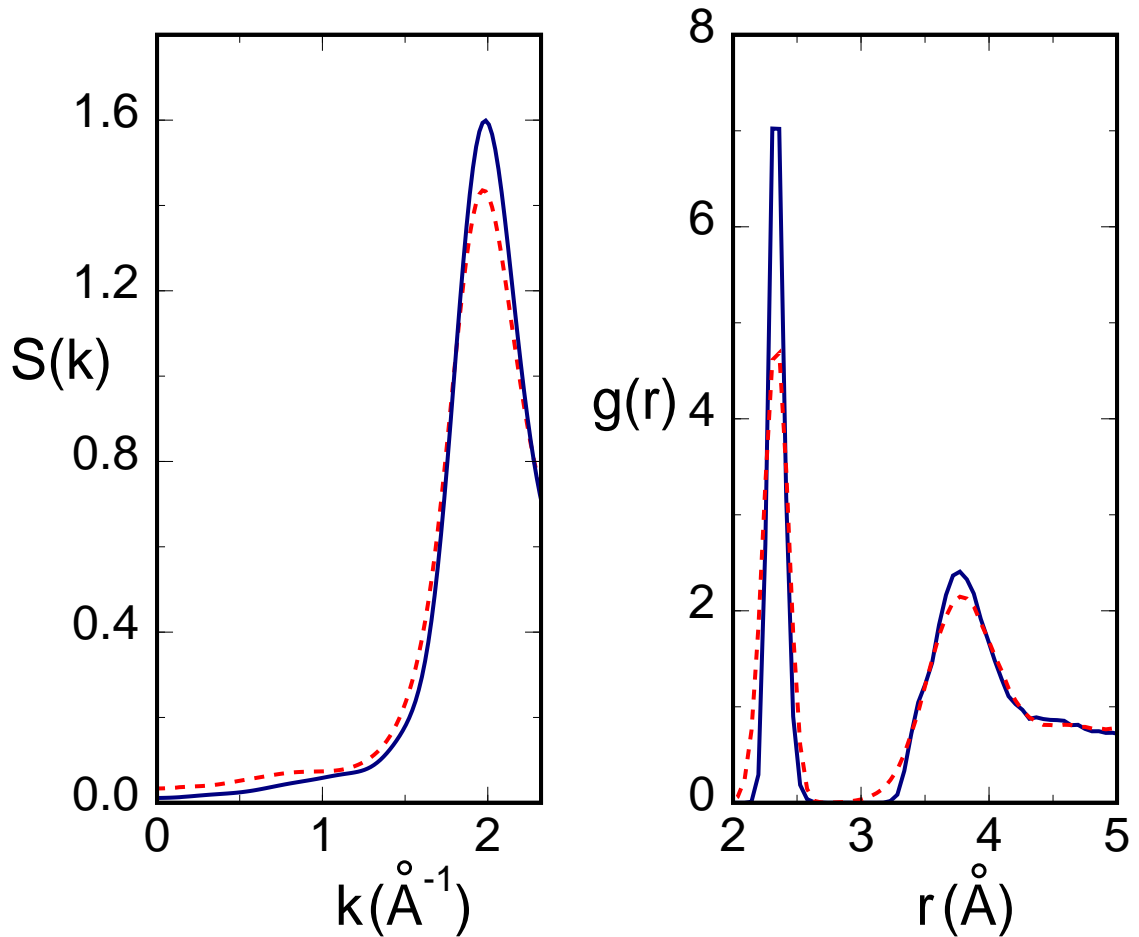
Figure 3.2: (a) Comparison of the angularly averaged structure factor $S(k)$ versus $k$ for small to intermediate $k$ for the Stillinger-Weber quenched SW5 model (blue solid curve) and the Keating annealed K (BM) model [70] (red dashed line). (b) Comparison of the first peak in radial distribution function $g(r)$ versus radial distance $r$ for the K (BM) model [70] (red dashed curve) and the SW5 model (blue solid curve).

the results for K models carry over to the corresponding SW models. The ten-atom cages are quite uniformly distributed throughout the volume, and there are no large clusters. Comparison of our results to a recent study of nucleation [106] shows that NHN models are far from crystallization. The ten-atom diamond cage that constitutes
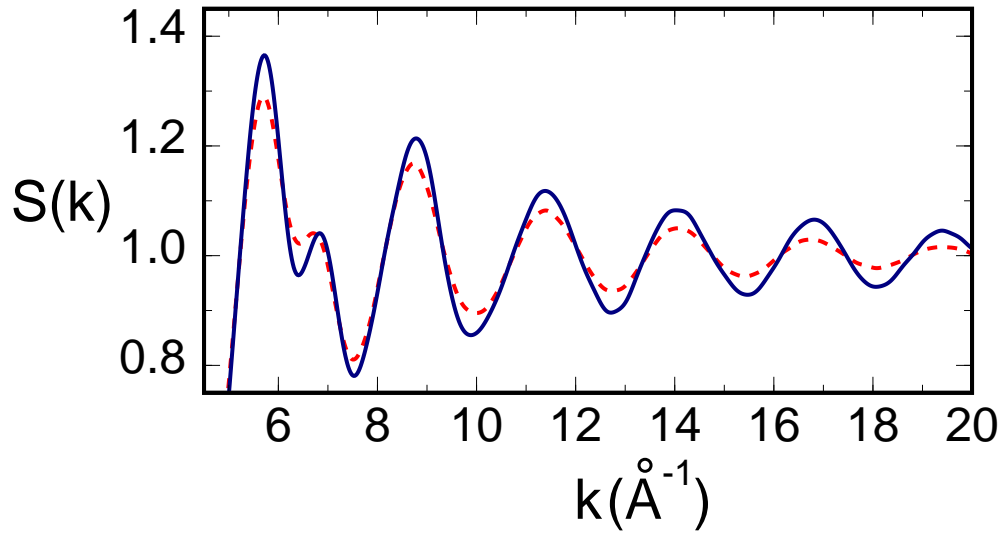
Figure 3.3: The angularly averaged structure factor $S(k)$ versus the wavenumber $k$ at large $k$ for the Stillinger-Weber quenched SW5 model (blue solid curve) displays larger amplitude oscillations than the Keating-annealed K (BM) model [70] (red dashed curve).

a basic building block of the diamond lattice and the eight-atom wurtzite cage that constitutes a basic building block of the wurtzite lattice are shown in Fig. 3.5 (a) and Fig. 3.5 (b) respectively.
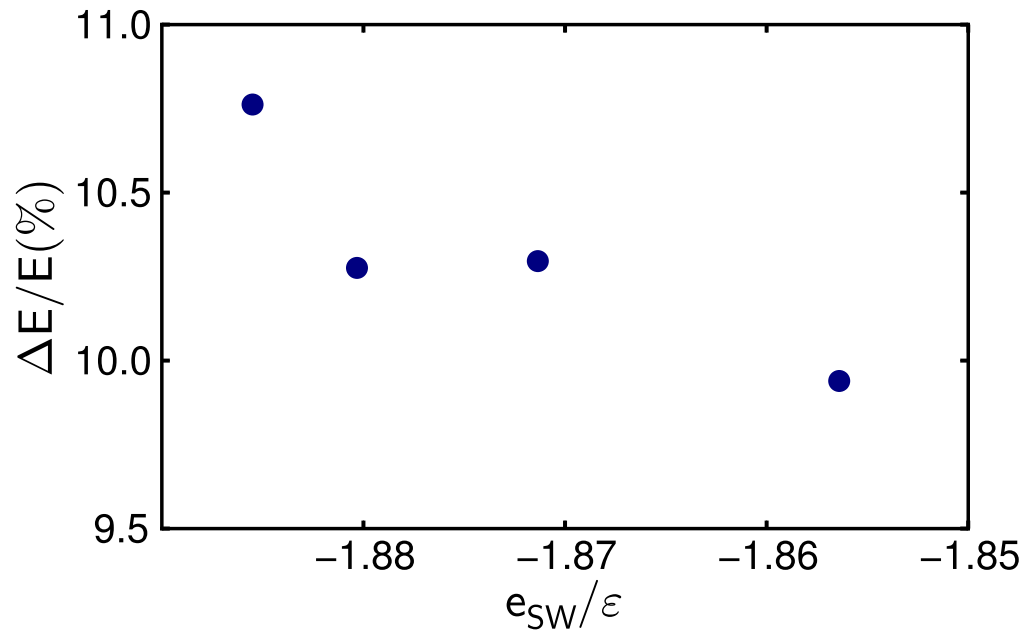
Figure 3.4: Fractional band gap, $\Delta E/E$ versus the average SW energy per atom $e_{SW}$ in units of $\varepsilon = 1.6483\,\text{eV}$, where $\Delta E$ is the band gap width and $E$ the energy at the midpoint of the band gap (measured with respect to the bottom of the valence band). The value of $e_{SW}/\varepsilon$ decreases with increasing hyperuniformity, as shown in Table 5.3 below; hence, the figure shows that fractional band gap width increases with hyperuniformity.
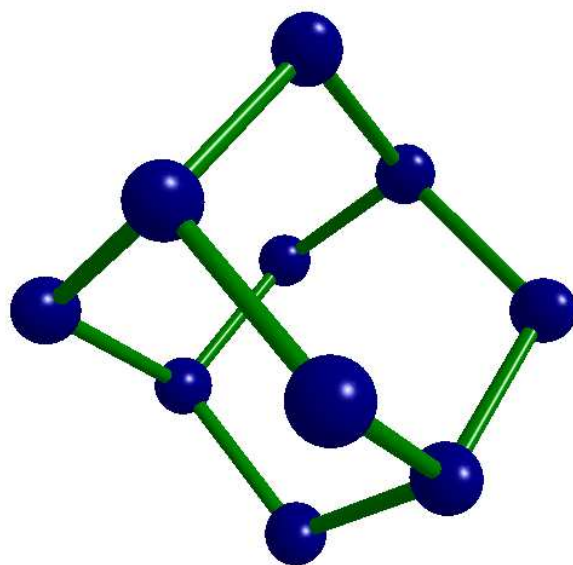
(a) Ten-atom diamond cage
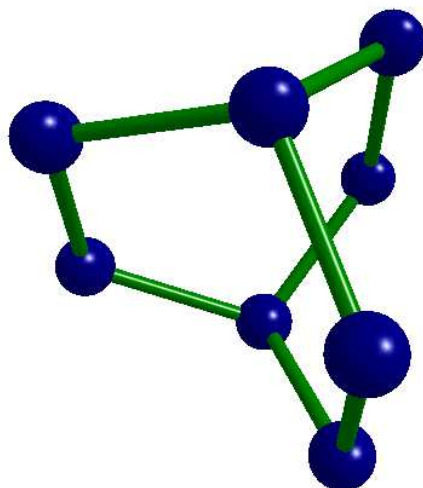


(b) Eight-atom wurtzite cage

Figure 3.5: Illustration of ten-atom diamond cage and eight-atom wurtzite cage that represent a basic building blocks of the diamond and wurtzite lattices respectively. The size of clusters of ten-atom diamond cages can be used as a measure of proximity to crystallization.

## 3.4 Discussion

The fact that our annealing-quenching procedure produces a sequence of NHN models with an increasing degree of hyperuniformity (i.e., $S(k \to 0)$ tending to zero) has deep significance. First, it demonstrates that the energy landscape for conventional Keating-annealed CRN models, for Stillinger-Weber quenched models, and, hence, probably amorphous silicon, has local minima that span a greater diversity of structures than was previously recognized. It also demonstrates that, experimentally, it is possible to reach minima that are more nearly hyperuniform than had been thought achievable. The density fluctuations as measured by $S(k \to 0)$ are not frozen at the freezing point, but continue to decrease with annealing. In particular, the value of $S(k \to 0)$ cannot be considered a universal quantity for a-Si or any other amorphous tetrahedral network, as might be inferred from de Graff and Thorpe [21]. For example, while the percentage drop in the energy per atom in going from the K (BM) model to SW5 is about 23%, the corresponding drop in $S(k \to 0)$ is about 50%. Remarkably, the *configurational proximity metric* [53], which gauges the average local atomic movement required to transform one structure into another, is only about one percent of a bond-length with a corresponding percentage energy drop of only about 2.4% during our Stillinger-Weber (framework) quenching step from a Keating potential-annealed CRN to a SW potential-quenched NHN state, even though the latter possesses an $S(k \to 0)$ that is about one half the CRN value. This reveals the importance of collective atomic rearrangements during the second step of our quenching protocol.

Our findings are completely consistent with recent results for amorphous metals in which the atomic pair interactions are isotropic [107, 108]. In these studies, it has been demonstrated that, on approach to an inherent structure, $S(k \to 0)$ is nearly hyperuniform and decreases monotonically [107], and that $S(k \to 0)$ decreases as the temperature decreases. Also, deeper local minima in the energy landscape are

accessed [108]. Thus, the observation that sampling deeper energy minima are accompanied by increased hyperuniformity appears to apply to a wide class of disordered systems (with both isotropic and directional interactions) and its full elucidation demands attention in the future.

Is it possible to construct a-Si with appreciably smaller $S(k \to 0)$ than reported here or, more ambitiously, reach true hyperuniformity ($S(k \to 0) = 0$)? There are both fundamental and practical reasons to consider such questions. On the practical side, our results above suggest that hyperuniform amorphous tetrahedral network models will have larger electronic band gaps than typical non-hyperuniform samples [13]. Similar ideas have successfully led to the creation of novel designer materials composed of a hyperuniform disordered arrangement of dielectric materials that have complete photonic band gaps [54–56]. On the theoretical side, our present computational results strongly indicate that continued annealing of a-Si samples improves the degree of hyperuniformity. Moreover, our simulations suggest that quenching a-Si samples under increased pressure leads to further decrease of $S(k \to 0)$ (see Table 5.4 for dependence of $S(k \to 0)$ on compression).

Perfect hyperuniformity has been observed previously in disordered systems with hard, short-range isotropic interactions, most notably in a wide class of maximally random jammed packings [36, 37]. It has also been found in systems with soft, long-range interactions; for example, in one component plasmas [42, 44] or in the ground states of so-called *stealthy* potentials [46] that enforce $S(k) = 0$ for a $k$ in a range $[0, k_C]$, where $k_C > 0$. The existence of these diverse examples and our construction here of a sequence of increasingly hyperuniform configurations suggest that the search for a configuration with $S(k \to 0) = 0$ is one of the exciting areas for future research.

Even before our numerical studies of NHN models began, the general theoretical conjectures above stimulated recent measurements by Xie et al. [2] of the structure factor in the long-wavelength limit for a sample of a-Si synthesized by direct ion bom-

bardment. These experiments have measured $S(k \to 0)$ to determine the degree of hyperuniformity both as-implanted and after annealing and have also checked several other correlated signatures predicted above. The results are discussed in Chapter 6.

# Chapter 4

# Description of Methods

I N this chapter, we give details of the techniques used to produce NHN models. We also present a description of techniques used to study the structural and topological properties of the generated models, such as the structure factor and the ring and cage statistics.

## 4.1   Simulation Details to Create NHN Models

We have devised a two-step procedure to create NHN models that are based on the Stillinger-Weber (SW) potential. The first step involves producing a highly annealed CRN model based on the Keating potential as an initial condition for a SW quench. Barkema and Mousseau used an accelerated and scalable modification of the Wooten, Winer, and Weaire (WWW) technique [68] to produce large Keating-relaxed CRN models that have been a standard in the field. We have introduced several improvements to the Barkema-Mousseau algorithm, which, together with faster computers, allow us to generate significantly higher quality CRNs.

The starting point of the WWW technique is a disordered, perfectly four-coordinated network of atoms in a periodic box. Following the suggestion by

Barkema and Mousseau [70], we started from a liquid-like configuration to avoid any memory of an initial crystalline state. This disordered network is evolved through a sequence of bond switches, that are accepted with a Hastings-Metropolis acceptance probability

$$P = \min[1, \exp(-\Delta E_s / k_B T)],$$

where $k_B$ is the Boltzmann constant, $T$ is the temperature, and $\Delta E_s$ is the change of energy due to the bond switch, evaluated from the Keating potential [64]:

$$E_{\text{Keat.}} = \frac{3}{16} \frac{\alpha}{d^2} \sum_{i,j} \left( \mathbf{r}_{ij} \cdot \mathbf{r}_{ij} - d^2 \right)^2 + \frac{3}{16} \frac{\beta}{d^2} \sum_{i,j,k} \left( \mathbf{r}_{ij} \cdot \mathbf{r}_{ik} + \frac{1}{3} d^2 \right)^2.$$

Here $\alpha, \beta$ are the bond-stretching and bond-bending constants respectively, and $d$ is the equilibrium bond length.

Since the acceptance rate is less than 0.1% in a well annealed network, it is important to avoid a complete relaxation of trial configurations and reject the proposed move as soon as it becomes clear that the move will increase the Keating energy. To that end, Barkema and Mousseau have proposed that a move be rejected if the Keating force exceeds a certain threshold value [70]. In addition, we introduce here a *multiscale local cluster relaxation* methodology, which consists of the following steps:

(1) Only atoms in a small cluster of about 120 atoms around a switched bond are relaxed, with the bond-switch being rejected if the energy increases by more than a threshold value of $0.01\,\text{eV}$ per atom in the cluster.

(2) If not rejected in step (1), atoms in a larger cluster of about 320 atoms around the switched bond are relaxed, with the bond-switch being accepted or rejected based on the Hastings-Metropolis acceptance probability.

(3) Relaxation of all the atoms is performed after about a hundred accepted moves to relieve any built up stress due to the local relaxation.

Performing only local relaxations is crucial to the scalability of the algorithm, while using multiple scales increases efficiency. An important speed-up is achieved by parallelization. We use an asynchronous master-worker parallelization paradigm, where the master proposes transpositions and workers report on their success, instead of a bulk synchronous parallelization proposed by Vink et al. [71].

In our procedure, the annealing temperature is slowly decreased from about $0.3\,\mathrm{eV}$ to about $0.15\,\mathrm{eV}$ per silicon atom. Following Barkema and Mousseau, we performed a zero temperature quench every several thousand successful transpositions at the annealing temperature. During the annealing-quenching procedure, we varied the ratio of the two-body and three-body interaction by 5% and the volume of the system by 3%. We found that a significant speed-up of the quenches can be achieved by preferentially trying bond-switches that have the highest strain, then switching the bonds that lie in the neighborhood of previously successful bond-switches, since the successful bond-switches often appear in clusters. Several models K1-K5 at various degree of annealing were produced whenever the Keating energy per atom showed a substantial decrease.

The second step of our two-step procedure to create a NHN model involves finding a zero-pressure inherent structure (local minimum) associated with a modified SW potential interaction. The SW potential [75] involves two- and three- body interactions of the following form:

$$E_{SW} = \sum_{i,j} v_2(r_{ij}) + \sum_{i,j,k} v_3(r_{ij}, r_{ik}, \cos\theta_{ijk}),$$

$$v_2(r_{ij}) = \varepsilon f_2 \left( r_{ij}/\sigma \right),$$

$$v_3(r_{ij}, r_{ik}, \cos\theta_{ijk}) = \varepsilon f_3 \left( r_{ij}/\sigma, r_{ik}/\sigma, \cos\theta_{ijk} \right),$$

where

$$f_2(r) = \begin{cases} A(Br^{-p} - r^{-q}) \exp\left[ (r-a)^{-1} \right] & r < a \\ 0 & r \geq a, \end{cases}$$

$$f_3(r_{ij}, r_{ik}, \cos\theta_{ijk}) =$$

$$\lambda \exp\left[ \gamma(r_{ij} - a)^{-1} + \gamma(r_{ik} - a)^{-1} \right] \left( \cos\theta_{ijk} + \frac{1}{3} \right)^2.$$

Here $\varepsilon = 1.6483\,\text{eV}$, $A = 7.050$, $B = 0.6022$, $p = 4$, $q = 0$, $a = 1.80$, $\lambda = 31.5$, $\gamma = 1.20$, and $\sigma = 2.0951\,\text{Å}$ are parameters that were determined from fitting the location of transverse optic and transverse acoustic peaks to neutron scattering experiments on a-Si by Vink et al. [76].

The advantage of the two-step procedure lies in its computational efficiency, which is crucial for a generation of large samples needed for a study of hyperuniformity. The first step uses a simple quadratic potential (Keating potential) to obtain a defectless network structure that serves as a crude approximation of a-Si. The second step uses a more accurate potential (Stillinger-Weber potential) to obtain an inherent structure of a realistic potential without the need of performing the entire relaxation with a computationally expensive potential.

## 4.2   Stillinger-Weber Quench

The Stillinger-Weber quench described in the previous section was performed at zero external pressure under a modified Stillinger-Weber potential. The numerical relax-

ation of the point pattern was performed using the Polak-Ribiere conjugate gradient method at zero pressure, until a local minimum was reached. In order to efficiently relax a large point pattern with three-body interactions, we used a periodically wrapped cell list method. In this method the simulation domain is subdivided into appropriately sized small cells that wrap around to accommodate the periodic boundary conditions. Points are binned into cells and only points within a block of $3 \times 3 \times 3$ neighboring cells are considered for evaluation, reflecting the short-range interaction of the Stillinger-Weber potential. The cell list method allows to evaluate the force with computational complexity of $\mathcal{O}(N)$ steps for an $N$-particle system. This numerical computation was performed on a cluster of four Nvidia Tesla graphics card units, totaling 960 CUDA cores.

Currently there are no reliable measurements of the three-point correlation function $g_3(r_{12}, r_{13}, r_{23})$ (where $r_{12}, r_{13}, r_{23}$ are the side lengths of the triangle defined by points $\mathbf{r}_1, \mathbf{r}_2, \mathbf{r}_3$) that could help discriminate between different empirical potentials used to relax models of a-Si. Since it is expected that $g_3(r_{12}, r_{13}, r_{23})$ is sensitive to the form of the three-body term of the empirical potential used for relaxation, a precise measurement of $g_3(r_{12}, r_{13}, r_{23})$ could reveal a need to either modify the parameters of the Stillinger-Weber potential or to replace the Stillinger-Weber potential by a computationally more costly potential (e.g. Tersoff or EDIP potential) in the second step of the two-step procedure.

## 4.3 Evaluating the Structure Factor from a Numerical Model

The structure factors $S(k)$ of the generated samples were evaluated by the *sampling volume* method. This method is based on the scaling behavior of density fluctuations presented by Torquato and Stillinger [28] and described in detail by de Graff and

Thorpe [21]. The method can be viewed as a Fourier transform of the pair correlation function $g(r)$ with an appropriately chosen convergence factor that reduces artifacts due to the finite size of the model [21]. In the rest of this section we will derive the formula for the estimate of the structure factor using the sampling volume method and show how it is related to the Fourier transform of the pair correlation function.

Consider a sphere of radius $R$ centered at $\mathbf{x}_0$ within an $N$-point sample with periodic boundary conditions. The structure factor of points that lie within this sphere is given by

$$S_w(\mathbf{k}, R) = \frac{1}{N} \sum_{i,j}^{N} w_R\left(\mathbf{r}_i - \mathbf{x}_0\right) w_R\left(\mathbf{r}_j - \mathbf{x}_0\right) e^{i\mathbf{k}\cdot(\mathbf{r}_i - \mathbf{r}_j)}, \tag{4.1}$$

where $w_R(\mathbf{r})$ is the spherical window function defined as

$$w_R(\mathbf{r}) = \begin{cases} 1 & |\mathbf{r}| \leq R \\ 0 & |\mathbf{r}| > R. \end{cases} \tag{4.2}$$

We will assume that the sample is part of a homogeneous system, so that we can average over all possible positions of $\mathbf{x}_0$ (center of the spherical window). Translational averaging gives the following value of the structure factor:

$$S_w(\mathbf{k}, R) = \frac{1}{VN} \int_V \sum_{i,j} w_R\left(\mathbf{r}_i - \mathbf{x}_0\right) w_R\left(\mathbf{r}_j - \mathbf{x}_0\right) e^{i\mathbf{k}\cdot(\mathbf{r}_i - \mathbf{r}_j)} d\mathbf{x}_0, \tag{4.3}$$

which can be expressed as

$$S_w(\mathbf{k}, R) = \frac{1}{N} \sum_{i,j} \alpha_R(\mathbf{r}_i - \mathbf{r}_j) e^{i\mathbf{k}\cdot(\mathbf{r}_i - \mathbf{r}_j)}, \tag{4.4}$$

where we have introduced a spherical intersection function $\alpha(\mathbf{r})$, which is given by the following formula (in three dimensions).

$$\alpha_R(\mathbf{r}) = \begin{cases} 1 - \frac{3}{4}\frac{r}{R} + \frac{1}{16}\left(\frac{r}{R}\right)^3 = \left(1 - \frac{r}{2R}\right)^2\left(1 + \frac{r}{4R}\right) & r \leq 2R, \\ 0 & r > 2R, \end{cases} \tag{4.5}$$

where $r = |\mathbf{r}|$.

We will further assume that the sample is part of an isotropic system and thus the structure factor depends only on the magnitude of the wavevector $k = |\mathbf{k}|$. This allows us to average over all possible spherical angles $\Omega$ of directions of the wavevector $\mathbf{k}$.

$$S_w(k, R) = \frac{1}{4\pi}\int_{S^2}\frac{1}{N}\sum_{i,j}\alpha_R(\mathbf{r}_i - \mathbf{r}_j)e^{i\mathbf{k}\cdot(\mathbf{r}_i - \mathbf{r}_j)}d\Omega, \tag{4.6}$$

which simplifies to

$$S_w(k, R) = \frac{1}{N}\sum_{i,j}\alpha_R(|\mathbf{r}_i - \mathbf{r}_j|)\frac{\sin(k|\mathbf{r}_i - \mathbf{r}_j|)}{k|\mathbf{r}_i - \mathbf{r}_j|}. \tag{4.7}$$

The structure factor $S_w(k, R)$ of a sample has a sharp central peak $S_{cp}(k)$ at $\mathbf{k} = 0$ that approaches a delta function peak $(S_{cp}(k) = \delta(k))$ in the infinite sample limit. In order to estimate the behavior of the central peak, we will evaluate the scattering amplitude of the spherical sampling window that is uniformly filled with density $\rho_0$. Such a spherical sampling window has a central peak of amplitude

$$A_{cp}(k, R, \mathbf{x}_0) = \rho_0\int_{\mathbb{R}^3}w_R(\mathbf{r} - \mathbf{x}_0)e^{i\mathbf{k}\cdot\mathbf{r}}d\mathbf{r} = \rho_0\tilde{w}_R(k)e^{i\mathbf{k}\cdot\mathbf{x}_0}, \tag{4.8}$$

where $\tilde{w}_R(k) = \left(\frac{2\pi}{kR}\right)^{3/2}R^3J_{3/2}(kR)$. Here $J_{3/2}(kR) = \sqrt{\frac{\pi}{2(kR)^5}}[\sin(kR) - (kR)\cos(kR)]$ is the Bessel function of order $3/2$. The corresponding structure factor is given by

$$S_{cp}(k, R) = \frac{|A_{cp}(k, R, \mathbf{x}_0)|^2}{\langle N(R)\rangle} = \rho_0^2\frac{|\tilde{w}_R(k)|^2}{\rho_0 v(R)} = \rho_0\tilde{\alpha}_R(k), \tag{4.9}$$

63

where $v(R) = \frac{4\pi}{3}R^3$ is the volume of the spherical sampling window, $\langle N(R) \rangle = \rho_0 v(R)$ is the average number of atoms within the spherical sampling window, and $\tilde{\alpha}_R(k) = \frac{12\pi}{k^6 R^3}\left[\sin(kR) - (kR)\cos(kR)\right]^2$. Thus we obtain the structure factor with the central peak subtracted $S(k, R)$ as

$$S(k, R) = -\rho_0 \tilde{\alpha}_R(k) + \frac{1}{N}\sum_{i,j}\alpha_R(|\mathbf{r}_i - \mathbf{r}_j|)\frac{\sin\left(k|\mathbf{r}_i - \mathbf{r}_j|\right)}{k|\mathbf{r}_i - \mathbf{r}_j|}, \qquad (4.10)$$

or, performing the sum over $i = j$,

$$S(k, R) = -\rho_0 \tilde{\alpha}_R(k) + 1 + \frac{1}{N}\sum_{i \neq j}\alpha_R(|\mathbf{r}_i - \mathbf{r}_j|)\frac{\sin\left(k|\mathbf{r}_i - \mathbf{r}_j|\right)}{k|\mathbf{r}_i - \mathbf{r}_j|}, \qquad (4.11)$$

where $\rho_0$ is the density of the infinite sample.

From equations (4.5) and (4.11) we expect that for a fixed value of $k$, the large $R$ behavior of $S(k, R)$ is $S(k, R) = a + b/R + O(1/R^3)$. Therefore, to obtain the value of $S(k)$, we plot $S(k, R)$ versus $1/R$, and extrapolate the linear relation between $S(k, R)$ and $1/R$ to $1/R \to 0$. Fig. 4.1 shows the dependence of the relative variance on $1/R$. The relation between $S(k, R)$ and $1/R$ is to a good degree linear. We extrapolate this linear dependence to obtain $S(k)$ by the linear least square fit. The Error of the extrapolation can be estimated from the linear least square fit variation.

The first part of the formula (4.11) can be expressed as

$$-\rho_0 \tilde{\alpha}_R(k) = -\rho_0 \int_{\mathbb{R}^3} \alpha_R(|\mathbf{r}|)e^{-i\mathbf{k}\cdot\mathbf{r}}d\mathbf{r} = -\int_0^\infty \rho_0 4\pi r^2 \frac{\sin(kr)}{kr}\alpha_R(r)dr. \qquad (4.12)$$

The last part of the formula (4.11) can be recognized as a discrete approximation to to the continuous integral, i.e.

$$\int_0^\infty \rho_0 4\pi r^2 g(r)\frac{\sin(kr)}{kr}\alpha_R(r)dr \approx \frac{1}{N}\sum_{i \neq j}\alpha_R(|\mathbf{r}_i - \mathbf{r}_j|)\frac{\sin\left(k|\mathbf{r}_i - \mathbf{r}_j|\right)}{k|\mathbf{r}_i - \mathbf{r}_j|}. \qquad (4.13)$$

64
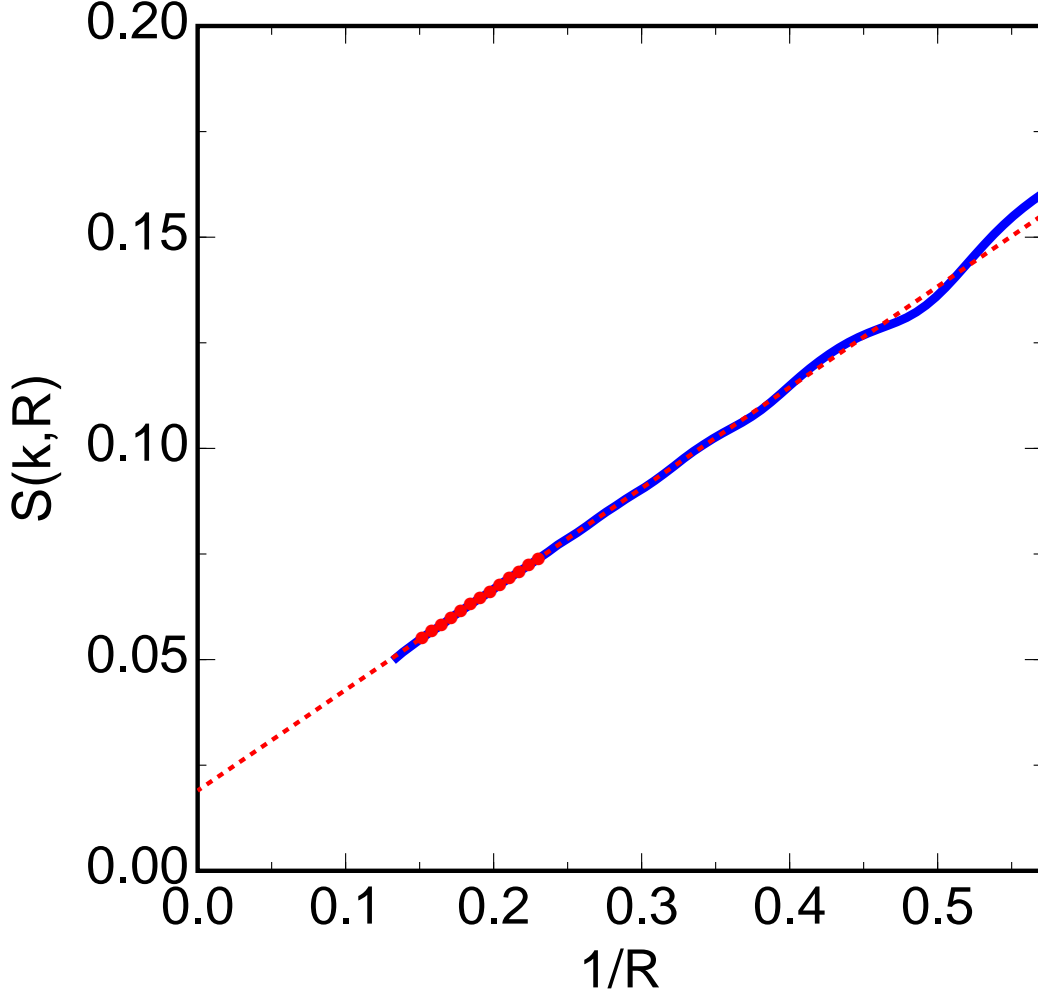
Figure 4.1: Plot of the relative variance of the sample versus $1/R$. The relative variance exhibits a linear dependence on $1/R$. Red dashed line shows how the relative variance can be extrapolated to $1/R \to 0$ to obtain the value of $S(k)$.

Given the approximation

$$\int_0^\infty \rho_0 4\pi r^2 g(r) \frac{\sin(kr)}{kr} \alpha_R(r) dr \approx \frac{1}{N} \sum_{i \neq j} \alpha_R(|\mathbf{r}_i - \mathbf{r}_j|) \frac{\sin(k|\mathbf{r}_i - \mathbf{r}_j|)}{k|\mathbf{r}_i - \mathbf{r}_j|}, \qquad (4.14)$$

equation (4.10) can be recognized as a discrete approximation of

$$S(k) = 1 + \int_0^\infty 4\pi r^2 \left[\rho(r) - \rho_0\right] \frac{\sin kr}{kr} \alpha_R(r) dr. \tag{4.15}$$

Hence the sampling volume method can be thought of as being derived from the formula

$$S(k) = 1 + 4\pi \int_0^\infty r \left[\rho(r) - \rho_0\right] \frac{\sin(kr)}{k} dr, \tag{4.16}$$

where the regularization factor $\alpha_R(r)$ was used in the infinite integral to turn it into a finite one, and in order to obtain the best estimate of the regularized integral and a discrete sum was used. Compare to equation (1.11) in section 1.7 and note that $\rho(r) - \rho_0 = \rho_0(g(r) - 1)$.

## 4.4   Ring Statistics

The ring statistics provides an important measure of the medium-range order in the continuous random network models. In addition to characterizing the ring statistics itself, the ring adjacency can be used to identify larger topological structures, such as eight-atom wurtzite cages and ten-atom diamond cages. Many different irreducibility criteria have been proposed in the past to determine what constitutes an irreducible ring. While different irreducibility criteria generally agree for small rings, they may differ for larger rings (more than about 7 atoms). In this thesis, the ring statistics used are the irreducible shortest-path ring statistics [32]. Unlike many other irreducibility criteria, the shortest-path rings agree well with the intuitive notion of an irreducible ring.

In order to explain the shortest-path irreducibility criterion we give a few definitions. A *path* of length $k$ is a sequence of $k$ adjacent bonds, which are defined as as bonds that share an atom. A *ring* of length $k$ is a sequence of $k$ adjacent bonds

with at most one bond per vertex pair that starts and ends at the same atom. The *topological distance* between atoms $i, j$ is the minimum $k$ such that there is a path between $i$ and $j$ of length $k$. The *irreducible shortest-path ring* is defined as a ring that contains a shortest path for each pair of vertices in the ring. The irreducible shortest-path rings can be efficiently enumerated by the backtracking algorithm [32].

There are no experiments that measure the ring statistics directly, nevertheless some experiments put constraints on the possible topologies of a-Si. Since triangles result in highly strained atomic configurations, which lead to electronic states in the band gap counter to experiments, a realistic model of a-Si should not contain triangles. Presence of a significant number of triangles is also inconsistent with the narrow bond angle distribution inferred from the pair correlation function $g(r)$. Increased dihedral ordering deduced from a careful analysis of the pair correlation function [30] points towards a large number of six-rings.

# Chapter 5

# Structural Characteristics of NHN Models

I N this chapter we present structural characteristics of the NHN models. These characteristics demonstrate the homogeneity and isotropy of the generated samples. They also show the level of relaxation and put the models in the context of other samples generated in the past. In the last two sections, we discuss the density of electronic and vibrational states.

## 5.1 Geometric Characterization of Amorphous Silicon

Geometric characteristics refer to the properties that can be expressed in terms of geometric distances. These include the distributions of bond lengths, distributions of bond angles and quantities based on the pair correlation function and the structure factor. Characteristics that are derived from the total energy of the sample under the interaction of some potential are also considered geometric characteristics.

Table 5.1 summarizes the structural properties of the Keating-relaxed CRN models with progressively higher level of annealing. K5, the most annealed model, has more than a degree lower bond angle deviation than Barkema-Mousseau models [70] (K (BM)). The Short-range order of the models improves with annealing. Table 5.1 shows the standard deviation $\sigma_L$ of the bond length, the standard deviation $\sigma_A$ of the bond angle, the limit of the structure factor as $k \to 0$ and the height of the first-coordination shell peak in $g(r)$.

| Model | $\sigma_L$ | $\sigma_A$ | $S(k \to 0)$ | $g(r)$ max |
|---|---|---|---|---|
| K (BM) | 4.03% | 9.94° | 0.035 | 4.9 |
| K1 | 3.84% | 9.23° | 0.031 | 5.1 |
| K2 | 3.83% | 9.14° | 0.028 | 5.1 |
| K3 | 3.80% | 9.01° | 0.027 | 5.2 |
| K4 | 3.71% | 8.71° | 0.026 | 5.3 |
| K5 | 3.64% | 8.61° | 0.022 | 5.4 |

Table 5.1: Short-ranged and long-ranged properties of the Keating-relaxed CRN models

Table 5.2 summarizes the structural properties of the NHN models derived from the CRN models by a zero-pressure minimization of the modified Stillinger-Weber potential. The SW (BM) model is obtained from the Barkema-Mousseau CRN model [70] (K (BM)). Table 5.2 shows the standard deviation of the bond length, the standard deviation of the bond angle, the limit of the structure factor as $k \to 0$, and the height of the first-coordination shell peak in $g(r)$.

| Model | $\sigma_L$ | $\sigma_A$ | $S(k \to 0)$ | $g(r)$ max |
|---|---|---|---|---|
| SW (BM) | 2.70% | 10.5° | 0.018 | 7.3 |
| SW1 | 2.68% | 10.0° | 0.016 | 7.3 |
| SW2 | 2.68% | 9.8° | 0.015 | 7.3 |
| SW3 | 2.66% | 9.6° | 0.015 | 7.4 |
| SW4 | 2.66% | 9.3° | 0.014 | 7.4 |
| SW5 | 2.65% | 9.2° | 0.010 | 7.4 |

Table 5.2: Short-ranged and long-ranged properties of the NHN models

Table 5.3 shows the average motion of atoms (measured by the configurational proximity metric $p_{i \to f} = \sqrt{\sum_{k=1}^{N} |\mathbf{r}_{i,k} - \mathbf{r}_{f,k}|^2}/r_0$, where $r_{i,k}$, $r_{f,k}$ are the initial and final positions of atoms in the SW quench and $r_0$ is the mean nearest-neighbor distance [53]) as a result of replacing the Keating interaction with the Stillinger-Weber interaction. This quantifies the configurational distance of the SW models from their K progenitors. The Keating energy ($e_K$) and Stillinger-Weber energy per atom ($e_{SW}$) of a CRN model and the Stillinger-Weber energy per atom ($e_{SW}$) of the corresponding SW model are also shown. The SW (BM) model is obtained from the Barkema-Mousseau CRN model [70] (K (BM)).

| Model | Prox. metric | $e_K$ (K) | $e_{SW}/\varepsilon$ (K) | $e_{SW}/\varepsilon$ (SW) |
|---|---|---|---|---|
| SW (BM) | 0.723% | 0.02130 | $-1.7809$ | $-1.8264$ |
| SW1 | 0.900% | 0.01864 | $-1.8141$ | $-1.8505$ |
| SW2 | 1.062% | 0.01833 | $-1.8179$ | $-1.8532$ |
| SW3 | 0.952% | 0.01794 | $-1.8235$ | $-1.8553$ |
| SW4 | 1.088% | 0.01685 | $-1.8372$ | $-1.8645$ |
| SW5 | 1.015% | 0.01648 | $-1.8421$ | $-1.8660$ |
| Diamond | | 0 | $-2.0000$ | $-2.0000$ |

Table 5.3: Energies per atom of the K and SW models under different interactions. $e_{SW}$ is given in units of the SW potential energy scale $\varepsilon = 1.6483\,\mathrm{eV}$. $e_K$ is given in dimensionless units in which $d = \sqrt{3}/2$ and $\alpha = d^2$. Energies of the diamond lattice are shown for comparison. The first column shows the distance of a SW model from its K progenitor in terms of the proximity metric.

Table 5.4 shows the values of $S(k \to 0)$ for a sequence of models that were obtained by a constant-volume SW quench of CRN5 at various degrees of compression. The compression is expressed in terms of the relative compression of the linear scale compared to the linear scale of the sample at zero pressure (SW5). The uncertainty of $S(k \to 0)$ is 0.002.

| Rel. Compr. | $-4\%$ | $0\%$ | $4\%$ | $8\%$ |
|---|---|---|---|---|
| $P(\mathrm{GPa})$ | $-10$ | $0$ | $10$ | $30$ |
| $S(k \to 0)$ | 0.017 | 0.010 | 0.009 | 0.007 |

Table 5.4: Dependence of $S(k \to 0)$ on the relative compression of the linear scale during a constant-volume SW quench

## 5.2 Topological Characterization of Amorphous Silicon

A characteristic of a sample is considered topological if it is derived from the model's connectivity table defined by the atomic bonding. Topological characteristics include concentrations of rings of different orders, concentrations of various cages, clusters of cages and characteristics derived from these notions.

Table 5.5 compares the irreducible ring statistics of the Barkema-Mousseau CRN model [70] (K (BM)) and our most annealed model (K5). The medium-range order significantly improves with annealing, as seen by the increased number of hexagons and smaller number of squares as well as eight- and nine-membered rings.

| Ring order | 4 | 5 | 6 | 7 | 8 | 9 |
|---|---|---|---|---|---|---|
| K (BM) | 2.39% | 45.5% | 74.1% | 51.0% | 15.7% | 4.1% |
| K1 | 1.61% | 43.2% | 80.5% | 52.6% | 13.9% | 3.1% |
| K2 | 1.47% | 43.1% | 81.2% | 52.8% | 13.9% | 3.1% |
| K3 | 1.37% | 42.5% | 82.8% | 53.0% | 14.0% | 2.9% |
| K4 | 1.00% | 42.1% | 83.9% | 54.6% | 13.1% | 2.6% |
| K5 | 0.99% | 42.8% | 85.0% | 53.9% | 12.9% | 2.6% |

Table 5.5: Comparison of the ring statistics between the Barkema-Mousseau CRN model [70] (K (BM)) and our most annealed model (K5)

Tables 5.6 and 5.6 show characteristics of the ten-atom cages of our models. The results for crystalline and paracrystalline [109] models are shown for reference. In Table 5.6, the first column shows the number of the ten-atom diamond cages per atom; the second column shows the number of clusters of diamond cages per atom. In Table 5.7, the first column shows the size of the maximal cluster; the second column shows the average size of the clusters; and the third column shows the number of

interior cages. *Interior cages* are defined as cages whose atoms and neighbors all lie within the same cluster. Clusters are collections of ten-atom cages in which each ten-atom cage shares one atom or more with at least one other ten-atom cage.

Cage statistics of the K1-5 and SW1-5 models shows that while our models are significantly more relaxed than the K (BM) model, the models are very far from crystallinity or paracrystallinity. Table 5.6 shows that the number of clusters per atom in the K/SW models increases with annealing, and hence that increased annealing moves the K/SW models away from the Paracrystalline model. As this trend is the exact opposite from what is expected based on the behavior of the concentration of the ten-atom cages in the K/SW samples, it raises a serious doubt on whether paracrystalline state can be reached by annealing of a-Si.

| Model | No. cages | No. cl. per atom |
|:---:|:---:|:---:|
| K/SW (BM) | 0.9% | $6.29 \times 10^{-3}$ |
| K1/SW1 | 1.6% | $8.30 \times 10^{-3}$ |
| K2/SW2 | 1.6% | $8.20 \times 10^{-3}$ |
| K3/SW3 | 1.6% | $8.10 \times 10^{-3}$ |
| K4/SW4 | 1.9% | $9.15 \times 10^{-3}$ |
| K5/SW5 | 2.2% | $9.95 \times 10^{-3}$ |
| Paracryst. | 15.5% | $4.05 \times 10^{-3}$ |
| Diamond cryst. | 100% | $1/N$ |

Table 5.6: The table shows the number of ten-atom cages per atom (No. cages); the number of clusters (cl.) per atom. The K1-5 and SW1-5 models all contain $20,000$ atoms; the crystalline has $N$ atoms and the paracrystalline model has 1728 atoms.

| Model | Max cl. sz. | Aver. cl. sz. | No. int. cages |
|---|---|---|---|
| K/SW (BM) | 40 | 12.6 | 0 |
| K1/SW1 | 77 | 14.4 | 0 |
| K2/SW2 | 87 | 14.6 | 2 |
| K3/SW3 | 88 | 14.9 | 0 |
| K4/SW4 | 48 | 15.5 | 0 |
| K5/SW5 | 90 | 15.7 | 0 |
| Paracryst. | 746 | 122.7 | 67 |
| Diamond cryst. | $N$ | $N$ | $N$ |

Table 5.7: The table shows the number of atoms in the largest cluster; the average cluster size; and the number of interior cages. The K1-5 and SW1-5 models all contain $20,000$ atoms; the crystalline has $N$ atoms and the paracrystalline model has 1728 atoms.

Fig. 5.1 shows that the ten-atom cage clusters are distributed uniformly throughout the volume of the SW5 sample. The figure also shows that there are no large crystalline clusters present in the sample. In fact the largest crystalline cluster has 90 atoms as can be seen from Table 5.7, compared to 746 for the paracrystalline model.
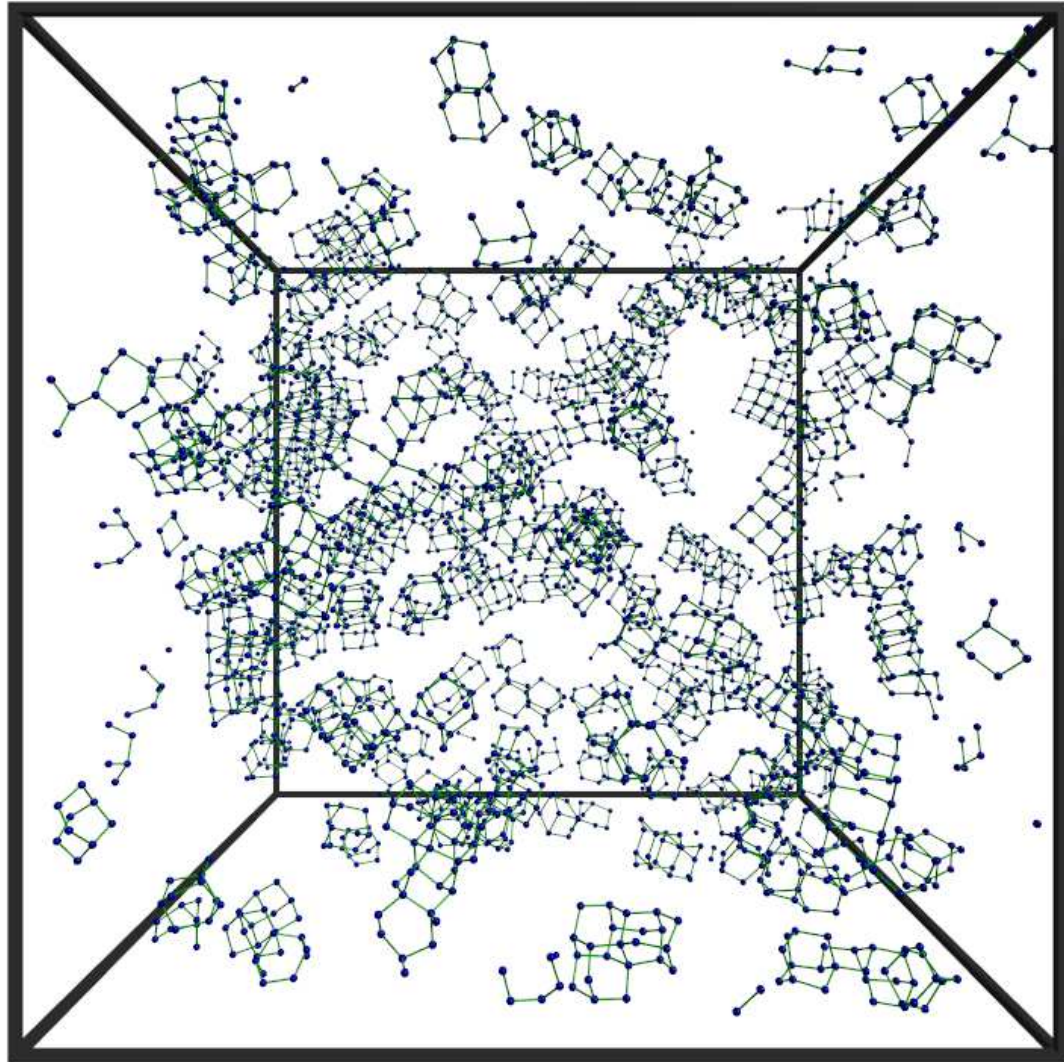
Figure 5.1: Distribution of the ten-atom cages in the SW5 model; see Fig 3.5 (a) in Chapter 3 for an illustration of a single ten-atom cage. Ten-atom cages in the SW5 sample are distributed uniformly throughout the volume.

## 5.3 Isotropy of NHN Models

In order to check that the NHN models are isotropic, we compute the values of the structure factor $S(\mathbf{k})$ for a two-dimensional cut through the functional values of $S(\mathbf{k})$ in the three-dimensional space of the wavevectors $\mathbf{k}$. Fig. 5.2 shows the values of the

structure factor $S(\mathbf{k})$ as a heatmap. Blue on the color scale corresponds to $S(\mathbf{k}) = 0$, and red color corresponds to $S(\mathbf{k}) = 2.5$. The figure demonstrates that the SW5 model is isotropic. The cross-like feature at $\mathbf{k} = \mathbf{0}$ is a finite size artifact of the cubic box that bounds the sample.
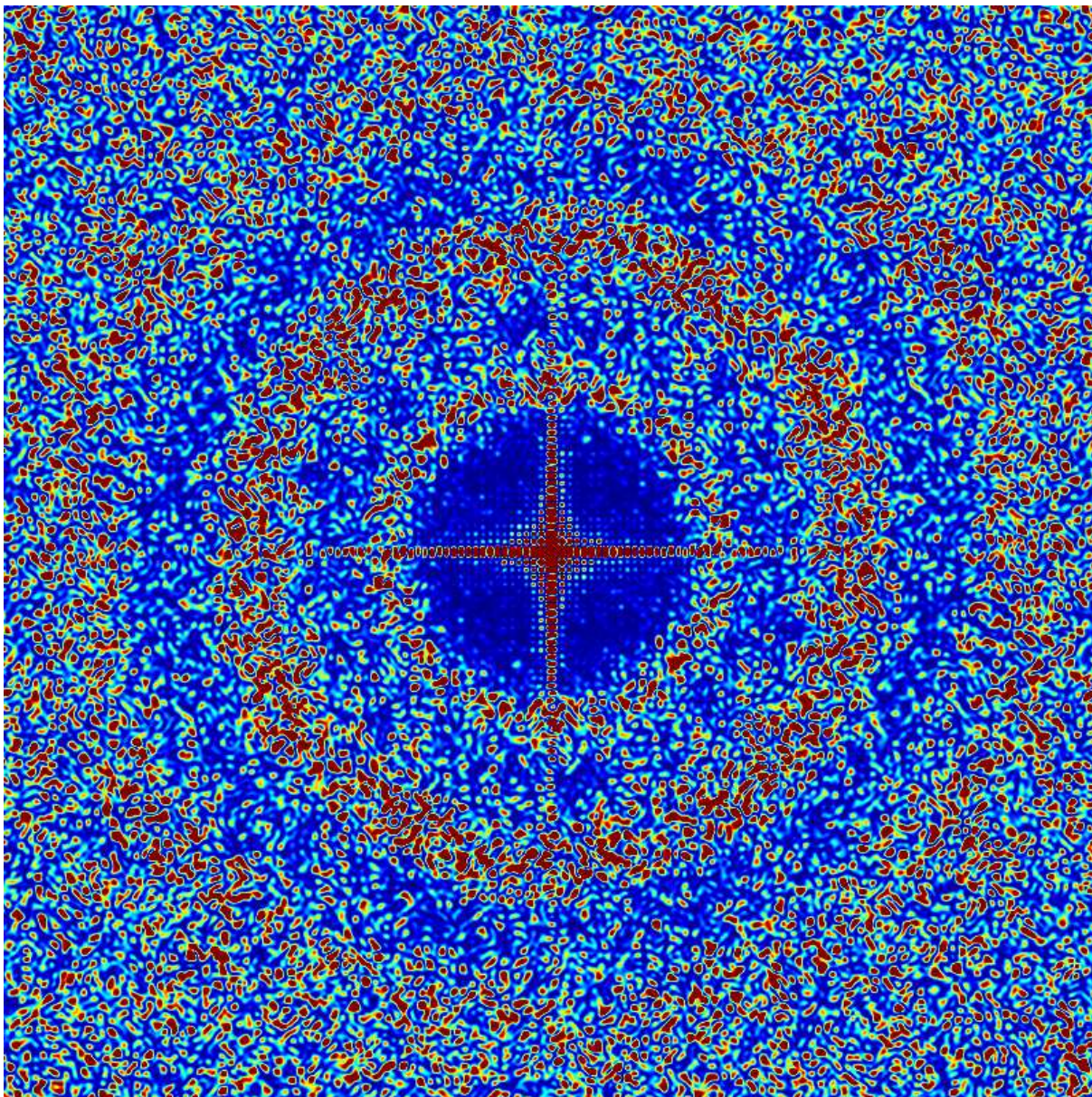


Figure 5.2: two-dimensional cut through the three-dimensional $\mathbf{k}$ space with the values of the structure factor $S(\mathbf{k})$ shown as a heatmap plot. The region shown corresponds to $\mathbf{k} = (k_x, k_y, 0)$ with $k_x, k_y \in [-6.5\,\text{Å}^{-1}, 6.5\,\text{Å}^{-1}]$. The cross-like feature at $\mathbf{k} = \mathbf{0}$ is an finite size artifact of the cubic box that bounds the sample.

## 5.4 Band gap in Amorphous Silicon

The atom of silicon has 14 electrons. Ten of these electrons are core electrons (in $1s^2 2s^2 2p^6$ configuration), tightly bound to the Si nucleus and consequently do not take part in the chemical bonding. The outermost four electrons (valence electrons) of silicon atom have atomic configuration $3s^2 3p^2$, which changes to a hybridized $sp^3$ configuration in materials with tetrahedral bonding order. The proximity of nearby silicon atoms leads to a creation of bonding and anti-bonding molecular orbitals as shown in Fig. 5.3. Since electrons can make a transition between different bonding sites, bonding orbitals are broadened into a valence band and anti-bonding orbitals are broadened into a conduction band, as is schematically shown in Fig. 5.3.
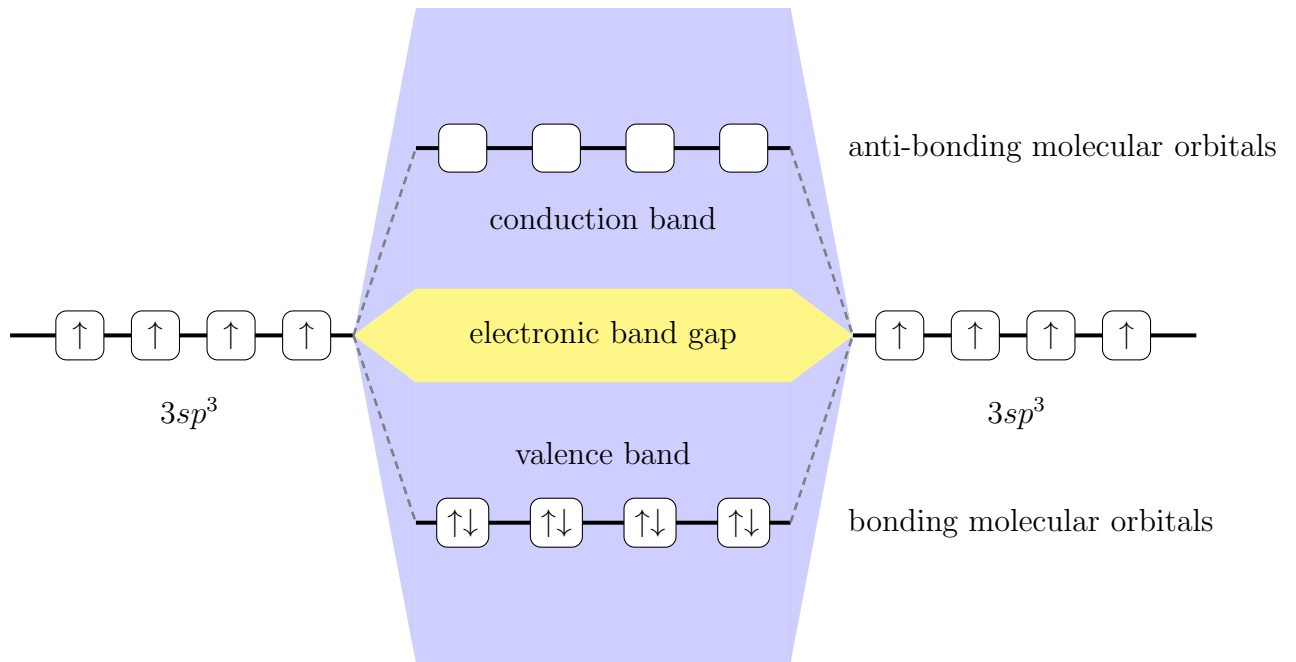
Figure 5.3: Electronic band gap in amorphous silicon. Hybridized $sp^3$ orbitals form bonding and anti-bonding molecular orbitals, that are broadened to valence and conduction bands in a solid.

Fig. 5.4 (a) and Fig. 5.4 (b) show the electronic density of states of c-Si and a-Si respectively. Electronic density of states was evaluated by using a tight-binding model for silicon by Kwon [96]. The electronic structure of c-Si has several sharp features

due to Van Hove singularities in the Brillouin zone of c-Si, but these sharp features are missing in a-Si due to its lack of long-range order. Since the density of states of a-Si resembles a smeared crystalline density of states, it may come as a surprise that a-Si has a wider electronic band gap than c-Si. The band gap of c-Si depends on the magnitude and direction of the crystal momentum, with the direct $\Gamma$ band-gap (difference between the energy of the conduction band and the valence band at the $\Gamma$ point, located at zero crystal momentum) of about 3.4 eV [33]. The indirect character of the c-Si band gaps (minimum energy in the conduction band and the maximum energy in the valence band occur at different crystal momenta), however, reduces the band-gap of c-Si to about 1.1 eV. The band gap of a-Si lies between c-Si direct and indirect band gap, so the wider electronic band gap of a-Si can be seen as a result of smoothing out the indirect and anisotropic band gap of c-Si [110].

The band gap size a a-Si sample, obtained by measuring complex dielectric functions, is dependent on the preparation history [110]. The self-ion implanted samples have a band gap of $\Delta E_g = 0.85$ eV, evaporated samples have a band gap of $\Delta E_g = 1.12$ eV, and annealed samples (3 h at 500 °C) had the broadest band gap of $\Delta E_g = 1.30$ eV [26, 27]. The largest measured band gap of a-Si is observed in an annealed material, which exhibits the largest degree of hyperuniformity, confirming the behavior predicted by the NHN models (see Fig. 3.4).
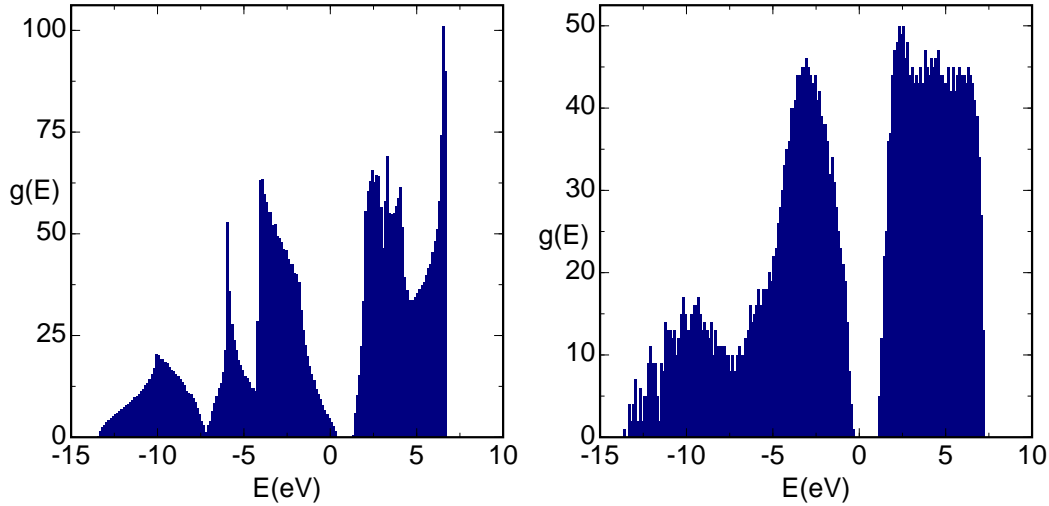
(a) Electronic density of states of c-Si     (b) Electronic density of states of a-Si

Figure 5.4: Electronic density of states of c-Si and a-Si. Energy of a state in eV is shown on the horizontal axis, density of states in arbitrary units is shown on the vertical axis. Sharp features of the c-Si density of states are smeared out in the a-Si and yet a-Si features a wider electronic band gap than c-Si. Density of states is calculated by the method of Kwon [96]. Electronic density of states of a-Si is calculated for a 1000-atom a-Si model produced by a Stillinger-Weber quench of a CRN network.

## 5.5 Vibrational Density of States of Amorphous Silicon

The vibrations of a crystalline solid can be decomposed into plane-wave modes (phonons) with definite wavevectors $\mathbf{k}$ and energy dispersion relation $E(\mathbf{k})$. In an amorphous solid that lacks periodicity, vibrational excitations no longer have well defined wavevectors, and thus we will focus on the phonon density of states instead. The vibrational density of states, $g(E)$, is defined so that $g(E)dE$ is the number of vibrational states between the energies $E$ and $E + dE$, which is a well defined concept in both crystalline and amorphous solids. The vibrational density of states

affects thermal properties of solids such as the thermal expansion, the thermal conductivity, and the specific heat, and also mechanical properties such as the sound wave propagation and attenuation.

Fig. 5.5 (a) and Fig. 5.5 (b) show the phonon densities of states $g(E)$ of c-Si and a-Si respectively. The crystalline sample features sharp Van Hove singularities resulting from the singularities on the Brillouin zone. The amorphous sample lacks the sharp features of the c-Si density of states, yet the transverse acoustic (TA) peak near $E/e = 1.5$ and the transverse optic (TO) peak near $E/e = 4.0$ are clearly identifiable. Positions of the TA and TO peaks are sensitive to the $\lambda$ parameter of the Stillinger-Weber potential and thus the ratio of the TO and TA peaks positions was used to fit the value of $\lambda$ parameter of the Stillinger-Weber potential by Vink et al. [76]. The phonon density of states of a-Si is calculated for a 1000 atom a-Si model produced by a Stillinger-Weber quench of a CRN network. The phonon density of states is obtained by diagonalizing the dynamical matrix (matrix of the second derivatives of the inter-atomic potential) calculated from the Stillinger-Weber interaction. The second derivatives of the two- and three-body isotropic potential used to evaluate the dynamical matrix are shown in Appendix B.
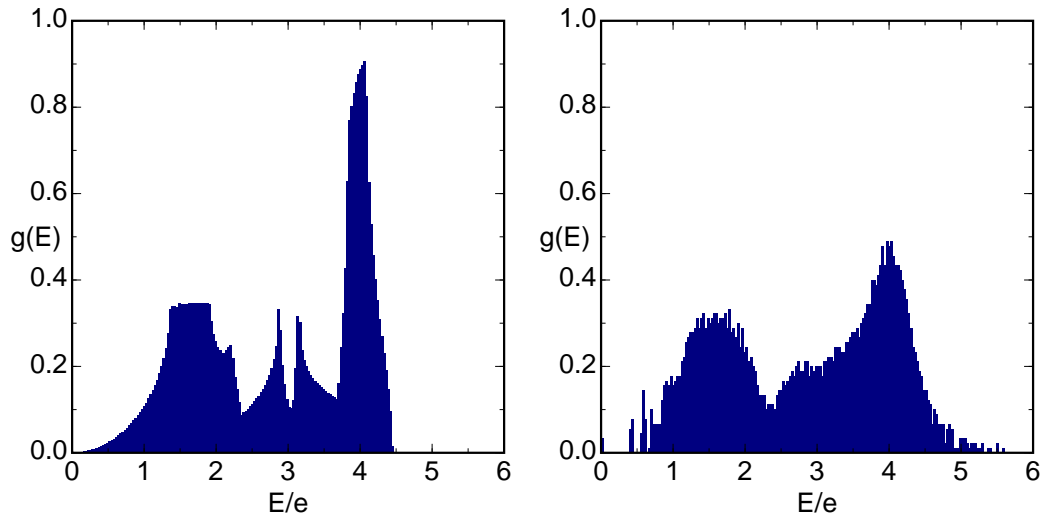
(a) Phonon density of states of c-Si          (b) Phonon density of states of a-Si

Figure 5.5: Phonon densities of states of c-Si and a-Si. The horizontal axis shows the energy of a phonon state in units of $e = 0.0151\,\text{eV}$; the vertical axis shows the density of states $g(E)$ in arbitrary units. The sharp features (Van Hove singularities) seen in the density of states of c-Si are smoothed-out in the a-Si sample. Despite the smoothing of the density of states, the transverse acoustic (TA) peak at $E_{TA}/e = 1.5$ and the transverse optic (TO) peak at $E_{TO}/e = 4.0$ are clearly identifiable. The phonon density of states shown in the figure of a-Si is calculated for a 1000-atom a-Si model produced by a Stillinger-Weber quench of a CRN network.

# Chapter 6

# Comparison of the NHN Models with Experiments

T HIS chapter is based on the experimental results obtained by diffraction measurements of Xie et al. [2] and Laaziri et al. [3, 4] on a sample of an edge-supported membrane of a-Si prepared by ion self-implantation [14]. The diffraction measurements provide the structure factor $S(k)$ as a function of the the wavenumber $k$. Using the Fourier transform, this structure factor function can be transformed to a pair correlation function $g(r)$. We will show that the nearly-hyperuniform models of a-Si are in better agreement with these experimental data than previously considered models, for both the structure factor and the pair correlation function.

## 6.1    Behavior of the NHN Models under Annealing

The best currently available measurements of the structure factor in the long-wavelength limit of an annealed sample of a-Si, obtained via transmission X-ray scattering at the Argonne Advanced Photon Source by Xie et al., indicate that

$S(k \to 0) = 0.0075 \pm 0.0005$ [2]. This is almost five times lower than the value predicted by de Graff and Thorpe [21] using the currently best available CRN configuration of Barkema and Mousseau (BM), obtained using the Keating potential [70]. This suggests that certain large-scale correlations present in a-Si are not accounted for in current CRN models.

In Fig. 6.1, we show $S(k \to 0)$ as a function of the inverse height $H^{-1}$ of the first scattering peak for the original K (BM) CRN model [21], for the CRN models with progressively higher level of annealing under the Keating potential K1-K5, and for the subsequent Stillinger-Weber quenched models SW1-SW5. Included in the figure are the experimental measurements for annealed and implanted a-Si samples [2]. The data obtained from the numerical K1-K5 and SW1-SW5 models show that, with more annealing $S(k \to 0)$ gets smaller and the first peak height gets larger (as does the first peak in the pair correlation function). The same trend is observed in the experimental data of as-implanted and annealed a-Si samples. We conclude that the K (BM) CRN model is not an endpoint of the annealing process. Instead, additional annealing moves the CRN models in the direction of increasing hyperuniformity (i.e. $S(k \to 0)$ gets smaller), increasing the height of the first scattering peak, and increasing the height of the first peak of the pair correlation function $g(r)$. It is also seen from the Fig. 6.1 that the SW models have values of $S(k \to 0)$ that are about 50% lower than the corresponding K models that were used as an initial state for a Stillinger-Weber quench. Our best nearly hyperuniform model, SW5, yields $S(k \to 0) = 0.010 \pm 0.0002$, which is appreciably smaller than that of the K (BM) CRN model $[S(k \to 0) = 0.035 \pm 0.0002]$ [21], and in between the values of the implanted and annealed experimental samples, being nearly equal to the latter $[S(k \to 0) = 0.0075 \pm 0.0005]$. The experimental values of $S(k \to 0)$ for the as-implanted and annealed a-Si samples are consistent with the nearly hyperuniform network picture.
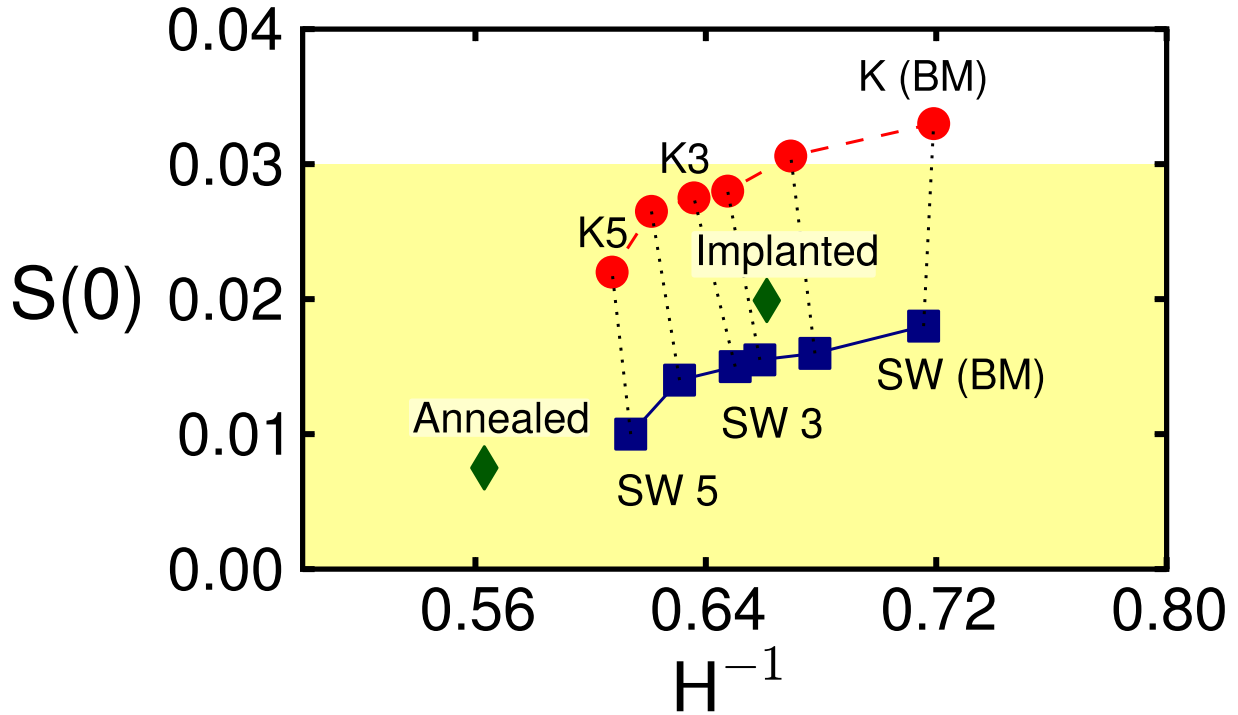
Figure 6.1: Values of $S(k \to 0)$ for the network structural models progressively relaxed with a Keating potential as a function of the inverse height $H^{-1}$ of the first scattering peak. Solid red circles represent the original Barkema-Mousseau model (labeled by K (BM)), and a series of progressive relaxations K1 through K5. The Keating-relaxed models serve as initial conditions for the subsequently quenched Stillinger-Weber structures, which appear as solid blue squares (labeled by SW). The experimental values for as-implanted a-Si and annealed a-Si appear as solid green diamonds. The trajectory of the experimental values fits well with the modified Stillinger-Weber results. The shaded region below $S(k \to 0) = 0.03$ indicates the nearly hyperuniform range in which $S(k \to 0)$ is below the equilibrium melting value for a-Si.

A recent study, using fluctuation electron microscopy (FEM) measurements and electron diffraction data as experimental constraints in a reverse Monte Carlo pro-

cedure with Tersoff inter-atomic potential, led to the suggestion [109, 111] that as-prepared a-Si is "paracrystalline", i.e. that it contains $1 - 2\,\text{nm}$ large regions with the topology of crystalline silicon (paracrystallites). Paracrystalline models of a-Si are heterogeneous on a nanometer-length scale due to the presence of paracrystallites embedded in a disordered (not necessarily CRN) matrix [109]. Since it can be inferred from the fluctuation electron microscopy data that annealing of a-Si leads to a reduction in paracrystallinity by a factor of 2 to 10 [20, 25, 112], and since $S(k \to 0)$ is expected to decrease with increasing crystalline order and thus with increasing level of paracrystallinity, paracrystalline models predict that $S(k \to 0)$ should decrease with annealing. This prediction of paracrystalline models is counter to both the theoretical predictions and the experimental data. We conclude that the observed low value for $S(k \to 0)$ is indeed a signature of hyperuniformity consistent with the nearly hyperuniform network picture.

## 6.2 Analysis of the Experimental Measurement of the Structure Factor

In the experimental measurement of $S(k)$, there is an upturn in the structure factor at the lowest values of the wavevector $k$, preventing a direct measurement of $S(k \to 0)$. This upturn is due to a small-angle scattering, primarily from surface roughness, and secondarily from a very small amount of nanoporosity. Surface roughness is expected especially on the matte side of the sample that was exposed to the chemical etch used to remove the crystal substrate. The upturn was observed to decrease with the reduction in the surface roughness.

A simple extrapolation of a straight line from the minimum value of $S(k)$ to $k = 0$ can be used to derive an upper limit on $S(k \to 0)$. This procedure yields $S(k \to 0)_{\text{upper limit}} = 0.026$ for the as-implanted a-Si sample and $S(k \to 0)_{\text{upper limit}} =$

0.016 for the annealed (relaxed) a-Si sample. Note that these values are below the computationally determined lower bound of $S(k \to 0) = 0.035$ suggested by de Graff and Thorpe [21], and that the value for annealed a-Si is lower than that for as-implanted a-Si.

A more precise estimate of the value of $S(k \to 0)$ is obtained by modeling the small-angle scattering from surface roughness. To model the upturn due to the surface scattering, we fit $S(k)$ between $k = 0.08\,\text{\AA}^{-1}$ and $0.4\,\text{\AA}^{-1}$ to the form $S(k) = ak^b + S(k \to 0) + S(k \to 0)k$. The first term is an approximation to the small-angle X-ray scattering, including both Guinier and Porod scattering from a range of surface feature sizes. The last two terms describe a linear contribution to $S(k)$ at small wavevector $k$. The measured $S(k)$, the best overall fits, and the best-fit linear contribution are shown in Fig. 6.2, where the fits are shown with solid lines. The exponent $b$, representing the surface scattering, is $b = -3.34 \pm 0.02$ for the as-implanted sample and $b = -2.40 \pm 0.03$ for the annealed (relaxed) sample. The linear portions of the fits are shown with dashed lines. Using the surface scattering model, we find that $S(k \to 0) = 0.0199 \pm 0.0005$ for the as-implanted and $S(k \to 0) = 0.0075 \pm 0.0005$ for the annealed (relaxed) a-Si. It is clear that annealing of the experimental samples increases the degree of hyperuniformity. Both samples are consistent with the nearly hyperuniform network models and both have $S(k \to 0)$ significantly lower than the de Graff-Thorpe lower bound [21].

We have also considered the more general six-parameter fitting function of the form $S(k) = ak^b + ck^d + S(k \to 0) + S(k \to 0)k$. We have found that the best-fit $S(k \to 0)$ is less than the value reported above with essentially the same goodness of fit. Hence, the values above could be considered conservative upper bounds.

The values of the terminal slopes are $S'(k \to 0) = 0.0188 \pm 0.0009\,\text{\AA}$ for the as-implanted a-Si and $S'(k \to 0) = 0.0260 \pm 0.0005\,\text{\AA}$ for the annealed (relaxed) a-Si. It is noteworthy that the linear approximation is a good fit to the behavior of
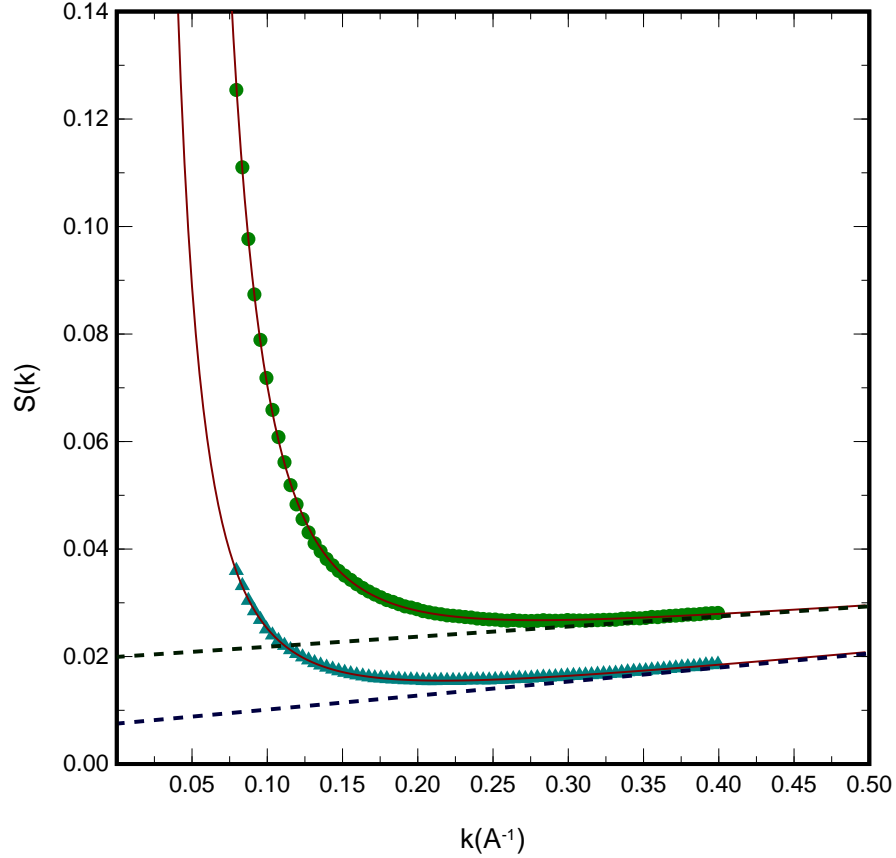
Figure 6.2: $S(k)$ at low $k$ for the as-implanted a-Si (circles) and the annealed (relaxed) a-Si (triangles). Note that the minimum values of $S(k)$ for both as-implanted and annealed are less than 0.03, below the theoretical bounds based on continuous random network models relaxed with Keating potentials or on treating a-Si as a frozen-liquid. To obtain $S(k \to 0)$, the data are fit (solid curves) to a sum of an inverse power-law in $k$, representing small angle scattering mostly from a rough etched surface, and a linear contribution. The dashed lines show the linear contribution only. The plot shows that this ansatz fits well (see text for details). We measure the degree of hyperuniformity to be $S(k \to 0) = 0.0199 \pm 0.0005$ for the as-implanted a-Si and $S(k \to 0) = 0.0075 \pm 0.0005$ for the annealed a-Si.

$S(k)$ for small wavenumber and agrees with what has been observed in MRJ sphere packings [36].

## 6.3 Comparison of the Structure Factor obtained from NHN models to the Experiments

The computational models presented in Chapter 3 demonstrate that increased annealing results in increased height of the first peak in the pair correlation function, narrower bond angle distribution, and increased dihedral angle ordering, see Tables 5.2 and 5.1 in Chapter 5. Each of these characteristics can be taken as an indicator of the state of relaxation of the network model. All of these results are confirmed by the experimental results of Xie et al. [2] and the earlier experiments [3, 4] that obtained the pair correlation function in the same samples of a-Si. These experimental studies observed that the same changes were induced by thermal annealing. The increase in height and the narrowing of the first peak with annealing observed in computational models (see Fig. 6.3) results in the extension of the exponential decay length of the density oscillations in the pair distribution function, with periodicity given by the wavevector of the first scattering peak in the structure factor. These predictions are confirmed by the recent analysis [30].

The experimental measurements [3, 4] show that during thermal annealing the average coordination number increases from 3.79 to 3.88, which means that annealed a-Si is closer to ideal network models with average coordination number 4 than as-implanted a-Si. Based on experimental values derived from the width of the first and the second peaks in the radial distribution function, the bond angle distribution for the as-implanted a-Si was reported as $\Delta\theta = 10.45°\pm0.09°$ and for the annealed sample as $\Delta\theta = 9.63° \pm 0.08°$ [3]. Later, a more sophisticated analysis [30], that takes into account a contribution from third nearest neighbors in addition to the contribution from the first and the second suggested that the value for the bond angle deviation, as deduced from the width of the first and second peaks only, may be overestimated

by as much as 1.5°. The nearly hyperuniform models are in agreement with the experimental results derived the latter, more sophisticated, analysis.

Previously, de Graff and Thorpe used a K (BM) 100,000-atom model relaxed with the Keating interatomic potential to predict the value of $S(k \to 0)$ of a-Si to be $S(k \to 0) = 0.035 \pm 0.001$ [21]. It can be seen from Table 5.1 and Fig. 6.1 that the K (BM) model is not sufficiently relaxed. It has a bond angle deviation $\Delta\theta = 9.94°$, which is larger than what is experimentally observed even in the as-implanted a-Si sample, it lacks the third neighbor ordering [113] observed in experiments, and the first peak in the structure factor is too short and too wide compared to what is observed experimentally. The K (BM) models is relaxed by the Keating potential, which is less realistic than the Stillinger-Weber potential used to obtain the NHN models. The insufficient structural relaxation and unsatisfactory inter-atomic potential explain why the K (BM) model overestimates the limit of long wavelength scattering.

The nearly hyperuniform network models introduced in Chapter 3 on the other hand present a spectrum of models with $S(k \to 0)$ ranging from the value proposed by de Graff and Thorpe based on the frozen-liquid picture to the values comparable to the experimental values reported by Xie et al. [2]. The structure of our most annealed NHN model, SW5, is significantly more relaxed than the K (BM) model, as demonstrated by a bond-angle standard deviation that is more than a degree lower than that of the K (BM) model, which makes the structure of the SW5 model a better fit to the experiments. Additionally, while the height of the first peak of $S(k)$ of the SW5 model lies between those of the annealed and implanted samples, the corresponding K (BM) value is lower than both experimental values, as shown in Fig. 6.3.

For larger wavenumbers, our SW5 model again yields better agreement with the experimental data for the structure factor; see Fig. 6.4. In particular, the K (BM) CRN model predicts a significantly faster decay of the large-$k$ oscillations in $S(k)$
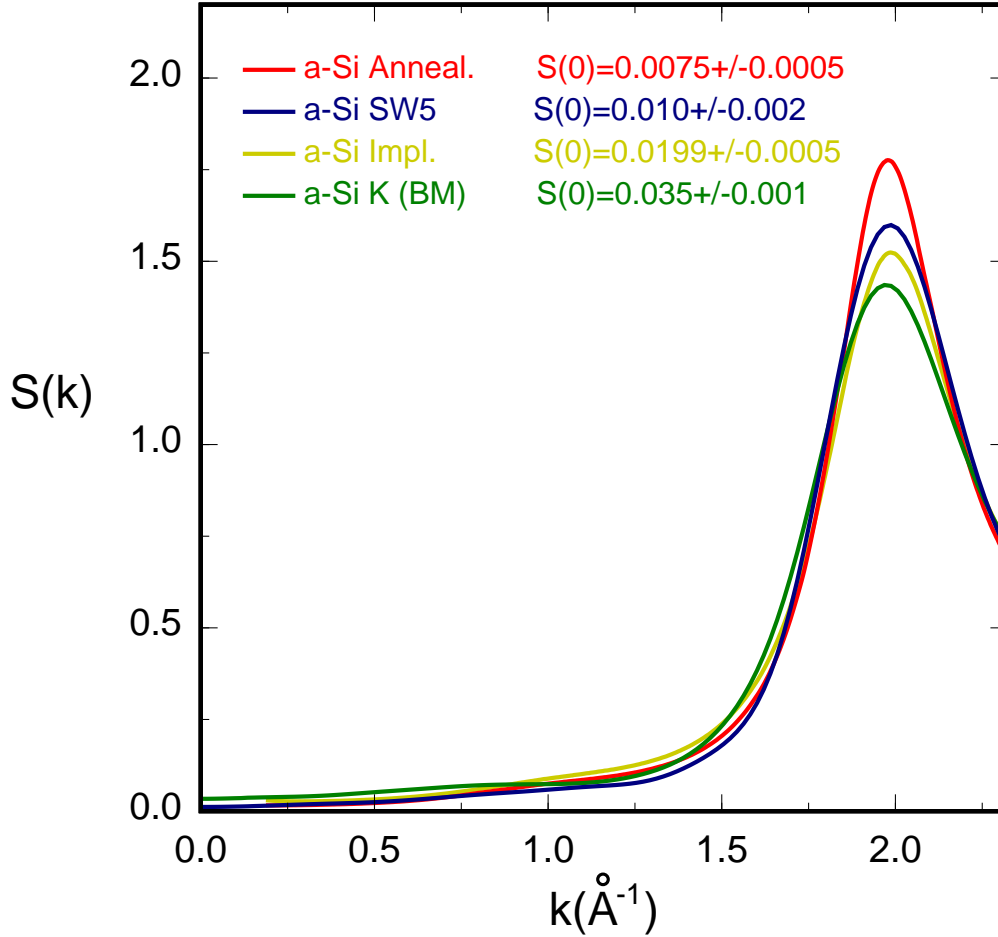
Figure 6.3: Comparison of the angularly averaged structure factor $S(k)$ versus $k$ for small $k$ for the SW5 model (blue curve) and the K (BM) CRN model [70] (green line) to those of the experimental measurements on annealed and implanted a-Si samples obtained by Xie et al. [2] (red and yellow curves). The values of $S(k \to 0)$ are indicated in the legend.

than does the SW5 model, which agrees well with the corresponding experimental values of the structure factor of Laaziri et al. [3]. We thus conclude that the SW5 model provides an improvement upon other predictions of the K (BM) CRN model.
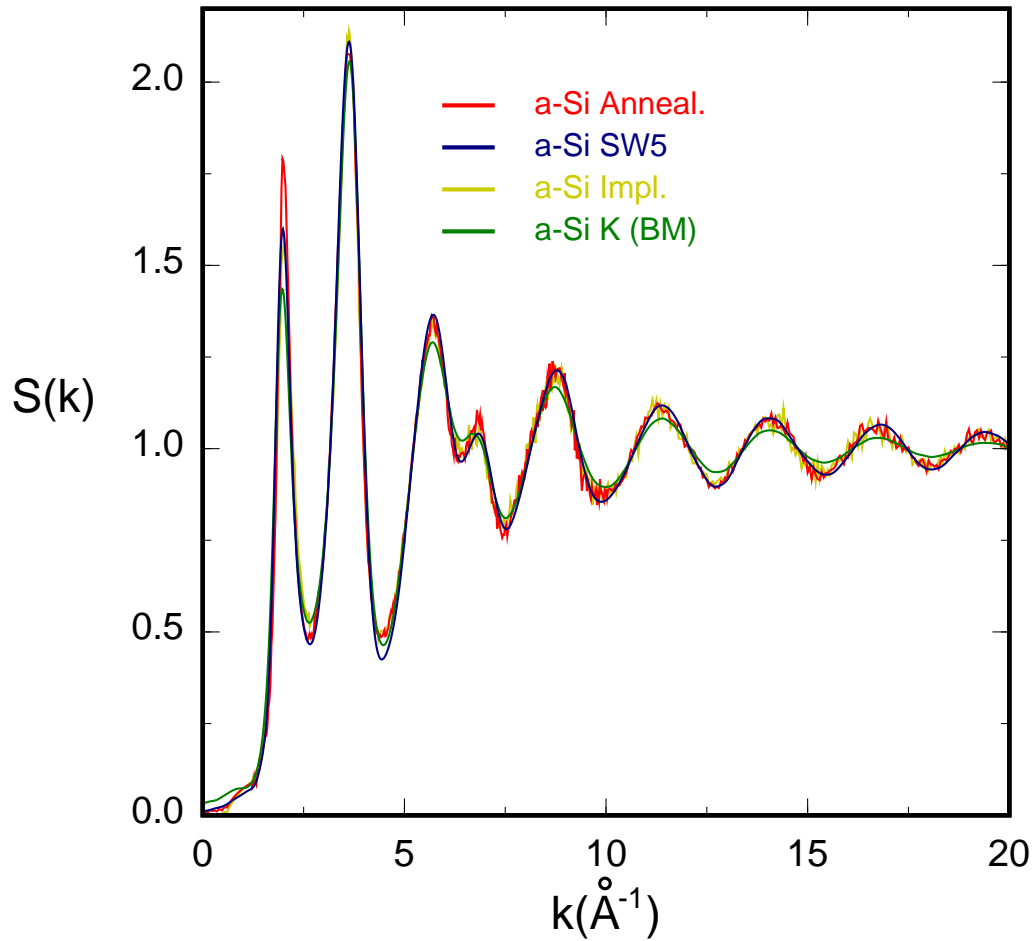
Figure 6.4: Comparison of the angularly averaged structure factor $S(k)$ versus $k$ at large $k$ for the SW5 model (blue curve) and the K (BM) CRN model [70] (green curve) to those of the experimental measurements on annealed and implanted a-Si samples of Laaziri et al. [3] (red and yellow curves).

## 6.4 Comparison of the Pair Correlation Function obtained from NHN models to the Experiments

The local coordination structure is captured better by the SW5 model than the K (BM) CRN model, as shown in Fig. 6.5 for the pair correlation function $g(r)$. It is seen that the K (BM) CRN model predicts a significantly broader first peak in $g(r)$ (due to a larger bond-length variation) than the experimentally measured one, which is captured well by the SW5 model.

Using a two-step numerical procedure consisting of bond-switching annealing relaxation and Stillinger-Weber quenching, we have shown that there are nearly hyperuniform models that perform better than the benchmark Barkema and Mousseau K (BM) CRN model in reproducing the observed $S(k \to 0)$. As the annealing (via the Keating potential) time increases, the value $S(k \to 0)$ decreases (i.e. degree of hyperuniformity increases) from the initial maximum value associated with the K (BM) CRN model. Moreover, when these modified CRN models are relaxed under the SW potential, the resulting NHN states are endowed with values of $S(k \to 0)$ that are smaller than those of their CRN counterparts by a factor of 1/2. Based on our numerical investigation, we conclude that the value of $S(k \to 0)$ cannot be considered a universal quantity for a-Si or for any other amorphous tetrahedral network, as suggested by de Graff and Thorpe [21]. It should not go unnoticed that our SW5 model provides better predictions of other observed structural features, including bond-length and bond-angle statistics, height of the first scattering peak, long-range oscillations of $S(k)$, and the first peak in $g(r)$.
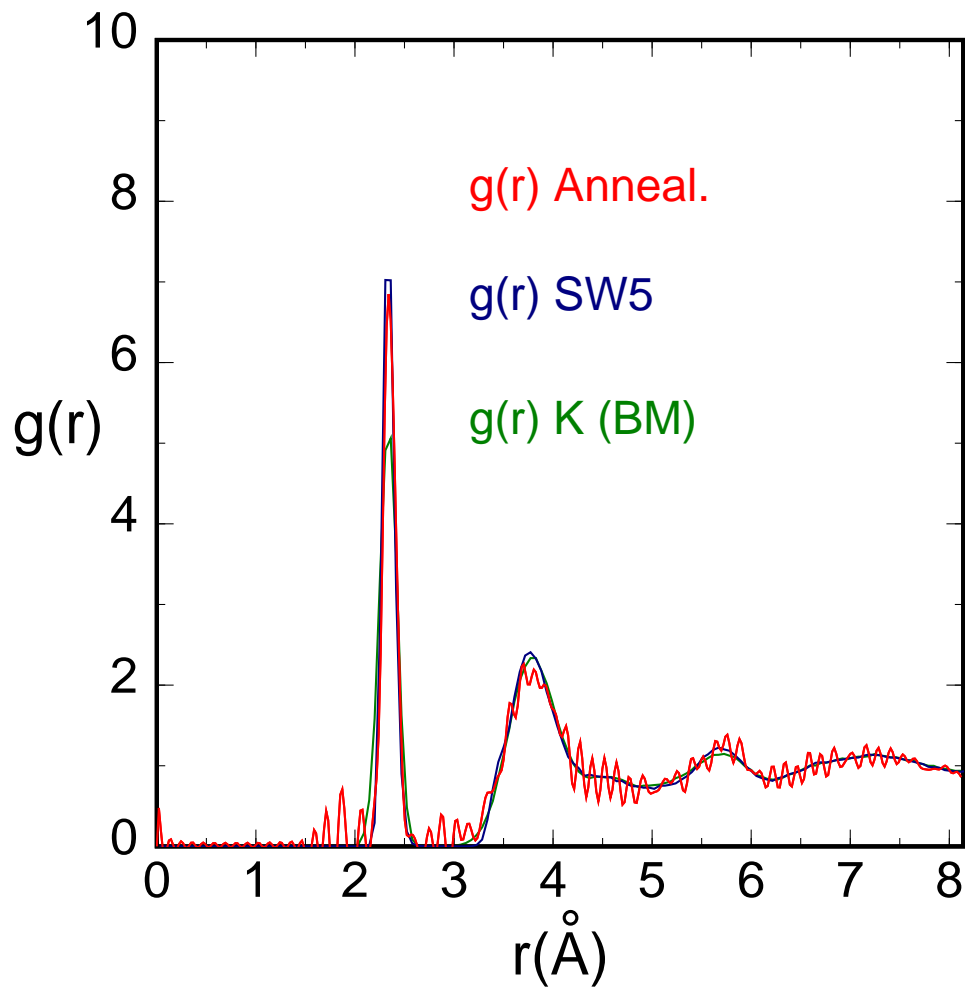
Figure 6.5: Comparison of the radial distribution function $g(r)$ versus radial distance $r$ measured experimentally by Laaziri et al. [3] for an annealed a-Si sample (red curve) to the K (BM) CRN model [70] (green curve) and the SW5 model (blue curve).

# Chapter 7

# Conclusion

## 7.1 Summary

WE have presented a new model for the structure of amorphous silicon, the nearly hyperuniform network (NHN) model. We have shown that the value of the structure factor in the limit of infinite wavelength $S(k \to 0)$ in the NHN models depends on the amount of relaxation, and is different from the value obtained from the CRN model of Barkema and Mousseau. Hence, the value of $S(k \to 0)$ cannot be considered a universal quantity, as conjectured by de Graff and Thorpe [21]. The exact opposite is true: By varying the level of relaxation, we have obtained a spectrum of NHN models with varying degrees of hyperuniformity, and we have succeeded in constructing a NHN model, which is more than a factor of 3 closer to hyperuniformity than what the frozen-liquid picture predicts. We have shown that annealing increases the degree of hyperuniformity (i.e. $S(k \to 0)$ is smaller) and that the degree of annealing correlates with quantities of theoretical interest, such as the height of the first scattering peak in the structure

factor, and with quantities of practical interest, such as the width of the electronic band gap.

We have demonstrated that the NHN models perform better than the CRN models in reproducing the observed structure factor $S(k)$, the pair correlation function $g(r)$, and other structural characteristics, such as the variance of the bond-length and the bond-angle distribution. High-sensitivity X-ray scattering data indicate that as-implanted and annealed a-Si have a nearly hyperuniform disordered atomic structure in agreement with the NHN models. The observed value of $S(k \to 0) = 0.0075 \pm 0.0005$ for annealed a-Si is significantly smaller than the theoretical lower bound offered by de Graff and Thorpe [21], but is consistent with the predictions of the NHN models.

## 7.2   Future Work

Since the results presented in this thesis touch diverse topics, it is inevitable that some of the questions have been left unanswered. These include the structural origin of the scattering enhancement near $k = 1 \,\text{Å}^{-1}$, the possibility of a perfect hyperuniformity in disordered tetrahedral solids with soft, short-range interactions, and the origin of the linear behavior of $S(k)$ as $k \to 0$.

## Perfect Hyperuniformity of Disordered Tetrahedral Solids with Soft, Short-Range Interaction

Whether true hyperuniformity can be achieved in a disordered many-body system with soft, short-range interparticle interactions remains an open question. Hyperuniformity has been observed in systems with hard, short-range interactions, including a large class of maximally random jammed packings [36, 37]. Hyperuniformity is also found in systems with soft, long-range interactions; for example, in one-component

plasmas [42, 44] or in the ground states of stealthy potentials [46]. The existence of these diverse examples suggest that one cannot rule out the existence of hyperuniform amorphous tetrahedral network models. In fact, the extrapolation of Fig. 3.1 suggests it may indeed be possible. The search for the perfectly hyperuniform tetrahedral network models represents an exciting and challenging area for future research.

## Scattering Enhancement near $k = 1\,\text{Å}^{-1}$

The structure factor $S(k)$ for both as-implanted and annealed samples exhibits a small broad peak that has not been examined previously. This scattering enhancement feature close to $k = 1\,\text{Å}^{-1}$ and well below the first diffraction peak near $k = 2\,\text{Å}^{-1}$ is observed both in NHN models and in the experiment (see Fig. 6.3 in Chapter 6). Diffraction peaks between $k = 1\,\text{Å}^{-1}$ and $k = 2\,\text{Å}^{-1}$ are indicative of the medium-range order on a scale of about 6-20 Å, a scale that is not well understood in disordered materials despite being the subject of intense interest [114]. The scattering enhancement may bring insights into the packing of the structural tetrahedra of a-Si. Neither the scattering enhancement in a-Si nor any of its structural analogues in other tetrahedral amorphous materials have been studied. Amorphous silicon, being a monoatomic solid provides possibly the simplest example of this phenomenon with implications for the structure of other disordered tetrahedral materials, such as $Ge, SiO_2, GeO_2$, and $H_2O$.

The structural cause of the scattering enhancement near $k = 1\,\text{Å}^{-1}$ remains unknown. We speculate that the enhancement is caused by energetically favorable cage structures in the network or perhaps by correlations between dihedral angles in the "backbone" structures running through the network. We note that the small scattering enhancement has been found in NHN models without dangling bonds or defects, which suggests that coordination defects and their clusters cannot explain the struc-

tural origin of this feature. The nature of these possible causes and their impact on the structural properties of a-Si is the subject of a future study.

## Linear Decay of the Structure Factor

The structure factor $S(k)$ of both the NHN models and the experiments show a linear behavior as $k \to 0$. Similar behavior was observed in the hyperuniform maximally jammed random packings consisting of hard spheres particles, where the linear behavior is related to a weak power-law tail in the pair correlation function $(g(r) - 1 \sim -1/r^4$ [36]). Although our NHN samples are not large enough to investigate the precise character of the decay of the structure factor at small $k$ and the pair correlation function at large $r$, it presents an intriguing direction for future research.

## Failure of the Paracrystalline Models

Our findings do not support the paracrystalline models of a-Si. The NHN models provide a much better fit for the data without the need of any artificial assumption of paracrystallinity. It has been argued [109, 115] that the paracrystalline model is the only model of a-Si capable of explaining a fluctuation electron microscopy (FEM) measurements [116]. It is possible, however, that the SW1-5 models are capable of explaining the FEM data without the presence of paracrystallites and with models involving only physical short-range interactions.

## Practical Uses of Controlling the Electronic Band Gap

The capability to fine tune the size of an electronic band gap is desirable in applications of a-Si to microelectronics, solar panels and many others discussed in Chapter 1. The search for new, yet unknown applications for band-gap control in amorphous

semiconductors is likely to lead to other possible technological applications. Similar ideas have successfully led to the creation of novel hyperuniform disordered materials with tunable photonic band gaps [54–57]. A provisional patent for the invention of "Hyperuniform and Nearly Hyperuniform Random Network Materials" has been filed with the United States Patent and Trademark Office.

# Appendix A

# Bonding Constraints in

# Amorphous Silicon

We present a mean field theory argument to estimate the degree of overconstraint of covalent solids. We will assume that the character of the inter-atomic interaction in the solid is such that it constrains the bond lengths and bond angles to lie in a narrow range, but it does not pose significant constraints on atoms that lie beyond the second coordination shell (i.e. it does not constrain dihedral angles etc.).

In these situations, the amount of over-constraint can be seen from the following constraint counting argument (see [117, 118]). Let us suppose that there are $n_r$ atoms with coordination $r$ ($r \in \mathbb{Z}_{\geq 2}$), so we have for the number of atoms

$$N = \sum_{r=1}^{\infty} n_r, \tag{A.1}$$

and for the average atomic coordination

$$\overline{r} = \frac{\sum_{r=1}^{\infty} r n_r}{\sum_{r=1}^{\infty} n_r}. \tag{A.2}$$

There is a one constraint for each bond and since each bond is shared by two atoms, there are $r/2$ bond constraints per $r-$coordinated atom. There are also $2r - 3$ independent angles between the bonds of an $r-$coordinated atom, since the direction of a bond can be specified by two angles with respect to a fixed reference frame and there are 3 independent rotation of the reference frame.

It follows that the number of constraints per atom $N_c/N$ is

$$\frac{N_c}{N} = \frac{\sum_{r=1}^{\infty} \left[ r/2 + (2r - 3) \right] n_r}{\sum_{r=1}^{\infty} n_r} = \frac{5}{2}\bar{r} - 3. \tag{A.3}$$

Given that $\bar{r} = 4$ in the perfectly tetrahedrally bonded network, we obtain that the number of constraints per atom is $N_c/N = 7$. Seven constraints per atom is by far exceeding the three translational degrees of freedom per atom. This demonstrates the high degree of over-constraint found in a-Si.

# Appendix B

# First and Second Derivatives of an Isotropic potential

## B.1 Two-Body Isotropic Potential

The two-body term of the Stillinger-Weber potential is isotropic and thus can be written as

$$V = V(|\mathbf{r_{ij}}|). \tag{B.1}$$

The first derivative of the two-body term of the Stillinger-Weber potential can be written as

$$V' = d_r V(|\mathbf{r_{ij}}|) \frac{(\mathbf{r_{ij}} \cdot \delta\mathbf{r_{ij}})}{|\mathbf{r_{ij}}|}. \tag{B.2}$$

The second derivative of the two-body term of the Stillinger-Weber potential can be written as

$$V'' = \frac{1}{2}\frac{d_r V(|\mathbf{r_{ij}}|)}{|\mathbf{r_{ij}}|}(\delta\mathbf{r_{ij}} \cdot \delta\mathbf{r_{ij}})$$
$$+ \frac{1}{2}\left[\frac{d_r d_r V(|\mathbf{r_{ij}}|)}{|\mathbf{r_{ij}}|^2} - \frac{d_r V(|\mathbf{r_{ij}}|)}{|\mathbf{r_{ij}}|^3}\right](\mathbf{r_{ij}} \cdot \delta\mathbf{r_{ij}})(\mathbf{r_{ij}} \cdot \delta\mathbf{r_{ij}}). \tag{B.3}$$

## B.2   Three-Body Isotropic Potential

The three-body term of the Stillinger-Weber potential is isotropic and thus can be written as

$$V = V(|\mathbf{r_{ij}}|, |\mathbf{r_{im}}|, \cos\theta_{ijm}). \tag{B.4}$$

The first derivative of the three-body term of the Stillinger-Weber potential can be written as

$$V' = \left[\frac{d_{r_1}V(|\mathbf{r_{ij}}|, |\mathbf{r_{im}}|, \cos\theta_{ijm})}{|\mathbf{r_{ij}}|} - \cos\theta_{ijm}\frac{d_{cos\theta}V(|\mathbf{r_{ij}}|, |\mathbf{r_{im}}|, \cos\theta_{ijm})}{|\mathbf{r_{ij}}|^2}\right](\mathbf{r_{ij}} \cdot \delta\mathbf{r_{ij}})$$
$$+ \left[\frac{d_{r_2}V(|\mathbf{r_{ij}}|, |\mathbf{r_{im}}|, \cos\theta_{ijm})}{|\mathbf{r_{im}}|} - \cos\theta_{ijm}\frac{d_{cos\theta}V(|\mathbf{r_{ij}}|, |\mathbf{r_{im}}|, \cos\theta_{ijm})}{|\mathbf{r_{im}}|^2}\right](\mathbf{r_{im}} \cdot \delta\mathbf{r_{im}})$$
$$+ \left[\frac{d_{cos\theta}V(|\mathbf{r_{ij}}|, |\mathbf{r_{im}}|, \cos\theta_{ijm})}{|\mathbf{r_{ij}}||\mathbf{r_{im}}|}\right][(\mathbf{r_{im}} \cdot \delta\mathbf{r_{ij}}) + (\mathbf{r_{ij}} \cdot \delta\mathbf{r_{im}})]. \tag{B.5}$$

The second derivative of the three-body term of the Stillinger-Weber potential can be written as (shown on the following page)

$$
\begin{aligned}
V = & \frac{1}{2}\left[\frac{d_{r_1}V(|\mathbf{r_{ij}}|,|\mathbf{r_{im}}|,\cos\theta_{ijm})}{|\mathbf{r_{ij}}|} - \cos\theta_{ijm}\frac{d_{\cos\theta}V(|\mathbf{r_{ij}}|,|\mathbf{r_{im}}|,\cos\theta_{ijm})}{|\mathbf{r_{ij}}|^2}\right](\delta\mathbf{r_{ij}}\cdot\delta\mathbf{r_{ij}}) \\
& + \frac{1}{2}\left[\frac{d_{r_2}V(|\mathbf{r_{ij}}|,|\mathbf{r_{im}}|,\cos\theta_{ijm})}{|\mathbf{r_{im}}|} - \cos\theta_{ijm}\frac{d_{\cos\theta}V(|\mathbf{r_{ij}}|,|\mathbf{r_{im}}|,\cos\theta_{ijm})}{|\mathbf{r_{im}}|^2}\right](\delta\mathbf{r_{im}}\cdot\delta\mathbf{r_{im}}) \\
& + \frac{1}{2}\left[2\frac{d_{\cos\theta}V(|\mathbf{r_{ij}}|,|\mathbf{r_{im}}|,\cos\theta_{ijm})}{|\mathbf{r_{ij}}||\mathbf{r_{im}}|}\right](\delta\mathbf{r_{ij}}\cdot\delta\mathbf{r_{im}}) \\
& + \frac{1}{2}\left[\frac{d_{r_1}d_{r_1}V(|\mathbf{r_{ij}}|,|\mathbf{r_{im}}|,\cos\theta_{ijm})}{|\mathbf{r_{ij}}|^2} - \frac{d_{r_1}V(|\mathbf{r_{ij}}|,|\mathbf{r_{im}}|,\cos\theta_{ijm})}{|\mathbf{r_{ij}}|^3} + 3\cos\theta_{ijm}\frac{d_{\cos\theta}V(|\mathbf{r_{ij}}|,|\mathbf{r_{im}}|,\cos\theta_{ijm})}{|\mathbf{r_{ij}}|^4}\right. \\
& \left. + \cos^2\theta_{ijm}\frac{d_{\cos\theta}d_{\cos\theta}V(|\mathbf{r_{ij}}|,|\mathbf{r_{im}}|,\cos\theta_{ijm})}{|\mathbf{r_{ij}}|^4}\right](\mathbf{r_{ij}}\cdot\delta\mathbf{r_{ij}})(\mathbf{r_{ij}}\cdot\delta\mathbf{r_{ij}}) \\
& + \frac{1}{2}\left[\frac{d_{r_2}d_{r_2}V(|\mathbf{r_{ij}}|,|\mathbf{r_{im}}|,\cos\theta_{ijm})}{|\mathbf{r_{im}}|^2} - \frac{d_{r_2}V(|\mathbf{r_{ij}}|,|\mathbf{r_{im}}|,\cos\theta_{ijm})}{|\mathbf{r_{im}}|^3} + 3\cos\theta_{ijm}\frac{d_{\cos\theta}V(|\mathbf{r_{ij}}|,|\mathbf{r_{im}}|,\cos\theta_{ijm})}{|\mathbf{r_{im}}|^4}\right. \\
& \left. + \cos^2\theta_{ijm}\frac{d_{\cos\theta}d_{\cos\theta}V(|\mathbf{r_{ij}}|,|\mathbf{r_{im}}|,\cos\theta_{ijm})}{|\mathbf{r_{im}}|^4}\right](\mathbf{r_{im}}\cdot\delta\mathbf{r_{im}})(\mathbf{r_{im}}\cdot\delta\mathbf{r_{im}}) \\
& + \frac{1}{2}\left[2\frac{d_{r_1}d_{r_2}V(|\mathbf{r_{ij}}|,|\mathbf{r_{im}}|,\cos\theta_{ijm})}{|\mathbf{r_{ij}}||\mathbf{r_{im}}|} + 2\cos\theta_{ijm}\frac{d_{\cos\theta}V(|\mathbf{r_{ij}}|,|\mathbf{r_{im}}|,\cos\theta_{ijm})}{|\mathbf{r_{ij}}|^2|\mathbf{r_{im}}|^2} + 2\cos^2\theta_{ijm}\frac{d_{\cos\theta}d_{\cos\theta}V(|\mathbf{r_{ij}}|,|\mathbf{r_{im}}|,\cos\theta_{ijm})}{|\mathbf{r_{ij}}|^2|\mathbf{r_{im}}|^2}\right](\mathbf{r_{ij}}\cdot\delta\mathbf{r_{ij}})(\mathbf{r_{im}}\cdot\delta\mathbf{r_{im}}) \\
& - 2\cos\theta_{ijm}\frac{d_{r_1}d_{\cos\theta}V(|\mathbf{r_{ij}}|,|\mathbf{r_{im}}|,\cos\theta_{ijm})}{|\mathbf{r_{ij}}|^2|\mathbf{r_{im}}|}\Bigg](\mathbf{r_{ij}}\cdot\delta\mathbf{r_{ij}})(\mathbf{r_{im}}\cdot\delta\mathbf{r_{im}}) \\
& + \frac{1}{2}\left[-2\frac{d_{\cos\theta}V(|\mathbf{r_{ij}}|,|\mathbf{r_{im}}|,\cos\theta_{ijm})}{|\mathbf{r_{ij}}|^3|\mathbf{r_{im}}|} - 2\cos\theta_{ijm}\frac{d_{\cos\theta}d_{\cos\theta}V(|\mathbf{r_{ij}}|,|\mathbf{r_{im}}|,\cos\theta_{ijm})}{|\mathbf{r_{ij}}|^3|\mathbf{r_{im}}|} + 2\frac{d_{r_1}d_{\cos\theta}V(|\mathbf{r_{ij}}|,|\mathbf{r_{im}}|,\cos\theta_{ijm})}{|\mathbf{r_{ij}}|^2|\mathbf{r_{im}}|}\right](\mathbf{r_{im}}\cdot\delta\mathbf{r_{ij}})(\mathbf{r_{ij}}\cdot\delta\mathbf{r_{ij}}) \\
& + \frac{1}{2}\left[-2\frac{d_{\cos\theta}V(|\mathbf{r_{ij}}|,|\mathbf{r_{im}}|,\cos\theta_{ijm})}{|\mathbf{r_{ij}}||\mathbf{r_{im}}|^3} - 2\cos\theta_{ijm}\frac{d_{\cos\theta}d_{\cos\theta}V(|\mathbf{r_{ij}}|,|\mathbf{r_{im}}|,\cos\theta_{ijm})}{|\mathbf{r_{ij}}||\mathbf{r_{im}}|^3} + 2\frac{d_{r_2}d_{\cos\theta}V(|\mathbf{r_{ij}}|,|\mathbf{r_{im}}|,\cos\theta_{ijm})}{|\mathbf{r_{ij}}||\mathbf{r_{im}}|^2}\right](\mathbf{r_{ij}}\cdot\delta\mathbf{r_{im}})(\mathbf{r_{im}}\cdot\delta\mathbf{r_{im}}) \\
& + \frac{1}{2}\left[-2\frac{d_{\cos\theta}V(|\mathbf{r_{ij}}|,|\mathbf{r_{im}}|,\cos\theta_{ijm})}{|\mathbf{r_{ij}}|^3|\mathbf{r_{im}}|} - 2\cos\theta_{ijm}\frac{d_{\cos\theta}d_{\cos\theta}V(|\mathbf{r_{ij}}|,|\mathbf{r_{im}}|,\cos\theta_{ijm})}{|\mathbf{r_{ij}}|^3|\mathbf{r_{im}}|} + 2\frac{d_{r_1}d_{\cos\theta}V(|\mathbf{r_{ij}}|,|\mathbf{r_{im}}|,\cos\theta_{ijm})}{|\mathbf{r_{ij}}|^2|\mathbf{r_{im}}|}\right](\mathbf{r_{ij}}\cdot\delta\mathbf{r_{ij}})(\mathbf{r_{ij}}\cdot\delta\mathbf{r_{im}}) \\
& + \frac{1}{2}\left[-2\frac{d_{\cos\theta}V(|\mathbf{r_{ij}}|,|\mathbf{r_{im}}|,\cos\theta_{ijm})}{|\mathbf{r_{ij}}||\mathbf{r_{im}}|^3} - 2\cos\theta_{ijm}\frac{d_{\cos\theta}d_{\cos\theta}V(|\mathbf{r_{ij}}|,|\mathbf{r_{im}}|,\cos\theta_{ijm})}{|\mathbf{r_{ij}}||\mathbf{r_{im}}|^3} + 2\frac{d_{r_2}d_{\cos\theta}V(|\mathbf{r_{ij}}|,|\mathbf{r_{im}}|,\cos\theta_{ijm})}{|\mathbf{r_{ij}}||\mathbf{r_{im}}|^2}\right](\mathbf{r_{im}}\cdot\delta\mathbf{r_{ij}})(\mathbf{r_{im}}\cdot\delta\mathbf{r_{im}}) \\
& + \frac{1}{2}\left[\frac{d_{\cos\theta}d_{\cos\theta}V(|\mathbf{r_{ij}}|,|\mathbf{r_{im}}|,\cos\theta_{ijm})}{|\mathbf{r_{ij}}|^2|\mathbf{r_{im}}|^2}\right]\left[(\mathbf{r_{im}}\cdot\delta\mathbf{r_{ij}})(\mathbf{r_{im}}\cdot\delta\mathbf{r_{ij}}) + 2(\mathbf{r_{im}}\cdot\delta\mathbf{r_{ij}})(\mathbf{r_{ij}}\cdot\delta\mathbf{r_{im}}) + (\mathbf{r_{ij}}\cdot\delta\mathbf{r_{im}})(\mathbf{r_{ij}}\cdot\delta\mathbf{r_{im}})\right].
\end{aligned}
\tag{B.6}
$$

103

# Bibliography

[1] M. Hejna, P. J. Steinhardt, and S. Torquato, Phys. Rev. B **87**, 245204 (2013), URL http://link.aps.org/doi/10.1103/PhysRevB.87.245204.

[2] R. Xie, G. G. Long, S. J. Weigand, S. Roorda, S. C. Moss, P. J. Steinhardt, and S. Torquato, Proc. Nat. Acad. Sci. USA (2012).

[3] K. Laaziri, S. Kycia, S. Roorda, M. Chicoine, J. L. Robertson, J. Wang, and S. C. Moss, Phys. Rev. B **60**, 13520 (1999), URL http://link.aps.org/doi/10.1103/PhysRevB.60.13520.

[4] K. Laaziri, S. Kycia, S. Roorda, M. Chicoine, J. L. Robertson, J. Wang, and S. C. Moss, Phys. Rev. Lett. **82**, 3460 (1999), URL http://link.aps.org/doi/10.1103/PhysRevLett.82.3460.

[5] R. Street, *Technology and Applications of Amorphous Silicon*, Springer Series in Materials Science (Springer, 2000), ISBN 9783540657149, URL http://books.google.com/books?id=tZFyXvnoHUEC.

[6] R. Street, *Hydrogenated Amorphous Silicon*, Cambridge Solid State Science Series (Cambridge University Press, 2005), ISBN 9780521019347, URL http://books.google.com/books?id=zQMwsMt4VmoC.

[7] A. Snell, K. Mackenzie, W. Spear, P. LeComber, and A. Hughes, Applied Physics A: Materials Science & Processing **24**, 357 (1981), ISSN 0947-8396, 10.1007/BF00899734, URL http://dx.doi.org/10.1007/BF00899734.

[8] A. Shah, J. Meier, A. Buechel, U. Kroll, J. Steinhauser, F. Meillaud, H. Schade, and D. Domin, Thin Solid Films **502**, 292 (2006), ISSN 0040-6090, selected Papers from the 5th International Conference on Coatings on Glass (ICCG5)- Advanced Coatings on Glass and Plastics for Large-Area or High-Volume Products, URL http://www.sciencedirect.com/science/article/pii/S0040609005011685.

[9] M. Rose, J. Hajto, P. Lecomber, S. Gage, W. Choi, A. Snell, and A. Owen, Journal of Non-Crystalline Solids **115**, 168 (1989), ISSN 0022-3093, URL http://www.sciencedirect.com/science/article/pii/0022309389903943.

[10] M. Konagai, Japanese Journal of Applied Physics **50**, 030001 (2011), URL http://jjap.jsap.jp/link?JJAP/50/030001/.

[11] P. F. McMillan, Nat Mater **3**, 755 (2004), ISSN 1476-1122, URL `http://dx.doi.org/10.1038/nmat1248`.

[12] A. Hedler, S. L. Klaumunzer, and W. Wesch, Nat Mater **3**, 804 (2004), ISSN 1476-1122, URL `http://dx.doi.org/10.1038/nmat1241`.

[13] R. Zallen, *The Physics of Amorphous Solids (Wiley Classics Library)* (Wiley-VCH, 1998), ISBN 0471299413, URL `http://www.worldcat.org/isbn/0471299413`.

[14] S. Roorda, K. Laaziri, and S. C. Gujrathi, Nuclear Instruments and Methods in Physics Research Section B: Beam Interactions with Materials and Atoms **148**, 360 (1999), ISSN 0168-583X, URL `http://www.sciencedirect.com/science/article/pii/S0168583X98006703`.

[15] S. K. Deb, M. Wilding, M. Somayazulu, and P. F. McMillan, Nature **414**, 528 (2001), ISSN 0028-0836, URL `http://dx.doi.org/10.1038/35107036`.

[16] A. P. GERK and D. TABOR, Nature **271**, 732 (1978), URL `http://dx.doi.org/10.1038/271732a0`.

[17] J. A. Yater and M. O. Thompson, Phys. Rev. Lett. **63**, 2088 (1989), URL `http://link.aps.org/doi/10.1103/PhysRevLett.63.2088`.

[18] G. Tamizhmani, M. Cocivera, R. T. Oakley, and P. Del Bel Belluz, Chemistry of Materials **2**, 473 (1990), `http://pubs.acs.org/doi/pdf/10.1021/cm00010a029`, URL `http://pubs.acs.org/doi/abs/10.1021/cm00010a029`.

[19] P. Kelly and R. Arnell, Vacuum **56**, 159 (2000), ISSN 0042-207X, URL `http://www.sciencedirect.com/science/article/pii/S0042207X9900189X`.

[20] B. Haberl, A. C. Y. Liu, J. E. Bradby, S. Ruffell, J. S. Williams, and P. Munroe, Phys. Rev. B **79**, 155209 (2009), URL `http://link.aps.org/doi/10.1103/PhysRevB.79.155209`.

[21] A. M. R. de Graff and M. F. Thorpe, Acta Crystallographica Section A **66**, 22 (2010), URL `http://dx.doi.org/10.1107/S0108767309045206`.

[22] Y. Jiao, F. H. Stillinger, and S. Torquato, Phys. Rev. E **81**, 011105 (2010), URL `http://link.aps.org/doi/10.1103/PhysRevE.81.011105`.

[23] W. A. Kamitakahara, H. R. Shanks, J. F. McClelland, U. Buchenau, F. Gompf, and L. Pintschovius, Phys. Rev. Lett. **52**, 644 (1984), URL `http://link.aps.org/doi/10.1103/PhysRevLett.52.644`.

[24] W. A. Kamitakahara, C. M. Soukoulis, H. R. Shanks, U. Buchenau, and G. S. Grest, Phys. Rev. B **36**, 6539 (1987), URL `http://link.aps.org/doi/10.1103/PhysRevB.36.6539`.

[25] B. Haberl, S. N. Bogle, T. Li, I. McKerracher, S. Ruffell, P. Munroe, J. S. Williams, J. R. Abelson, and J. E. Bradby, Journal of Applied Physics **110**, 096104 (pages 3) (2011), URL `http://link.aip.org/link/?JAP/110/096104/1`.

[26] P. A. Stolk, F. W. Saris, A. J. M. Berntsen, W. F. van der Weg, L. T. Sealy, R. C. Barklie, G. Krotz, and G. Muller, Journal of Applied Physics **75**, 7266 (1994), URL `http://link.aip.org/link/?JAP/75/7266/1`.

[27] U. Zammit, K. N. Madhusoodanan, M. Marinelli, F. Scudieri, R. Pizzoferrato, F. Mercuri, E. Wendler, and W. Wesch, Phys. Rev. B **49**, 14322 (1994), URL `http://link.aps.org/doi/10.1103/PhysRevB.49.14322`.

[28] S. Torquato and F. H. Stillinger, Phys. Rev. E **68**, 041113 (2003).

[29] M. Durandurdu, D. A. Drabold, and N. Mousseau, Phys. Rev. B **62**, 15307 (2000), URL `http://link.aps.org/doi/10.1103/PhysRevB.62.15307`.

[30] S. Roorda, C. Martin, M. Droui, M. Chicoine, A. Kazimirov, and S. Kycia, Phys. Rev. Lett. **108**, 255501 (2012), URL `http://link.aps.org/doi/10.1103/PhysRevLett.108.255501`.

[31] W. H. Zachariasen, J. Am. Chem. Soc. **54**, 3841 (1932), `http://pubs.acs.org/doi/pdf/10.1021/ja01349a006`, URL `http://pubs.acs.org/doi/abs/10.1021/ja01349a006`.

[32] D. S. Franzblau, Phys. Rev. B **44**, 4925 (1991), URL `http://link.aps.org/doi/10.1103/PhysRevB.44.4925`.

[33] S. V. Faleev, M. van Schilfgaarde, and T. Kotani, Phys. Rev. Lett. **93**, 126406 (2004), URL `http://link.aps.org/doi/10.1103/PhysRevLett.93.126406`.

[34] D. Weaire, Phys. Rev. Lett. **26**, 1541 (1971), URL `http://link.aps.org/doi/10.1103/PhysRevLett.26.1541`.

[35] D. Weaire and M. F. Thorpe, Phys. Rev. B **4**, 2508 (1971), URL `http://link.aps.org/doi/10.1103/PhysRevB.4.2508`.

[36] A. Donev, F. H. Stillinger, and S. Torquato, Phys. Rev. Lett. **95**, 090604 (2005).

[37] C. E. Zachary, Y. Jiao, and S. Torquato, Phys. Rev. E **83**, 051308 (2011), URL `http://link.aps.org/doi/10.1103/PhysRevE.83.051308`.

[38] C. E. Zachary, Y. Jiao, and S. Torquato, Phys. Rev. E **83**, 051309 (2011), URL `http://link.aps.org/doi/10.1103/PhysRevE.83.051309`.

[39] S. Torquato and F. H. Stillinger, Rev. Mod. Phys. **82**, 2633 (2010), URL `http://link.aps.org/doi/10.1103/RevModPhys.82.2633`.

[40] C. E. Zachary, Y. Jiao, and S. Torquato, Phys. Rev. Lett. **106**, 178001 (2011), URL `http://link.aps.org/doi/10.1103/PhysRevLett.106.178001`.

[41] Y. Jiao and S. Torquato, Phys Rev E Stat Nonlin Soft Matter Phys **84**, 041309 (2011).

[42] J. L. Lebowitz, Phys. Rev. A **27**, 1491 (1983), URL `http://link.aps.org/doi/10.1103/PhysRevA.27.1491`.

[43] L. Reatto and G. V. Chester, Phys. Rev. **155**, 88 (1967), URL `http://link.aps.org/doi/10.1103/PhysRev.155.88`.

[44] S. Torquato, A. Scardicchio, and C. E. Zachary, J. of Stat. Mech.: Theory and Exp. **2008**, P11019 (2008), URL `http://stacks.iop.org/1742-5468/2008/i=11/a=P11019`.

[45] A. Scardicchio, C. E. Zachary, and S. Torquato, Phys. Rev. E **79**, 041108 (2009), URL `http://link.aps.org/doi/10.1103/PhysRevE.79.041108`.

[46] R. D. Batten, F. H. Stillinger, and S. Torquato, Journal of Applied Physics **104**, 033504 (pages 12) (2008), URL `http://link.aip.org/link/?JAP/104/033504/1`.

[47] O. U. Uche, S. Torquato, and F. H. Stillinger, Phys. Rev. E **74**, 031104 (2006), URL `http://link.aps.org/doi/10.1103/PhysRevE.74.031104`.

[48] L. Pietronero, A. Gabrielli, and F. S. Labini, Physica A: Statistical Mechanics and its Applications **306**, 395 (2002), ISSN 0378-4371, invited Papers from the 21th IUPAP International Conference on Statistical Physics, URL `http://www.sciencedirect.com/science/article/pii/S0378437102005174`.

[49] C. Baugh, Encycl. of Astronomy and Astrophysics. IOP Publishing, Bristol (2006).

[50] R. Prum and R. Torres, in *Excursions in Harmonic Analysis, Volume 2*, edited by T. D. Andrews, R. Balan, J. J. Benedetto, W. Czaja, and K. A. Okoudjou (Birkhuser Boston, 2013), Applied and Numerical Harmonic Analysis, pp. 401–421, ISBN 978-0-8176-8378-8, URL `http://dx.doi.org/10.1007/978-0-8176-8379-5_20`.

[51] C. E. Zachary and S. Torquato, J. of Stat. Mech.: Theory and Exp. **2009**, P12015 (2009), URL `http://stacks.iop.org/1742-5468/2009/i=12/a=P12015`.

[52] R. D. Batten, F. H. Stillinger, and S. Torquato, Phys. Rev. Lett. **103**, 050602 (2009), URL `http://link.aps.org/doi/10.1103/PhysRevLett.103.050602`.

[53] R. D. Batten, F. H. Stillinger, and S. Torquato, The J. of Chem. Phy. **135**, 054104 (pages 16) (2011), URL `http://link.aip.org/link/?JCP/135/054104/1`.

[54] M. Florescu, S. Torquato, and P. J. Steinhardt, Phys. Rev. B **80**, 155112 (2009), URL `http://link.aps.org/doi/10.1103/PhysRevB.80.155112`.

[55] M. Florescu, S. Torquato, and P. J. Steinhardt, Proceedings of the National Academy of Sciences **106**, 20658 (2009), `http://www.pnas.org/content/106/49/20658.full.pdf+html`, URL `http://www.pnas.org/content/106/49/20658.abstract`.

[56] M. Florescu, S. Torquato, and P. J. Steinhardt, Applied Physics Letters **97**, 201103 (pages 3) (2010), URL `http://link.aip.org/link/?APL/97/201103/1`.

[57] W. Man, M. Florescu, K. Matsuyama, P. Yadak, S. Torquato, P. J. Steinhardt, and P. Chaikin, in *Conference on Lasers and Electro-Optics* (Optical Society of America, 2010), p. CThS2, URL `http://www.opticsinfobase.org/abstract.cfm?URI=CLEO-2010-CThS2`.

[58] N. Mousseau, G. T. Barkema, and S. M. Nakhmanson, Philosophical Magazine Part B **82**, 171 (2002), `http://www.tandfonline.com/doi/pdf/10.1080/13642810208208540`, URL `http://www.tandfonline.com/doi/abs/10.1080/13642810208208540`.

[59] D. Polk, Journal of Non-Crystalline Solids **5**, 365 (1971), ISSN 0022-3093, URL `http://www.sciencedirect.com/science/article/pii/002230937190038X`.

[60] D. E. Polk and D. S. Boudreaux, Phys. Rev. Lett. **31**, 92 (1973), URL `http://link.aps.org/doi/10.1103/PhysRevLett.31.92`.

[61] P. Steinhardt, R. Alben, M. G. Duffy, and D. E. Polk, Phys. Rev. B **8**, 6021 (1973), URL `http://link.aps.org/doi/10.1103/PhysRevB.8.6021`.

[62] P. Steinhardt, R. Alben, and D. Weaire, Journal of Non-Crystalline Solids **15**, 199 (1974), ISSN 0022-3093, URL `http://www.sciencedirect.com/science/article/pii/0022309374900490`.

[63] R. Alben, D. Weaire, and P. Steinhardt, Journal of Physics C: Solid State Physics **6**, L384 (1973), URL `http://stacks.iop.org/0022-3719/6/i=20/a=003`.

[64] P. N. Keating, Phys. Rev. **145**, 637 (1966), URL `http://link.aps.org/doi/10.1103/PhysRev.145.637`.

[65] P. N. Keating, Phys. Rev. **149**, 674 (1966), URL `http://link.aps.org/doi/10.1103/PhysRev.149.674`.

[66] P. N. Keating, Phys. Rev. **152**, 774 (1966), URL `http://link.aps.org/doi/10.1103/PhysRev.152.774`.

[67] P. N. Keating, Phys. Rev. **169**, 758 (1968), URL `http://link.aps.org/doi/10.1103/PhysRev.169.758`.

[68] F. Wooten, K. Winer, and D. Weaire, Phys. Rev. Lett. **54**, 1392 (1985), URL `http://link.aps.org/doi/10.1103/PhysRevLett.54.1392`.

[69] B. R. Djordjević, M. F. Thorpe, and F. Wooten, Phys. Rev. B **52**, 5685 (1995), URL `http://link.aps.org/doi/10.1103/PhysRevB.52.5685`.

[70] G. T. Barkema and N. Mousseau, Phys. Rev. B **62**, 4985 (2000), URL `http://link.aps.org/doi/10.1103/PhysRevB.62.4985`.

[71] R. L. C. Vink, G. T. Barkema, M. A. Stijnman, and R. H. Bisseling, Phys. Rev. B **64**, 245214 (2001), URL `http://link.aps.org/doi/10.1103/PhysRevB.64.245214`.

[72] N. Mousseau and G. T. Barkema, Phys. Rev. E **57**, 2419 (1998), URL `http://link.aps.org/doi/10.1103/PhysRevE.57.2419`.

[73] D. A. Drabold, The European Physical Journal B **68**, 1 (2009), ISSN 1434-6028, URL `http://dx.doi.org/10.1140/epjb/e2009-00080-0`.

[74] M. C. Rechtsman, F. H. Stillinger, and S. Torquato, Phys. Rev. E **75**, 031403 (2007), URL `http://link.aps.org/doi/10.1103/PhysRevE.75.031403`.

[75] F. H. Stillinger and T. A. Weber, Phys. Rev. B **31**, 5262 (1985), URL `http://link.aps.org/doi/10.1103/PhysRevB.31.5262`.

[76] R. Vink, G. Barkema, W. van der Weg, and N. Mousseau, Journal of Non-Crystalline Solids **282**, 248 (2001), ISSN 0022-3093, URL `http://www.sciencedirect.com/science/article/pii/S0022309301003428`.

[77] J. Tersoff, Phys. Rev. Lett. **56**, 632 (1986), URL `http://link.aps.org/doi/10.1103/PhysRevLett.56.632`.

[78] J. Tersoff, Phys. Rev. B **37**, 6991 (1988), URL `http://link.aps.org/doi/10.1103/PhysRevB.37.6991`.

[79] J. Tersoff, Phys. Rev. B **38**, 9902 (1988), URL `http://link.aps.org/doi/10.1103/PhysRevB.38.9902`.

[80] M. Z. Bazant and E. Kaxiras, Phys. Rev. Lett. **77**, 4370 (1996), URL `http://link.aps.org/doi/10.1103/PhysRevLett.77.4370`.

[81] M. Z. Bazant, E. Kaxiras, and J. F. Justo, Phys. Rev. B **56**, 8542 (1997), URL `http://link.aps.org/doi/10.1103/PhysRevB.56.8542`.

[82] J. F. Justo, M. Z. Bazant, E. Kaxiras, V. V. Bulatov, and S. Yip, MRS Proceedings **469** (1997), ISSN null, URL `http://journals.cambridge.org/article_S1946427400287253`.

[83] J. a. F. Justo, M. Z. Bazant, E. Kaxiras, V. V. Bulatov, and S. Yip, Phys. Rev. B **58**, 2539 (1998), URL `http://link.aps.org/doi/10.1103/PhysRevB.58.2539`.

[84] L. Verlet, Phys. Rev. **159**, 98 (1967), URL `http://link.aps.org/doi/10.1103/PhysRev.159.98`.

[85] L. VERLET, Phys. Rev. **165**, 201 (1968), URL `http://link.aps.org/doi/10.1103/PhysRev.165.201`.

[86] M. D. Kluge, J. R. Ray, and A. Rahman, Phys. Rev. B **36**, 4234 (1987), URL `http://link.aps.org/doi/10.1103/PhysRevB.36.4234`.

[87] D. Drabold and J. Li, Current Opinion in Solid State and Materials Science **5**, 509 (2001), ISSN 1359-0286, URL `http://www.sciencedirect.com/science/article/pii/S1359028602000049`.

[88] W. D. Luedtke and U. Landman, Phys. Rev. B **37**, 4656 (1988), URL `http://link.aps.org/doi/10.1103/PhysRevB.37.4656`.

[89] M. H. Brodsky and R. S. Title, Phys. Rev. Lett. **23**, 581 (1969), URL `http://link.aps.org/doi/10.1103/PhysRevLett.23.581`.

[90] J. R. Dennis and E. B. Hale, Journal of Applied Physics **49**, 1119 (1978), URL `http://scitation.aip.org/getabs/servlet/GetabsServlet?prog=normal\&id=JAPIAU000049000003001119000001\&idtype=cvips\&gifs=yes`.

[91] N. Metropolis, A. W. Rosenbluth, M. N. Rosenbluth, A. H. Teller, and E. Teller, The Journal of Chemical Physics **21**, 1087 (1953), URL `http://link.aip.org/link/?JCP/21/1087/1`.

[92] B. Hajek, Mathematics of Operations Research **13**, 311 (1988), `http://mor.journal.informs.org/content/13/2/311.full.pdf+html`, URL `http://mor.journal.informs.org/content/13/2/311.abstract`.

[93] S. Kirkpatrick, C. D. Gelatt, and M. P. Vecchi, Science **220**, pp. 671 (1983), ISSN 00368075, URL `http://www.jstor.org/stable/1690046`.

[94] V. Cerny, Journal of Optimization Theory and Applications **45**, 41 (1985), ISSN 0022-3239, URL `http://dx.doi.org/10.1007/BF00940812`.

[95] J. C. Slater and G. F. Koster, Phys. Rev. **94**, 1498 (1954), URL `http://link.aps.org/doi/10.1103/PhysRev.94.1498`.

[96] I. Kwon, R. Biswas, C. Z. Wang, K. M. Ho, and C. M. Soukoulis, Phys. Rev. B **49**, 7242 (1994), URL `http://link.aps.org/doi/10.1103/PhysRevB.49.7242`.

[97] L. Goodwin, A. J. Skinner, and D. G. Pettifor, EPL (Europhysics Letters) **9**, 701 (1989), URL `http://stacks.iop.org/0295-5075/9/i=7/a=015`.

[98] N. Bernstein, M. J. Mehl, and D. A. Papaconstantopoulos, Phys. Rev. B **66**, 075212 (2002), URL `http://link.aps.org/doi/10.1103/PhysRevB.66.075212`.

[99] W. A. Harrison (1980).

[100] R. L. McGreevy, Journal of Physics: Condensed Matter **13**, R877 (2001), URL `http://stacks.iop.org/0953-8984/13/i=46/a=201`.

[101] R. L. McGreevy and L. Pusztai, Molecular Simulation **1**, 359 (1988), `http://www.tandfonline.com/doi/pdf/10.1080/08927028808080958`, URL `http://www.tandfonline.com/doi/abs/10.1080/08927028808080958`.

[102] F. H. Stillinger, Phys. Rev. E **59**, 48 (1999), URL `http://link.aps.org/doi/10.1103/PhysRevE.59.48`.

[103] P. Hohenberg and W. Kohn, Phys. Rev. **136**, B864 (1964), URL `http://link.aps.org/doi/10.1103/PhysRev.136.B864`.

[104] W. Kohn, Rev. Mod. Phys. **71**, 1253 (1999), URL `http://link.aps.org/doi/10.1103/RevModPhys.71.1253`.

[105] W. Kohn and L. J. Sham, Phys. Rev. **140**, A1133 (1965), URL `http://link.aps.org/doi/10.1103/PhysRev.140.A1133`.

[106] P. Beaucage and N. Mousseau, Phys. Rev. B **71**, 094102 (2005), URL `http://link.aps.org/doi/10.1103/PhysRevB.71.094102`.

[107] A. B. Hopkins, F. H. Stillinger, and S. Torquato, Phys. Rev. E **86**, 021505 (2012), URL `http://link.aps.org/doi/10.1103/PhysRevE.86.021505`.

[108] E. Marcotte, F. H. Stillinger, and S. Torquato, The Journal of Chemical Physics **138**, 12A508 (pages 10) (2013), URL `http://link.aip.org/link/?JCP/138/12A508/1`.

[109] M. M. J. Treacy and K. B. Borisenko, Science **335**, 950 (2012), `http://www.sciencemag.org/content/335/6071/950.full.pdf`, URL `http://www.sciencemag.org/content/335/6071/950.abstract`.

[110] M. Fried, T. Lohner, W. A. M. Aarnink, L. J. Hanekamp, and A. van Silfhout, Journal of Applied Physics **71**, 5260 (1992), URL `http://link.aip.org/link/?JAP/71/5260/1`.

[111] J. M. Gibson, M. M. J. Treacy, T. Sun, and N. J. Zaluzec, Phys. Rev. Lett. **105**, 125504 (2010), URL `http://link.aps.org/doi/10.1103/PhysRevLett.105.125504`.

[112] J.-Y. Cheng, J. M. Gibson, and D. C. Jacobson, Journal of Materials Research **16**, 3030 (2001), ISSN 2044-5326, URL `http://journals.cambridge.org/article_S0884291400064979`.

[113] S. M. Nakhmanson, P. M. Voyles, N. Mousseau, G. T. Barkema, and D. A. Drabold, Phys. Rev. B **63**, 235207 (2001), URL `http://link.aps.org/doi/10.1103/PhysRevB.63.235207`.

[114] D. L. Price, S. C. Moss, R. Reijers, M. L. Saboungi, and S. Susman, Journal of Physics: Condensed Matter **1**, 1005 (1989), URL `http://stacks.iop.org/0953-8984/1/i=5/a=017`.

[115] J. M. Gibson, Science **335**, 929 (2012), `http://www.sciencemag.org/content/335/6071/929.full.pdf`, URL `http://www.sciencemag.org/content/335/6071/929.short`.

[116] P. M. Voyles and J. R. Abelson, Solar Energy Materials and Solar Cells **78**, 85 (2003), ISSN 0927-0248, critical review of amorphous and microcrystalline silicon materials and solar cells, URL `http://www.sciencedirect.com/science/article/pii/S0927024802004348`.

[117] J. Phillips, Journal of Non-Crystalline Solids **34**, 153 (1979), cited By (since 1996) 738, URL `http://www.scopus.com/inward/record.url?eid=2-s2.0-0018530220&partnerID=40&md5=abb4a23b02cf2a5a172f68f8011c2507`.

[118] M. F. Thorpe, Journal of Non-Crystalline Solids **57**, 355 (1983).